universität wien

MASTERARBEIT | MASTER'S THESIS

Titel | Title

Computational characterisation of Ra^+ and Sr^+ for the development of optical atomic clocks

verfasst von | submitted by

Robin Cserveny BSc.

angestrebter akademischer Grad | in partial fulfilment of the requirements for the degree of

Master of Science (MSc)

Wien | Vienna, 2025

Studienkennzahl lt. Studienblatt | Degree programme code as it appears on the student record sheet:	UA 066 876
Studienrichtung lt. Studienblatt | Degree programme as it appears on the student record sheet:	Masterstudium Physics
Betreut von | Supervisor:	Univ.-Prof. Dr.techn. Cesare Franchini

CONTENTS

ABSTRACT (GERMAN)

Motiviert durch den Plan, optische Atomuhren basierend auf Ra^+ und Sr^+ in Richtung ihrer prognostizierten Präzisionen weiterzuentwickeln, präsentiere ich eine umfassende Charakterisierung dieser alkali-ähnlichen Ionen. Zu den berechneten Schlüsselgrößen gehören Lebensdauern, Übergangsmatrixelemente sowie Polarisierbarkeiten. Diese Arten von Atomuhren bieten außergewöhnliches Potential für Studien der theoretischen Physik, wie etwa Variationen der Feinstrukturkonstante, Verletzungen der atomaren Parität oder die Suche nach Dunkler Materie. Alle Berechnungen für diese Arbeit wurden mithilfe des Codes AMPSCI durchgeführt. Ich präsentiere Werte für reduzierte elektrische Dipol-, elektrische Quadrupol-, und magnetische Dipol-Matrixelemente, atomare Spektren, Lebensdauern angeregter Zustände, sowie statische und dynamische Polarisierbarkeiten. Darüber hinaus werden magische Wellenlängen, Hyperfein A-Konstanten und Sensitivitätskoeffizienten für eine mögliche zeitliche Variation der Feinstrukturkonstante bereitgestellt. Diese Größen wurden mithilfe der Korrelationspotentialmethode auf All-Orders-Niveau berechnet, wobei Korrekturen durch quantenelektrodynamische Effekte, die Breit-Wechselwirkung sowie durch Strukturstrahlung und Normierung berücksichtigt werden. Für diese Berechnungen wurden hauptsächlich niedrig liegende s- und p-Valenzzustände bis $n = 8$ und d-Zustände bis $n = 6$ für Ra^+ betrachtet, während die entsprechenden n-Werte für Sr^+ auf $n = 6$ und $n = 4$ begrenzt wurden. Zusätzlich werden Daten für Ba^+ bereitgestellt, das aufgrund seiner ähnlichen atomaren Struktur als Vergleich sowie als 'proof of concept' diente. Ziel dieser Arbeit ist es, die Weiterentwicklung der Ra^+ und Sr^+ optischen Atomuhren hin zu ihrer prognostizierten Präzision von etwa 10^{-18} zu unterstützen. Die präsentierten Ergebnisse bilden eine solide Grundlage für weitere experimentelle und theoretische Fortschritte auf diesem Gebiet.

ABSTRACT (ENGLISH)

Motivated by the plan to develop Ra^+ and Sr^+ optical atomic clocks toward their projected precisions, I present a comprehensive computational characterisation of these alkali-like ions. Calculated key quantities include lifetimes, transition matrix elements as well as polarisabilities. Those types of atomic clocks possess exceptional potential for studies of fundamental physics such as investigations into variations in the fine-structure constant, violations of atomic parity, and searches for dark matter. All calculations for this study were performed using the dedicated code library AMPSCI. I provide values for reduced electric dipole, electric quadrupole, and magnetic dipole matrix elements, atomic spectra, lifetimes of excited states, and both static and dynamic polarisabilities. Additionally, magic wavelengths, hyperfine A and field shift constants, and sensitivity coefficients to a possible time variation in the fine-structure constant are reported. These quantities were computed using the all-orders correlation potential method, supplemented with corrections for quantumelectrodynamical effects, Breit interaction, as well as structure radiation and normalisation. I primarily consider low-lying s and p valence states up to $n = 8$, and d states up to $n = 6$ for Ra^+, with corresponding states for Sr^+ truncated to $n = 6$ and $n = 4$, respectively. For comparison and proof of concept, additional calculations are presented for Ba^+, whose similar atomic structure helped to benchmark the methodology. This thesis aims to support the ongoing development of Ra^+ and Sr^+ optical atomic clocks towards their projected fractional frequency uncertainties on the order of 10^{-18}. The presented results offer a solid foundation for further experimental and theoretical advances in this field.

ACKNOWLEDGMENTS

First and foremost, I would like to thank both of my supervisors, Prof. Cesare Franchini (UniVie[1]) and Benjamin M. Roberts, PhD (UQ[2]), for providing me with the opportunity to work on such an interesting and up-to-date project.

I want to explicitly thank Ben for his kindness and helpfulness when I was inquiring for possible master's thesis topics while I was studying abroad at UQ and was taking part in the Computational Physics course he was lecturing. Since I really enjoyed this course, I wanted to delve more deeply into the research of Atomic Structure calculations. Fortunately for me, he soon offered me this topic, which I was very keen to take on. Ben was always trying to make time for my (many) questions that came up during this study and was very patient to answer all of them during our weekly meetings, which he was even willing to continue when I was not in Australia anymore, and when the time zone difference made it increasingly difficult to organise. Furthermore, I would also like to thank him for offering and providing the funds to present parts of my work at the ANZCOP-AIP Summer Meeting 2023 at the Australian National University in Canberra. Lastly, I am grateful for his help and guidance in writing the two papers that emerged from this thesis. It has been a privilege to get such great first-hand support while publishing as a first author for the first time, and he has provided me with great insights into the practices of being a researcher, which I hope to soon make use of as a PhD student.
Additionally, I want to express my gratitude towards Cesare, who was so kind and willing to take on the role as my supervisor in Vienna when I contacted him via email. Not everyone would have offered that, and I highly appreciate it.
Furthermore, I want to thank the Directorate of Studies and therefrom explicitly Prof. Paul Winkler, who have helped me to (spontaneously) organise doing my thesis abroad. Without their permission, it would not have been possible to make use of this great opportunity for which I am still very grateful.

In addition, I want to thank the *UQ Research Computing Centre* for allowing me to use their high-performance computer *Bunya*, which was used for some calculations that were carried out during this project.

Last but not least, I express a special gratitude to my family, friends, and fellow colleagues, for their always present support. Of those some were also offering to read through various sections, which has helped me to improve the readability of this text.

[1] University of Vienna, Vienna, Austria
[2] The University of Queensland, Brisbane, Queensland, Australia

PUBLICATIONS

Work from this thesis will be published in:

1) R. Cserveny, B. M. Roberts. Computational characterisation of Ra^+ and Ba^+ (in preparation)
Personal contribution: Data aquisition, drafting of the paper, design of tables and plots

2) R. Cserveny, B. M. Roberts. Computational characterisation of Sr^+ and Ca^+ (in preparation)
Personal contribution: Data aquisition, drafting of the paper

I have presented some results from this thesis at the:

- ANZCOP-AIP[3] Summer Meeting 2023, The Australian National University, Canberra, Australia, 2023. Talk:
Theoretical characterisation of the Ra ion for the development of atomic clocks and studies of fundamental physics

[3] Australian and New Zealand Conference on Optics and Photonics and the Australian Institute for Physics

LIST OF ABREVIATIONS

AMPSCI: Atomic Many-Body Perturbation Theory in the Screened Coulomb Interaction

a.u.: atomic units

BW: Bohr-Weisskopf

CC(SDv/pT): Coupled-Cluster (Single Double valence/partial Triple)

CPSCI: Correlation Potential (Method) in the Screened Coulomb Interaction

E1/2: Electric Dipole/Quadrupole

Exp.: Experimental

M1: Magnetic Dipole

ME: Matrix Element

MBPT: Many-Body Perturbation Theory

NIST: National Institute of Science and Technology

NR: non-relativistically

OAC: Optical Atomic Clock

PTSCI: Perturbation Theory in the Screened Coulomb Interaction

RHF: Relativistic Hartfree-Fock

RPA: Random Phase Approximation

SD: Standard Deviation

SR+N: Structure Radiation and Normalisation

TDHF: Time-Dependent Hartree-Fock

α_0**:** fine-structure constant (current value)

a_B**:** Bohr radius

Σ**:** Correlation Potential

$\Sigma^{(2)}$**:** 2^{nd}-order Correlation Potential

$\Sigma^{(\infty)}$**:** All-Orders Correlation Potential

$\lambda\Sigma$**:** Scaled Correlation Potential

λ_m**:** Magic wavelength

I. INTRODUCTION

Optical atomic clocks are the most precise instruments to date. In fact, their frequency can be measured as exactly as about 1 part in 10^{18} [12, 16, 85]. They are most known for their canonical applications in navigation and positioning, as well as time measurements. Due to their unparalleled stability and accuracy, they are also exceptional tools for studies of fundamental physics [40, 107]. This includes measurements to constrain variations of fundamental constants, such as the fine-structure constant ([31, 33, 41, 57]), or the ratio of the electron-to-proton mass [35, 46, 49, 52, 57]. Furthermore, they can be used for searches for dark matter and dark energy ([33]), as probes for exotic physics such as atomic parity violation ([40, 107]) or possible violation of the equivalence principle [31, 41]. Additionally, they allow testing of quantum theory with extraordinary precision [107].

The precision of an atomic clock is usually described by the so-called *fractional frequency uncertainty*. It is defined as the ratio of uncertainty in the measurement of the clock frequency ($\delta\nu$) to the frequency ν_0 itself: $\frac{\delta\nu}{\nu_0}$ [44]. From now on the words *precision* and *fractional frequency uncertainty* will be used interchangeably.

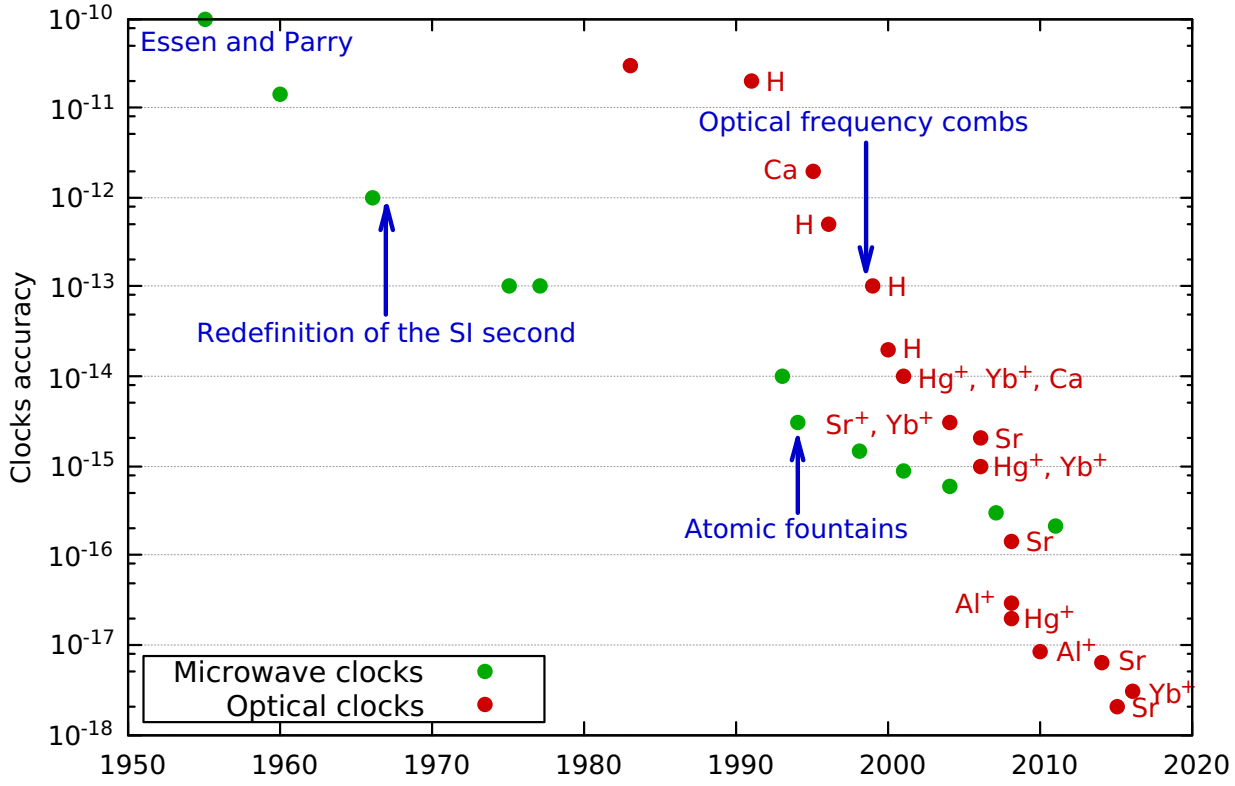

FIG. 1: This figure shows the development of the fractional frequency uncertainty (denoted here as 'Clocks accuracy') of different types of atomic clocks over time. It can be inferred that optical clocks have a more promising trend in comparison to older microwave concepts. Taken from [13].

Figure 1 shows the development of the fractional frequency uncertainty of different types of atomic clocks over time. It can be seen that since the invention of the first Cesium atomic clock in 1955 by Louis Essen, the precisions have continuously improved. Cs atomic clocks, typically operating on the atom's infamous 9.19 GHz hyperfine transition have long been considered the gold standard of

time measurements. Due to their immense success, they were used to redefine the unit of second in the SI system in 1967. The second has since been defined as 9.192.631.770 cycles of a laser tuned to a hyperfine transition between two ground states of Cesium-133 [96]. This transition is considered a microwave transition since its frequency corresponds to the microwave regime. Microwave atomic clocks, most of which are using Cs, were able to reach fractional frequency uncertainties of about 10^{-16}. This is expected to be close to their practical limitations ([44]), due to certain constraining factors, which will be explained briefly in Sec. II A.

The performance of an atomic clock depends on the atomic structure of the atom or ion used, the sensitivity to its environment, and – particularly relevant for mobile atomic clocks – on the necessary experimental setup [47]. In general, the uncertainty of a clock is inversely proportional to its frequency [117]. This can be best explained with the so-called atomic line quality factor Q, which is defined as the ratio of the transition frequency ν_0 to its natural linewidth $\Delta\nu$ [44]:

$$Q = \frac{\nu_0}{\Delta\nu}. \tag{1}$$

Sometimes it is simply referred to as *line* Q. It serves as a rating of the intrinsic frequency purity of a system. A higher value of Q is preferable, since it means that the peak around ν_0 is sharper. Therefore, it can be measured more precisely in theory. For example, Cs clocks have a line Q of about 10^{10}. Whereas optical atomic clocks (OACs) using optical transitions have demonstrated Q-values as high as 10^{15}, hence 5 orders of magnitude larger than analogous microwave systems, providing a tremendous inherent advantage for achieving high precisions [44, 47]. The first optical atomic clocks were developed in the 1980s. It took some time for these concepts to surpass the precisions of microwave clocks, which was finally achieved in 2008. This was done by a group at NIST[4], demonstrating uncertainties in the 10^{-17} range for two clocks using Al^+ and Hg^+ ions [52].

The major challenge with constructing optical frequency standards was the measurement of those optical frequencies itself. Due to their fast oscillations of around 10^{15} Hz they could not be measured directly. Their indirect measurement only became feasible because of advances in connecting these frequencies to the microwave domain by sophisticated efforts. The development of so-called *optical frequency combs* earned Theodor W. Hänsch and John L. Hall a Nobel Prize in 2005 (see Ref. [1]). Nowadays, most commonly the elements Sr, Hg^+, and Yb^+ are used to construct optical atomic clocks, with fractional frequency uncertainties down to about 10^{-18} [43, 50, 51, 58]. This means that those clocks deviate less than a second over the age of the universe – an immense achievement [17]. Furthermore, they are so precise that gravitational potential differences originating from the theory of General Relativity can be accurately measured down to the cm-level [42, 44].

[4] National Institute of Standard and Technology

Towards a Ra^+ and Sr^+ Optical Clock

Certain research groups proposed a Ra^+ and Sr^+ optical atomic clock since improvements in performance are predicted in comparison to existing clocks [71, 81]. It is expected that fractional frequency uncertainties of 10^{-18} can be achieved, which would rank them among the most accurate clocks [40, 47, 91, 117]. Furthermore, especially certain transitions in Ra^+ are very sensitive to variations in the fine structure constant α ([40, 47]) or to dark matter interactions ([4, 66]). In fact, it is known that Ra^+ has the largest positive enhancement of time variations in α of any clock that has ever been investigated [57, 71]. Together with Hg^+, which features a high sensitivity of opposite sign ([46, 73]), it could be used to further improve constraints on the variation of this constant [40].

At the moment a group at the *University of California, Santa Barbara (UCSB)* is building a $^{226}Ra^+$ clock. So far, Holliman et al. were able to demonstrate a fractional frequency uncertainty of $9 \cdot 10^{-16}$ (see [71]). Strontium ion atomic clocks have already been built approximately 20 years ago. Their evaluated uncertainty has since fallen by several orders of magnitude ([19, 20, 87]), with the most accurate Sr^+ clock to date having an uncertainty of $1.2 \cdot 10^{-17}$ [21]. An estimate for an achievable uncertainty of approximately $3 \cdot 10^{-18}$ was given by Dubé et al. in 2016 [21]. This suggests that further improvements in precision can be expected for both Ra^+ and Sr^+ OACs.

Throughout this thesis, the ions were characterised by calculating various quantities which are important for their implementation as atomic clocks. These include, but are not limited to atomic spectra, transition matrix elements, lifetimes of excited states, atomic polarisabilities, and magic wavelengths. Additionally, sensitivity coefficients to variations in α, hyperfine A constants, and field shift constants were computed. These calculations were performed using the dedicated code library AMPSCI (Atomic Many-Body Perturbation Theory in the Screened Coulomb Interaction), specifically designed for high-precision atomic structure calculations of single-valence systems [106]. Currently, the literature contains limited data for Ra^+ and Sr^+, with experimental data being particularly scarce. Consequently, the results of this work were primarily compared with theoretical calculations from other research groups. We hope that future experimental data will be able to support the predictions made within the experimental standard deviations. To ensure the reliability of the AMPSCI library, especially for the case of Ra^+ where experimental data is sparse, we first compared its results for similar atoms and ions with the currently available experimental and theoretical data from other groups.
Ba^+ was chosen as the primary reference for Ra^+, along with Sr^+ due to the availability of more extensive experimental data for these ions. They share similar properties, as they are located close to each other in the periodic table (see Fig. 2). Each of them has a single valence electron above a noble gas-like closed shell as well as relatively high mass. Additionally, they all exist as singly-charged ions. Moreover, far more experimental data is available for these ions than for Ra^+. In the case of Radium, its radioactivity further complicates experiments by increasing associated costs and making it more difficult to obtain and handle.

In the following chapters, I demonstrate that the calculations show excellent agreement with the available experimental data for all ions, often within their standard deviations. This served as a proof of concept and gave us confidence in applying the same computational methods to Ra^+. Especially for the case of Sr^+, a high precision is very probable since Ba^+ features one more shell and therefore a higher computational complexity, while still showing excellent agreement with experiments. The consistency between our theoretical predictions and the experimental data for these systems supports the robustness of our methods for studying these three ions.

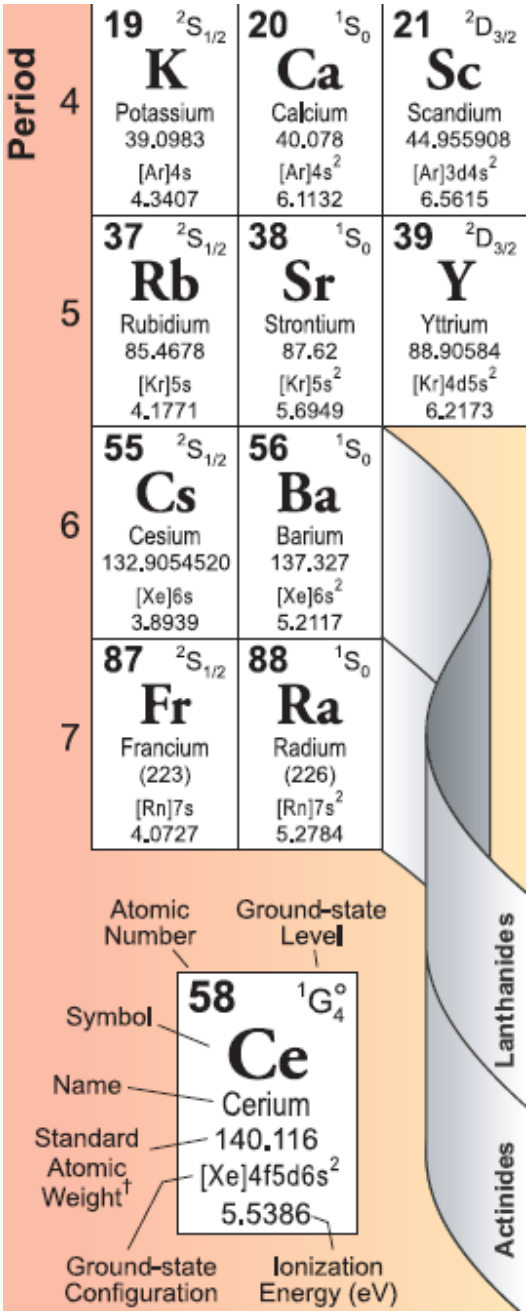

FIG. 2: Elements closest to Ra and Sr in the periodic table. Taken from [95].

The next chapter, 'Theoretical Background' (II), will provide a summary of the necessary theory behind the quantities we calculated, along with references to further resources. Chapter III, 'Computational Methods', will discuss the computational methods that were used as well as give an overview on perturbational approaches. We will then present and discuss the results while comparing them to the existing literature in Chapter IV. Finally, Chapter V will give a Conclusion to summarise the obtained knowledge, along with an Outlook for possible further research.

II. THEORETICAL BACKGROUND

This chapter will serve as an overview of the theory behind the calculated quantities as well as atomic clocks. All units will be given in atomic units if not stated otherwise. These are defined by setting $\hbar = e = m_e = c\alpha = 1$. For details outside the scope of this thesis, the appropriate references will be provided.

A. Optical Atomic Clocks

This section will provide a more physical description of atomic clocks and will focus on optical atomic clocks using single ions. Most of the principles are also applicable to clocks using different types of transitions. It will follow Refs. [44] and [85] closely.

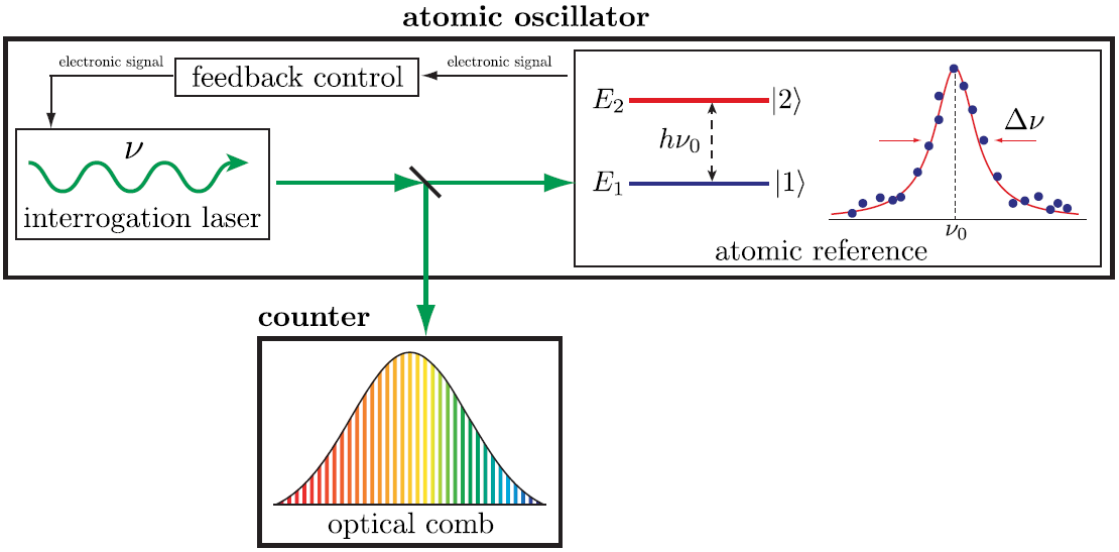

FIG. 3: Illustration of an optical atomic clock. The laser is resonant with the atomic transition. If it deviates slightly, a correction signal can be fed back via a feedback loop. An optical comb is used to divide the optical frequency down to countable microwave signals. Taken from [44].

Figure 3 shows the basic building blocks of an atomic clock. The most essential part of an atomic clock is its transition. For OACs, the frequency of the utilised transition is in the optical spectrum. A transition operates between two energy levels, which are denoted here as state $|1\rangle$ with energy E_1 and state $|2\rangle$ with its respective energy. The corresponding transition frequency ν_0 can be given via the following relation: $\nu_0 = \frac{E_2 - E_1}{h}$[5]. ν_0 is specific for each transition and ion species, which makes it a well-suited tool for time comparisons. In practice, environmental perturbations influence the transition frequency. These are, for example, black-body radiation, Stark shifts, Zeeman shifts, and Doppler shifts [71, 122]. All of these factors contribute significantly to the uncertainty of the frequency measurement and have to be taken into account. For the sake of ease of explanation, we will ignore these perturbations for now. We can simply think of ν_0 as the unperturbed frequency. In order to make use of an atomic transition, there has to be a means of preparing the desired initial state. In this case, it would be necessary to ensure that state $|1\rangle$ is occupied before a laser with frequency ν_0 is used to drive the $|1\rangle \rightarrow |2\rangle$ transition. Additionally, it must be possible to

[5] or $\nu_0 = \frac{E_2 - E_1}{2\pi}$ in atomic units

determine whether the electron is in the correct state ($|2\rangle$) after being driven by the laser. This is measured indirectly via atomic spectroscopy and determines how closely the laser frequency ν is to the frequency of the transition (ν_0) itself [44]. Furthermore, there has to be some sort of feedback loop in order to adjust ν closer to ν_0 if necessary. The frequency is measured with the help of an optical frequency comb, which is used to divide the optical frequency down to countable microwave or radio signals [44].

In practice, the operation of an atomic clock is achieved by utilising more than 2 energy levels and by choosing transitions with useful properties. We will best explain this in a practical example, such as the first single ion Ra^+ clock developed. This was achieved by Holliman et al., with the corresponding paper (see Ref. [71]) being published in 2022. It was able to reach a fractional frequency uncertainty of $9 \cdot 10^{-16}$.

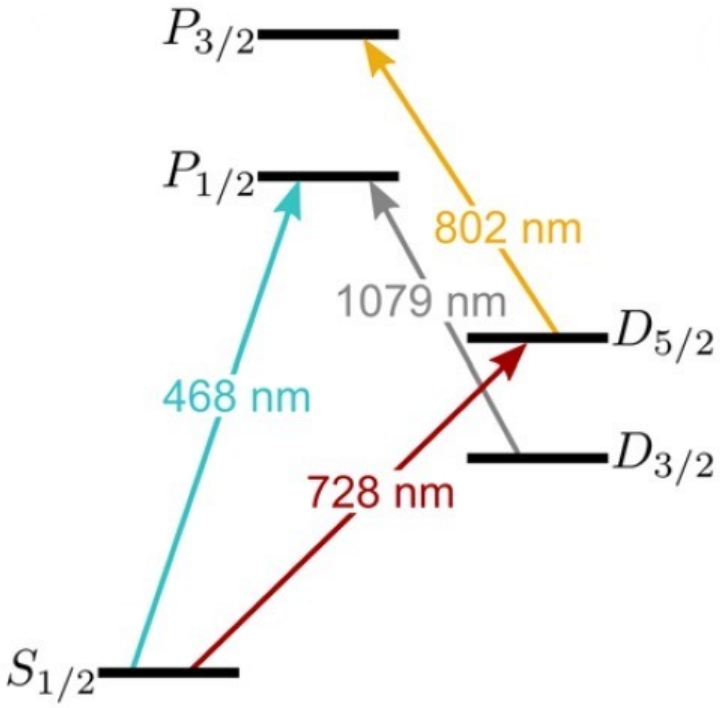

FIG. 4: Illustration of the atomic levels used for the first operation of a $^{226}Ra^+$ ion optical atomic clock. It was developed by a group at the *University of California, Santa Barbara (UCSB)* by Holliman et al. The $7S_{1/2} \longrightarrow 6D_{5/2}$ transition with a wavelength of 728 nm was used. Taken from [71].

This clock used the $7s_{1/2} \longrightarrow 6d_{5/2}$ transition in $^{226}Ra^+$ with a wavelength of 728 nm and was confined using an ion trap [71]. For an illustration of the utilised energy levels and transitions, please refer to Fig. 4. It should be mentioned that most Sr^+ clocks utilize the corresponding $s_{1/2} \longrightarrow d_{5/2}$ transition as well, which further speaks to the similarity of those two ionic systems. An important feature of this transition is that it is strongly forbidden (see Sec. II B) and therefore the $6d_{5/2}$ (upper) state has a long lifetime, with a lower bound of 0.232(4) s set by experiment [45]. It can decay to either the $7s_{1/2}$ or $6d_{3/2}$ state via electric quadrupole and magnetic dipole transitions[6] (see also Sec. II B). In order to prepare the ion in the desired initial state ($7s_{1/2}$) again

[6] These categories of transitions arise through a multipole expansion of the electromagnetic field.

after driving the transition, its valence electron is simultaneously pumped to the two higher-lying P states. From those, it will quickly decay back to the $7s$ state via allowed (electric dipole) transitions and therefore relatively high transition probability. The valence electron cannot decay into a lower energy state since all inner shells are already occupied in this configuration. This allows us to start the measurement cycle again. By repeating this procedure often enough, the clock frequency can be measured ever more precisely by using statistical methods. Other clock concepts will use different transitions, but the principle stays the same.
To sum up, the utilised transition will be forbidden, with accessible higher-lying levels having allowed transitions to decay into the desired initial state and hence allowing for a quick initialisation. Additionally, the initial state should have a relatively long lifetime, which is naturally ensured if only forbidden transitions to lower-energy states are possible. These facts highlight the importance of good knowledge of the atomic structure of the ion used in an atomic clock [47, 122]. Furthermore, it is important to study the effects of perturbations such as from electromagnetic fields (see Sec. II D) since these occur, e.g., when using ion traps or occur naturally through black-body radiation, which can influence the transition frequency. For further details about the experimental setup, such as the realisation of the feedback control loop for the laser or optical atomic clocks in general, please inspect Refs. [17, 44, 71, 85].

B. Matrix Elements

This section will give an overview of the types of matrix elements that were calculated for this study. It is closely oriented at Refs. [78, 122]. As mentioned in the previous section, decent knowledge of the atomic structure of the utilised system is necessary. With this knowledge, suitable transitions can be identified more easily. Lets start with the expansion of the electromagnetic field as a sum of plane waves, $e^{\pm i\vec{k}\cdot\vec{r}}$ [78]:

$$\vec{\boldsymbol{E}} \propto ik\,(a\,e^{i\vec{k}\vec{r}} - a^*\,e^{-i\vec{k}\vec{r}}). \tag{2}$$

The transition probability from state $|a\rangle$ to lower lying state $|b\rangle$ is proportional to the matrix element [78]:

$$dW_{ab} \propto |\,\boldsymbol{e_k}\,\langle a|\,\hat{\boldsymbol{p}}\,e^{-i\vec{k}\cdot\vec{r}}\,|b\rangle\,|^2\,d\Omega. \tag{3}$$

Here, dW_{ab} is the transition probability of a photon polarised along $\boldsymbol{e_k}$ in the solid angle $d\Omega$. $\hat{\boldsymbol{p}}$ denotes the quantum-mechanical impulse operator. If the wavelength of the field is much larger than the length of the system, it can be approximated to first order as a dipole field. This implies that the product in the exponential expansion of $\vec{k}\cdot\vec{r} << 1$. Therefore, it follows that $e^{-i\vec{k}\cdot\vec{r}} \approx 1$. The element $\langle a|\,\hat{\boldsymbol{p}}e^{-i\vec{k}\cdot\vec{r}}\,|b\rangle \approx \langle a|\,\hat{\boldsymbol{p}}\,|b\rangle$ can accordingly be written as $m\,\langle a|\,\hat{\boldsymbol{v}}\,|b\rangle = i\,\omega\,m\,\langle a|\,\hat{\boldsymbol{r}}\,|b\rangle$ [78]. This is commonly known as the dipole approximation. With the definition of the electric dipole moment operator, $\hat{\boldsymbol{D}} := e\hat{\boldsymbol{r}}$, Eq. (3) can be written as [78]:

$$dW_{ab} \propto |\boldsymbol{e_k}\cdot\langle a|\,\hat{\boldsymbol{D}}\,|b\rangle\,|^2\,d\Omega. \tag{4}$$

After integration over the solid angle, the final formula for the electric dipole transition rate γ_{ab} from state $|a\rangle$ to $|b\rangle$ reads as follows:

$$\gamma_{ab} = \int dW_{ab} = \frac{4\omega^3}{3c^3}|\,\langle a|\,\hat{\boldsymbol{D}}\,|b\rangle\,|^2. \tag{5}$$

The matrix element in Eq. (5) can be rewritten with the *Wigner-Eckart theorem* (see, e.g., Ref. [101]). When writing down the quantum number of the states $|a\rangle = |nJM\rangle$ and $|b\rangle = |n'J'M'\rangle$ from (5) explicitly, it yields [78]:

$$\gamma_{ab} = \frac{4\omega^3}{3c^3}\frac{1}{2J+1}\,|\,\langle nJ|\,|D|\,|n'J'\rangle\,|^2 \tag{6}$$

Here, $\langle nJ|\,|D|\,|n'J'\rangle$ denotes the so-called *reduced dipole matrix element* and J is the total angular momentum of the initial state. Please note that the reduced matrix element is not a vector quantity anymore as opposed to the previous matrix elements. Therefore, the electric dipole operator is denoted as a scalar correspondingly. This is due to the *Wigner-Eckart theorem*, which shows that a ME can be reduced by factoring out the dependency on the magnetic quantum number M [78]. This essentially accounts for the fact that every direction in space is equivalent, and it therefore should not matter in which direction the dipole operator is pointing. Using the dipole operator leads to the electric dipole selection rules with $\Delta J = 0, \pm 1$ (except $J = 0 \rightarrow J' = 0$). Additionally, the two states must have opposite parity [78].

The element $\exp(-i\,\vec{k}\cdot\vec{r})$ in the field expansion (see Eq. 2) can be expanded further in powers of $(\vec{k}\cdot\vec{r})$, leading to higher electric and magnetic multipole moments [78]. The electric dipole matrix element is also often briefly denoted as the E1 matrix element, owing to the fact that it is the first term in the expansion of the electric field. The electric quadrupole matrix element is denoted as E2 correspondingly, whereas the magnetic dipole matrix element is denoted shortly as M1, etc. If no E1 transition exists between two states, this transition is called a *forbidden transition*. In that case, E2 and/or M1 (or higher) transitions mainly contribute to the transition rate. On the other hand, if an E1 transition is possible, this transition is denoted as *allowed*. The rates of forbidden transitions are usually much smaller, and hence the lifetimes of the corresponding states much longer. For further details on the expansion of the electromagnetic field as well as matrix elements, please inspect Refs. [7, 78, 122].

C. Lifetimes

For their application in atomic clocks, it is helpful to study the lifetimes of states. The lifetime of an excited state is defined as the average time it will take for this state to transition into a state with lower energy. The lifetime τ_a can be calculated by the inverse of the sum over all possible transition rates γ_{ab_i} (see Eq. 6) from the initial state $|a\rangle$ to lower states $|b\rangle_i$. The according formula can be written as:

$$\tau_a = \frac{1}{\sum_{(\epsilon_{b_i}<\epsilon_a)}\gamma_{ab_i}} \tag{7}$$

States with allowed (E1) transitions typically have lifetimes in the range of nanoseconds. However, states with forbidden transitions have typical lifetimes on the order of seconds. Most often, E2 transitions are used for OACs [44, 85]. Some clocks, such as concepts using Yb^+, also utilize electric octupole (E3) transitions [43].

D. Polarisabilities

The polarisability is the atomic response to an external electric field. Polarisabilities are important for studying various environmental influences on atoms and ions. External factors such as black-body radiation or the electromagnetic field of an ion trap will perturb the atomic energy levels and will therefore induce shifts in the transition frequencies. These types of shifts are, in fact, the largest source of uncertainty for the new generation of optical frequency standards [91]. Therefore, accurate knowledge of those quantities is of uppermost importance for their application. This section is oriented closely at Ref. [91], which can be inspected for further information.

The polarisability is defined via the action of an external electric field $\vec{\boldsymbol{F}}$ on a charge distribution. An electric field will induce an electric dipole moment to such a distribution. The relation between those quantities is given by the following formula [91]:

$$\vec{\boldsymbol{d}} = \alpha\, \vec{\boldsymbol{F}} \tag{8}$$

The proportionality factor α (not to be confused with the fine structure constant) is referred to as the polarisability. A non-zero polarisability leads to an energy shift ΔE of an energy level:

$$\Delta E = -\frac{1}{2} \vec{\boldsymbol{F}} \cdot \alpha \vec{\boldsymbol{F}}. \tag{9}$$

The total polarisability α is given by the sum of the so-called scalar polarisability α_0 and the tensor polarisability α_2 [91]:

$$\alpha = \alpha_0 + \alpha_2 \frac{3M^2 - J\,(J+1)}{J\,(2J-1)}. \tag{10}$$

Here, J denotes the angular momentum and M is the magnetic projection. A scalar polarisability implies that the induced dipole moment is pointing in the same direction as the external field. This is true for spherically symmetric states (such as $s_{1/2}-$ or $p_{1/2}-$states) because α_2 does not contribute for them [91]. For all non-spherically symmetric states, α_2 will generally be non-zero, and therefore the total polarisability depends on the magnetic projection M. This accounts for the fact that the direction and magnitude of the resulting dipole moment can be dependent on the direction of the external field. Via second-order perturbation theory, the static polarisability can be calculated as:

$$\alpha_0 = \frac{2}{3\,(2J+1)} \sum_n \frac{|\,\langle\psi|\,|D|\,|\psi_n\rangle\,|^2}{E_n - E}. \tag{11}$$

where J is the angular momentum quantum number of the initial state $|\psi\rangle$ with the corresponding energy E [91]. The sum runs over all other states $|\psi_n\rangle$, with energies E_n, and $\langle\psi|\,|D|\,|\psi_n\rangle$ is a reduced E1 matrix element (see section II B). Equation (11) is often referred to as the 'sum-over-states' formula in the literature, since it runs over all possible states, including the continuum [91]. As can be inferred from the formula, it is crucial to precisely determine E1 matrix elements and especially the energy levels in order to provide accurate values for the polarisability. Although the sum runs over all states, in practice often the first few lowest-lying valence states dominate in their contribution and the continuum could be taken out of the calculation [91]. However, for some excited states this may not be the case and their contribution is important for high-precision calculations. Therefore, all those contributions are included in the calculations carried out for this thesis. This is incorporated by using a finite basis set, resulting in a finite sum in formula (11). This is equivalent to the inclusion of all bound and continuum states [91]. So far, we implicitly

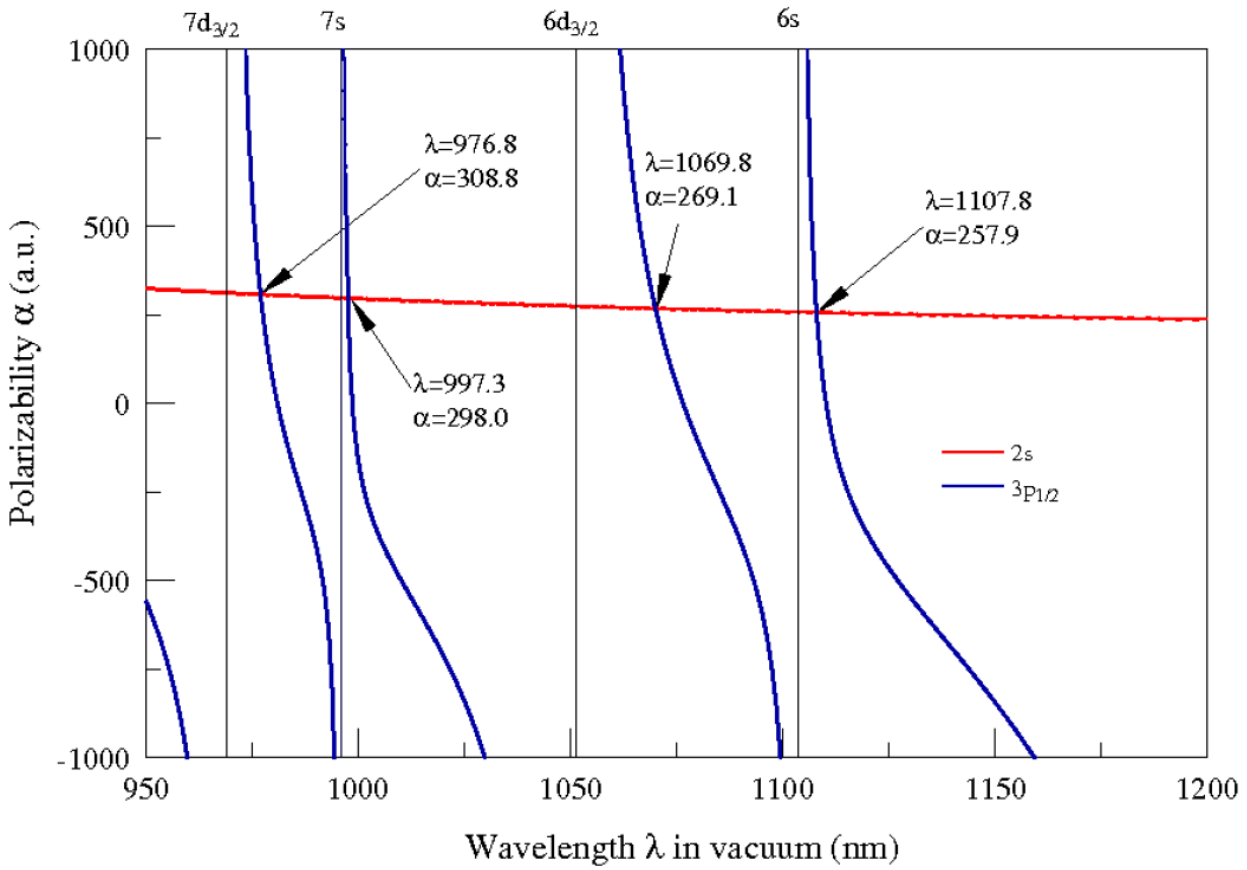

FIG. 5: This graphic shows a representative plot of the dynamical polarisability over the wavelength of the external electric field. In this case, it shows a calculation for the $2s - 3p_{1/2}$ transition in Li. Taken from the review article in Ref. [91].

only considered static electric fields. In a non-static field with frequency ω, the formula for the scalar polarisability only needs to be adjusted slightly and can be given via [91]:

$$\alpha_0(\omega) = \frac{2}{3\,(2J+1)} \sum_n \frac{\Delta E_n \;|\,\langle\psi|\,|D|\,|\psi_n\rangle\,|^2}{{\Delta E_n}^2 - \omega^2} \tag{12}$$

Here, ΔE_n is defined as $\Delta E_n = E_n - E$. Please note again the use of atomic units. As can be inferred from the formula, it is possible for the polarisability to diverge if the frequency reaches values of $\omega_n = |\Delta E_n|$. These values are called *resonances*. Furthermore, they can be determined experimentally and used to compare with calculations in order to determine the accuracy of the underlying theory [91]. The formula of the tensor polarisability can be similarly adjusted for alternating fields (see, e.g., Ref. [91]). Figure 5 shows a representative plot of the scalar polarisability (of Li) over the wavelength of an external electric field. The divergences in the scalar polarisability can be seen very well, with its value going to $-\infty$ from one side and to $+\infty$ from the other side.

Magic Wavelengths

An interesting phenomenon arising in the presence of alternating electric fields are so-called *magic wavelengths* [2, 91]. As we know, a transition occurs between two states, let us call them $|1\rangle$ and $|2\rangle$. We denote their unperturbed transition frequency by ν_0 (as in Fig. 3). An external AC field will perturb each energy level (see Eq. 9) differently since their polarisabilities are usually different. Hence, it follows that $\Delta E_1 \neq \Delta E_2$ in general. This further implies that the transition frequency will change accordingly. For the perturbed transition frequency $\nu_{pert.}$ it follows that $\nu_{pert.} \neq \nu_0$, if $\Delta E_1 \neq \Delta E_2$. For most transitions, there exists a magic wavelength λ_m (or more) where the polarisabilities of state $|1\rangle$ and $|2\rangle$ are the same, which implies $\Delta E_a = \Delta E_b$. This means that both energy levels are shifted by an equal amount due to the external electric field. In this case, even though both energy levels are perturbed, the transition frequency will not change since it is only dependent on the energy difference of those levels, which is not affected at this particular wavelength. Therefore, if an electric field with $\omega = \omega_m$ is applied, $\nu_{pert.} = \nu_0$ will hold. Knowledge of those frequencies can be used to adjust the necessary external fields (e.g. from ion traps) accordingly in order to minimise their influence on certain transitions. Furthermore, these wavelengths can be used to gauge the accuracy of a given theory, especially for the calculation of polarisabilities, since they may be measured with high accuracy [91].In practice, only magic wavelengths that are far enough away from resonances are utilised since otherwise one of the states could be shifted by an induced transition if the wavelength is not tuned perfectly to λ_m [70]. In Fig. 5 the corresponding magic wavelengths are indicated by arrows.

E. Hyperfine Constants

This section will be closely oriented at Ref. [122]. The hyperfine splitting of spectral lines is caused by electric and magnetic moments of the nucleus. The dominant contributions arise from the magnetic dipole and electric quadrupole moments [122]. This effect will be explained non-relativistically for the purpose of simplification. Nuclear magnetic moments are commonly expressed in units of the nuclear magneton, defined by

$$\frac{e\hbar}{2m_p c} = \left(\frac{m}{m_p}\right)\mu_B \tag{13}$$

where μ_B is the Bohr magneton and m_p is the proton mass. The magnetic moment of the nucleus can further be given by the gyromagnetic ratio:

$$\boldsymbol{\mu} = g_I \boldsymbol{I} \tag{14}$$

where $\boldsymbol{I}$ indicates the nuclear spin.

Electric quadrupole moments are the second important quantity of the nuclear structure. The quadrupole moment tensor Q_{ab} can be defined as:

$$Q_{ab} = \sum_{\alpha,\,\beta} \rho\,(3\,r_a r_b - \delta_{ab}\,r^2)\,\mathrm{d}r \tag{15}$$

where the sum runs over all protons and $\alpha, \beta \in \{x, y, z\}$ [122]. For convenience, the magnitude of the quadrupole moment is usually described by the expectation value of the tensorial Q_{zz} component via the relation:

$$Q = \langle \gamma I M |\, Q_{zz}\, | \gamma I M \rangle_{M=I}\,. \tag{16}$$

where the state I with its magnetic projection $M = I$ is chosen and γ is the triaxial deformation parameter of the nucleus. Eq. (16) is usually much easier to evaluate in spherical coordinates. With some algebra, this amounts to:

$$Q = \langle \gamma I | \, | Q_{zz} | \, | \gamma I \rangle \, \sqrt{\frac{I(2I-1)}{(2I+3)(2I+1)(I+1)}} \tag{17}$$

where $\langle \gamma I \, | \, | Q | \, | \, \gamma I \rangle$ is a reduced matrix element. For more details see, e.g., Ref. [122].
For nuclei with non-zero magnetic dipole and electric quadrupole moments, an additional interaction with the electron shells has to be taken into account:

$$W = W_\mu + W_Q = -\boldsymbol{\mu} \cdot \boldsymbol{B} + \frac{e}{6} \sum_{\alpha,\,\beta} Q_{\alpha\beta} \, \frac{\partial^2 \varphi}{\partial x_\alpha \, \partial x_\beta} \tag{18}$$

here, $\boldsymbol{B}$ and φ are the magnetic field and the electrostatic potential created by the electrons at the nucleus. This interaction leads to the hyperfine splitting of a level with angular momentum $\boldsymbol{J}$ into multiple components. Each of these components corresponds to a definitive value of the total angular momentum $\boldsymbol{F}$ of the atom:

$$\boldsymbol{F} = \boldsymbol{I} + \boldsymbol{J} \tag{19}$$

It should be mentioned that, because of the interaction described by Eq. (18) neither $\boldsymbol{I}$ nor $\boldsymbol{J}$ is conserved individually anymore. Only their vector sum $-\,\boldsymbol{F}\,-$ remains conserved.

Let's consider the first (magnetic) interaction term in Eq. (18) for example. Its mean value can be given by:

$$\begin{aligned} W_\mu &= -\langle \boldsymbol{\mu} \cdot \boldsymbol{B} \rangle = -g_I \, a \, \langle \boldsymbol{I} \cdot \boldsymbol{J} \rangle = A \, \langle \boldsymbol{I} \cdot \boldsymbol{J} \rangle = \frac{1}{2} A \, \langle \, \boldsymbol{F}^2 - \boldsymbol{I}^2 - \boldsymbol{J}^2 \rangle \\ &= \frac{1}{2} A \, [\, F(F+1) - J(J+1) - I(I+1)] \end{aligned}$$

where $F = J + I,\, J + I - 1,\, ...,\, |J - I|$. By replacing $\{J, I, F\}$ with $\{L, S, J\}$, the corresponding formula for the spin-orbit coupling can be seen immediately.
It follows from Eq. (18) that, in order to determine the Hyperfine A and B Constants, it is necessary to know the values of the magnetic field and of the second derivatives of the electrostatic potential at the position of the nucleus [122]. Without proof, the resulting expression for the total hyperfine splitting of an energy level can be given in the following form:

$$\Delta E_F = \frac{1}{2} \, A \, C + B \, C \, (C+1), \tag{20}$$

$$C = F \, (F+1) - J \, (J+1) - I \, (I+1) \tag{21}$$

where the constant A depends on the magnetic field generated by the electrons and B is dependent on the electric field gradient of the electrostatic field [94]. The calculation of both types of Hyperfine Constants involves the calculation of the reduced matrix elements, which are crucial for their accuracy [122]. For the respective formulae, please inspect Refs. [94, 122].

F. Field Shifts

The Field Shift is an energy correction that arises from the change in nuclear radius from one isotope to the next [78, 122]. Good knowledge of it is important for studies of possible variations of fundamental constants as well as dark matter searches [4, 66]. For example, small fluctuations of fundamental constants will lead to small variations in the nuclear radius and therefore impact the spectra. Most studies thereof have been carried out with $^{171}\mathrm{Yb}^{+}$ atomic clocks. Radium clocks are known to be particularly sensitive to these shifts as well, which could help further investigations of these effects [39].

When the number of neutrons in the nucleus is increased, its size accordingly increases as well. This can be parametrised as:

$$\delta E = -F\,\delta\langle r^2\rangle \tag{22}$$

where $\delta\langle r^2\rangle$ is the change in the root-mean-square of the nuclear radius and F is the so-called Field-Shift Constant [78]. For example, for a uniform charge distribution of radius R, the mean square radius is related to R^2 by [78]:

$$\langle r^2\rangle = \frac{3}{5}R^2. \tag{23}$$

With some algebra, it can be shown that the change in nuclear potential δV can be calculated as:

$$\delta V = \frac{5Z}{4R^3}\left[1-\frac{r^2}{R^2}\right]\delta\langle r^2\rangle,\;\; r \le R. \tag{24}$$

for this particular distribution. This allows us to introduce the single-particle operator $F(r)$:

$$F(r) = \begin{cases} \frac{5Z}{4R^3}\left[1-\frac{r^2}{R^2}\right], & r \le R \\ 0, & r > R \end{cases} \tag{25}$$

and to further determine the field-shift constant F as its expectation value [78]:

$$F = \langle F(r)\rangle. \tag{26}$$

For atomic structure calculations, the assumption of a uniform charge density is usually replaced by the Fermi distribution (as for the calculations carried out here), which is given by:

$$\rho_{nuc}(r) = \frac{\rho_0}{1+e^{(r-c)/a}} \tag{27}$$

where a and c are parameters. $t = 4\,a\,ln(3)$ is the so-called *skin thickness* and c is the *half-density radius* (see, e.g., Refs. [67, 78]). ρ_0 is found via the normalisation condition $\int \rho(r)\ \mathrm{d}^3r = 1$, with the corresponding charge distribution given by $Z\,e\,\rho(r)$. For further information, please inspect, for example, Refs. [78] and [122].

III. COMPUTATIONAL METHODS

This chapter will mainly discuss the computational methods that were utilised throughout this study. Essentially, we need to solve the Dirac equation, since relativistic effects become increasingly important for heavy atoms [110]. We will give a brief overview of the different orders of approximations, starting with the Relativistic Hartree-Fock (RHF) method, which is our lowest-order approximation. At the next order, we include the Random Phase Approximation (RPA), which accounts for the polarisation of the core electrons. Additionally, we account for electronic correlations by adding a correlation potential – Σ – to the Dirac-Hamiltonian. Further contributions include quantumelectrodynamical (QED) effects as well as the Breit interaction and Structure Radiation + Normalisation (SR+N) effects. In the case of Ra^+, we cannot solve the Dirac equation exactly since we are looking at a many-body problem. Therefore, dedicated perturbation techniques are necessary, which will be illustrated in the following sections. All units will be given in atomic units ($\hbar = e = m_e = c\alpha = 1$) if not stated otherwise. According references will be provided in case more detailed explanations are desired.

A. Relativistic Hartree-Fock (RHF) Method

At the lowest order, we are using the Hartree-Fock approach. Here, we assume that each of the N electrons moves independently in the nuclear Coulomb field and the average field of the remaining $(N-1)$ electrons[7]. It can be viewed as a variational method in which the wavefunctions of a many-electron system are given in the form of an antisymmetric product of single-particle wavefunctions [78]. I will outline this approach for the case of single-valence systems. We can further consider the nucleus as being fixed in space, in order to solve the Dirac equation for the electronic system in the static field on the nucleus. This is justified because the nucleus is much heavier than the electrons and hence its velocity is much lower [124]. This approach, commonly known as the 'Born-Oppenheimer approximation', essentially treats the nucleus as having an infinite mass and an infinitesimally small nuclear radius. For the treatment of finite-mass and-size effects, the so-called mass and field shifts (as carried out in this study) can be calculated. The corresponding Hamiltonian of the Dirac equation $\hat{H}\psi = E\psi$ for N electrons can be given by the sum:

$$\hat{H} = \sum_{i}^{N} \hat{h}_0(\vec{r}_i) + \sum_{i<j} \frac{e^2}{r_{ij}} \tag{28}$$

with $\hat{h}_0$ being the single-electron Dirac Hamiltonian including the single-particle kinetic energy and the nuclear potential [124]. The second term accounts for the electron-electron interaction due to the Coulomb potential, with $r_{ij} = |\vec{r_i} - \vec{r_j}|$. However, for systems with $N > 1$, the Dirac equation cannot be solved exactly due to the Coulomb term, since it involves 2 particles [105]. Therefore, this term needs to be approximated. If one can find a good approximation to the Coulomb potential – let's denote this approximation $\hat{V}_{avg}$ – the deviation $\delta\hat{V}$ from it will be small. This allows us to use an iterative approach [78]. An approximation to the Coulomb potential may be given by the average potential seen by the i-th electron due to the other $(N-1)$ electrons. This average potential is sometimes also called the *mean-field potential* and is only dependent on the i-th electrons coordinates since the average is calculated by integrating over all other coordinates. With this approach, correlations between electrons are neglected to some extent, in particular the

[7] This is also commonly known as the 'independent-electron approximation'.

Coulomb repulsion beyond the mean-field approximation [124]. However, these correlation effects can be effectively included afterward via different means ([78]) such as the so-called *Correlation Potential Method*, which will be described in Subsec. III E. $\delta\hat{V}$, which is also known as *residual Coulomb interaction*, can be given by [78]:

$$\delta\hat{V} = \sum_{i<j} \frac{e^2}{r_{ij}} - \sum_{i}^{N} \hat{V}_{avg}^{(i)}(\vec{r_i}) \tag{29}$$

Here, $\hat{V}_{avg}^{(i)}(\vec{r_i})$ is the average potential seen by the i-th electron. This allows us to rewrite the many-body Hamiltonian $\hat{H}$ as a full sum of single-particle Hamiltonians $\hat{h}_{HF}$, which is given by:

$$\hat{h}_{HF} = c\,\boldsymbol{\alpha}\cdot\hat{\boldsymbol{p}} + c^2\,(\beta-1) + \hat{V}_{nuc} + \hat{V}_{HF} \tag{30}$$

Here, $\hat{V}_{nuc}$ is the nuclear potential. To form it, we assume a Fermi distribution of the charge density, as shown in Eq. (27). Please note that we have subtracted the rest energy of the electron in Eq. (30) for convenience since it effectively acts as a constant energy shift. Hence, we have a term $(\beta-1)$. The terms $\boldsymbol{\alpha}$ and β in Eq. (30) denote 4×4 Dirac matrices, with $\boldsymbol{\alpha} = \gamma^0\boldsymbol{\gamma}$, $\beta = \gamma^0$ [101]. From now on, we will denote the average potential for a single electron as the Hartree-Fock potential $-\hat{V}_{HF}$. To be more precise, it can be defined as:

$$\hat{V}_{HF}\,\Phi_a(\vec{r}_1) = \sum_{i\neq a}^{N-1}\left(\int \frac{\Phi_i^\dagger(\vec{r}_2)\,\Phi_i(\vec{r}_2)}{r_{12}}\,\mathrm{d}\vec{r}_2\,\Phi_a(\vec{r}_1) - \int \frac{\Phi_i^\dagger(\vec{r}_2)\,\Phi_a(\vec{r}_2)}{r_{12}}\,\mathrm{d}\vec{r}_2\,\Phi_i(\vec{r}_1)\right) \tag{31}$$

where the sum over i extends over all $(N-1)$ occupied electrons [106]. Φ_i denotes their corresponding single-particle wavefunctions. The two terms in Eq. (31) are the so-called direct (or Hartree) and exchange parts [124]. As mentioned previously, we have to guess an initial approximation for the Coulomb potential. We can then use this guess to calculate electronic wavefunctions. Using these newly calculated wavefunctions, we can construct a new Hartree-Fock potential, which will generally lead to a better approximation than the previous one. This means that Eq. (30) correspond to a 'self-consistency problem' since its eigenfunctions appear in the potential term $\hat{V}_{HF}$ as well [124]. This approach can be used iteratively until we reach a satisfactory level of convergence. In the ideal case, $\hat{V}_{HF}$ will be made up of the same wavefunctions that solve the Hamiltonian itself, and hence, is self-consistent. Therefore, this method is also commonly known as *self-consistent field method* [78, 124].

The atomic wavefunctions can then be given as a linear combination of one or more Slater determinants of the calculated single-particle orbitals. In practice, the wavefunction for an atomic core is most often assumed to consist of a single Slater determinant, as in our case [105]. In theory, including multiple Slater determinants is more accurate, but at this point not feasible in terms of computational resources. The effects on excitations can be much more efficiently included by the means of the so-called Correlation Potential Method, which will be described more closely in Sec. III E. For single-valence systems, the Hartree-Fock approach leads to accuracies of around 10% between the RHF eigenvalues and the experimental energies, as in the case of Cesium [78]. By inclusion of an additional correlation potential (see Sec. III E), the accuracy can be improved to a level of around 0.1%. Using the Hartree-Fock method, we solve for s and p valence states up to $n = 8$ and d valence states up to $n = 6$ for Ra^+. For atoms in line 6 of the periodic table (e.g. Ba^+) we solve for up to $7sp$ and $5d$ valence states.

B. Grid parameters

For all our calculations, we used a so-called *log-linear* radial grid r_i in a region between r_0 and r_{max}. The non-uniformly spaced radial grid r_i can be defined in terms of a uniformly spaced u_i grid as:

$$u = r + \ln(r) \;\text{ with }\; \frac{\mathrm{d}r}{\mathrm{d}u} = \frac{r}{r+1} \tag{32}$$

It features a point distribution that is approximately logarithmic close to the origin and nearly linear for large radii [106]. I used a minimum radius of $r_0 = 10^{-6}\,a_B$ and a maximum radius of $r_{max} = 140\,a_B$ with 5000 points.

C. Basis parameters

For the correlation potential method (see Sec. III E) as well as the diagrammatic RPA method (see Sec. III D), it is necessary to use a discrete basis consisting of a set of Hartree-Fock eigenvalues. This helps, for example, to reduce infinite sums and integrals over the real spectrum (consisting of bound states, positive-energy continuum of scattering states, and the negative-energy continuum of positron states) to finite sums over a *pseudospectrum* [78, 108]. Our calculations were performed using the so-called *dual-kinetic-balance B-spline basis* (see [5]), which offers a high level of convergence and stability [56, 60, 107]. We used 45 splines of order 7 in a large but finite cavity of $30\,a_B$. Using this basis, we store states up to $n = 40$ for $l \in \{s, p, d, f, g, h, i\}$. It is very important that the basis is orthogonal to the wavefunctions of the occupied core electrons. Therefore, we verified that basis truncation errors are insignificant.

D. Core Polarisation (RPA)

In the presence of an external field with frequency ω (e.g., the electric field of a laser), the atomic orbitals will be perturbed. This can by expressed via the (single-particle) interaction Hamiltonian:

$$\hat{h}_f = \hat{f}\, e^{-i\omega t} + \hat{f}^\dagger\, e^{i\omega t} \tag{33}$$

Consequently, the total interaction Hamiltonian is given as the sum of all single-particle interaction Hamiltonians: $\hat{H}_f = \sum_i \hat{h}_{f_i}$ [105]. The atomic orbitals then transform as [23]:

$$\psi \longrightarrow \psi + \delta\psi = \psi + X e^{-i\omega t} + Y e^{i\omega t} \tag{34}$$

where ψ is the unperturbed orbital. X and Y are corrections due to the field and are not usually states of definite angular momentum [107]. The energy will transform as $\epsilon \longrightarrow \epsilon + \delta\epsilon\,(e^{-i\omega t} + e^{i\omega t})$. This effect is often referred to as core polarisation. The resulting perturbation requires a modification of the Hartree-Fock potential. For electric dipole matrix elements, we take it into account by using the time-dependent Hartree-Fock (TDHF) method (see, e.g., Refs. [23, 25, 26]). This method is equivalent to the random phase approximation with exchange (as in Ref. [77]) and is therefore often also referred to simply as random phase approximation. To first order, the corrections satisfy the time-dependent Hartree-Fock equations:

$$(\hat{h}_{HF} - \epsilon - \omega)\, X = -(\hat{h}_f + \delta\hat{V} - \delta\epsilon)\, \psi_c \tag{35}$$

$$(\hat{h}_{HF} - \epsilon + \omega)\, Y = -(\hat{h}_f^\dagger + \delta\hat{V}^\dagger - \delta\epsilon)\, \psi_c \tag{36}$$

with $\delta\epsilon = \langle\psi_c|\,\hat{h}_f + \delta\hat{V}\,|\psi_c\rangle$ and ψ_c denoting the wavefunction of the core electrons [23]. $\delta\hat{V}$ is the resulting correction to the RHF potential (see previous section):

$$\delta\hat{V} = \hat{V}_{HF}(\{\psi_c + \delta\psi_c\}) - \hat{V}_{HF}(\{\psi_c\}) \tag{37}$$

The TDHF equations are solved self-consistently for all electrons in the occupied core. Since those equations are iterated until convergence is reached, core polarisation is included in the Coulomb interaction up to all orders. Matrix elements are calculated as $\langle w|\,\hat{h}_f + \delta\hat{V}\,|v\rangle$ [23]. In the case of a field with frequency ω driving a E1 transition, $\hat{h}_f = \hat{\boldsymbol{d}} = -e\,\hat{\boldsymbol{r}}$, and $\delta\epsilon = 0$. It should be noted that we only used the TDHF method for the calculation of E1 matrix elements. This method gives an important contribution of around 10%. For E2 and M1 matrix elements, although, this approach does not always converge. Therefore, we use a more computationally expensive approach, which is called the *diagrammatic random phase approximation with exchange* for these MEs. For more details on this approach, please inspect Refs. [59, 83, 106].

E. Correlation Corrections

Correlation corrections are deviations from the simplified single-particle picture of a multi-electron system. They correspond to electron-electron interactions between valence and core electrons beyond the mean-field approximation [105]. In order to include these effects, the Hartree-Fock procedure can be improved by adding back the electron-electron repulsion (Coulomb) term (see Eq. 29) in a perturbative manner. The resulting correction can, in principle, be computed directly, via a direct summation of the diagrams shown in Fig. 6 (see Ref. [22]). For this thesis, however, a more numerically stable method, developed in Ref. [24], was used: the Correlation Potential Method. It works by including a correlation potential ($\hat{\Sigma}$) in the single-particle Hartree-Fock Hamiltonian [24, 53]:

$$(\,\hat{h}_{HF} + \hat{\Sigma}\,)\,\psi^{(Br)} = \epsilon^{(Br)}\,\psi^{(Br)} \tag{38}$$

The $\hat{\Sigma}-$potential accounts for the screening of the Coulomb potential by the core electrons as well as for hole-particle interactions. It is often referred to as the self-energy operator. The resulting wavefunctions $\psi^{(Br)}$ are called Brueckner orbitals [78]. It should be mentioned that those Brueckner orbitals can be used in conjunction with the TDHF method (as well as the diagrammatic RPA) explained in the previous section. It is possible to calculate Σ to lowest (second) order in the Coulomb interaction using the four Goldstone diagrams presented in Fig. 6 [83]:

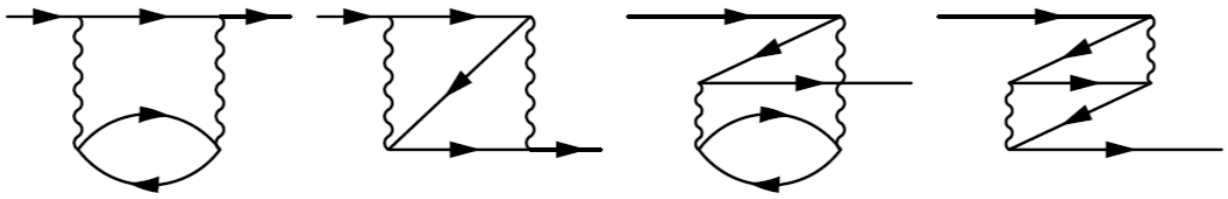

FIG. 6: Goldstone diagrams for the second-order energy correction in the Coulomb interaction. These were used for the second-order correlation potential $-\Sigma^{(2)}$. The forward time direction is from left to right. Backward facing lines denote states in the core (holes) and forward facing lines represent particle states. Wiggly lines correspond to the Coulomb interaction. The 1^{st} and 3^{rd} diagram (from left to right) are the so-called direct diagrams whereas the 2^{nd} and 4^{th} one show the exchange diagrams. For more details, please inspect, e.g., Refs. [24, 29, 69, 83]. Graphic taken from [107].

We will refer to this second-order correlation potential as $\Sigma^{(2)}$ from now on.

For more accurate calculations, it is necessary to include correlation corrections beyond second order. This can be done using the so-called Feynman diagram technique developed in Refs. [54, 55], which allow us to include screening effects as well as hole-particle interactions up to all orders [53]. The so-called *All-Orders Method* will be outlined more explicitly in the following section.

F. All-Orders Method

The inclusion of second-order correlation effects greatly increases the accuracies of calculations for single-valence systems. However, this procedure generally overestimates these corrections [105]. Therefore, higher-order correlation effects must be taken into account for a more accurate treatment. Interestingly, the inclusion of third-order effects can in fact worsen the agreement with the experiment, as seen in the case of Cesium [108]. Hence, usually an all-orders approach is required. For this, I use the so-called *Correlation Potential in the Screened Coulomb Interaction (CPSCI) Method*[8] , which was developed in Refs. [27, 55]. It has already been successfully applied to atomic structure calculations for heavy atoms [108]. We will refer to its correlation potential as $\Sigma^{(\infty)}$ from now on. With the CPSCI method, three sets of dominating diagrams can be included up to all orders in perturbation theory. These correspond to the screening of the electron-electron polarisation due to core polarisation (shown in Fig. 7) as well as due to the electron-hole Coulomb interaction (Fig. 8). Furthermore, non-linear effects of the correlation potential are included [105].

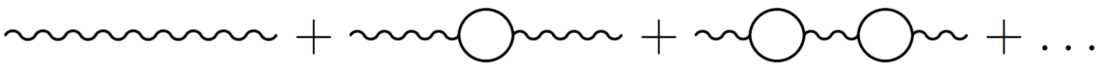

FIG. 7: Illustration of the screening of the Coulomb interaction by the polarisation of the core. Taken from [107].

For example, the largest correction to the second-order correlation potential arises due to the screening of the electron-electron potential by the core electrons [54]. The interactions between electrons and holes also give an important contribution, which is usually around half the size of the screening correction [55]. It should be mentioned that the polarisation loops describe an electron-hole pair because one electron is excited from the core, leaving a hole.

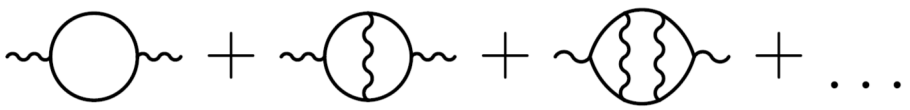

FIG. 8: Illustration of hole-particle corrections to the polarisation operator. Taken from [107].

Solving the Brueckner equation (Eq. 38) automatically incorporates a third category of diagrams to all orders, specifically the chaining of the $\Sigma-$operator (illustrated in Fig. 9) [53]. All remaining

[8] Sometimes, this method is also abbreviated as *PTSCI:* Perturbation Theory in the screened Coulomb interaction [108].

groups of diagrams are suppressed by a small parameter, allowing them to be safely disregarded [55]. This is especially true for s and p states, which are usually of most interest ([105]), such as in the case of Ra^+ and Sr^+ clock transitions. For further details on the correlation potential method, please inspect Refs. [25, 28, 53, 54, 83, 106].

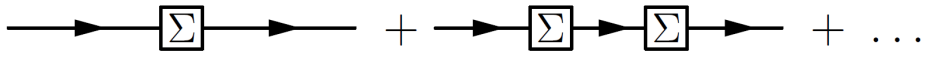

FIG. 9: Illustration of the chaining of the $\Sigma-$operator. Taken from [107].

Scaling of the Correlation Potential

Furthermore, we can introduce semi-empirical scaling factors to the correlation potential: $\hat{\Sigma} \longrightarrow \lambda\hat{\Sigma}$. These λ-factors are adjusted so that the eigenenergies $\epsilon_i^{(Br)}$ (see Eq. 38) of each valence state in the basis reproduce the experimental energies:

$$(\,\hat{h}_{HF} + \lambda_i\,\hat{\Sigma}\,)\,\psi_i^{(Br)} = \epsilon_i^{(Br)}\,\psi_i^{(Br)} \tag{39}$$

The experimental values we used were obtained from the *NIST Atomic Spectra Database* ([98]). This procedure usually leads to an improvement in accuracy and can be done up to all orders. For $\Sigma^{(\infty)}$, the scaling factors are usually very close to 1, due to the high precision of the *ab initio* results. For Ra^+ for example, they mostly deviate in the %-range whereas at the level of $\Sigma^{(2)}$ the deviation will be in the range of about $\pm 20\%$. The factors for the $7s$, $8s$, and $7p_{3/2}$ states in Ra^+ for the scaled all-orders potential are, e.g., $\lambda_{7s} = 0.9755$, $\lambda_{8s} = 0.9980$, and $\lambda_{7p_{3/2}} = 0.9783$. For $\lambda\Sigma^{(2)}$ they were calculated to be $\lambda_{7s} = 0.7574$, $\lambda_{8s} = 0.7724$, and $\lambda_{7p_{3/2}} = 0.8208$. Lighter atoms and ions (such as Cs, Ba^+, Sr^+) usually feature an even smaller deviation.

G. Spectrum parameters

For calculations of the polarisability, we use a so-called spectrum, which is similar to the previously mentioned basis. The main difference lies in their calculation. In the spectrum, when using the Correlation Potential Method (see Sec. III E), we have to use the same $\Sigma-$operator for the whole spectrum. Hence, if we want to scale the correlation potential for the spectrum, we can only use a single scaling factor for all states. Whereas for the basis, we have the option to use different scaling factors for different valence states. This can lead to lower accuracies when calculating polarisabilities, for example because of the important contribution of the energy denominator (see Eq. 11). Therefore, when possible we have an option in AMPSCI to replace the spectrum with the basis states. Of course, this is only possible for the valence states which have been included in the basis. This generally incorporates the dominant contributions, so the error is usually negligible.
For the spectrum, we used 100 splines of an order of 9 in a cavity of $90\,a_B$. We used a cut-off ratio of $r_{0,\epsilon} = 10^{-8}$ and s, p, d, and f states up to $n = 95$.

H. Coupled-Cluster Methods

The Coupled-Cluster (CC) calculation method is a very common alternative to the CPSCI method described above. In fact, it is used far more frequently. Although it was not applied in this thesis, it will be briefly explained for the sake of completeness and comparison. It should be mentioned at this point that all other groups' calculations that we will compare our calculations to have used some sort of Coupled-Cluster method. In this method, the many-body wavefunction is presented as:

$$\left|\psi\right\rangle = \exp(S)\left|\psi^{(0)}\right\rangle \tag{40}$$

where $\left|\psi^{(0)}\right\rangle$ is the lowest-order atomic wavefunction [11]. The operator S consists of so-called 'cluster contributions'. For N electrons, it involves excitation terms from single-, double- and up to N- electron excitations. The operator S can be separated into those distinct parts as: $S = S_1 + S_2 + ... + S_N$ where S_n denotes the n-body excitations [91, 108]. Accordingly, the exponential term in Eq. (40) can be expanded into:

$$\left|\psi\right\rangle = \{\, 1 + S_1 + S_2 + S_3 + \frac{1}{2}S_1^2 + S_1S_2 + \frac{1}{2}S_2^2 + ... \,\}\left|\psi^{(0)}\right\rangle \tag{41}$$

Actual implementations of the coupled-cluster approach vary significantly amongst groups. The main source of variation is in the order of the excitations that are included. Most include single and double excitations (usually abbreviated 'CCSD'). In order to achieve high accuracies, some dominating triple excitations have to be included as well, which are usually treated perturbatively and are very computationally intensive [18, 103]. Those calculations are commonly abbreviated as 'CCSDpT'[9]. Nonetheless, even with this approach they are still not always accurate. Higher excitations are generally not included, as the calculations blow up in complexity. Further variation lies in the usage of different non-linear terms as well as different basis sets. For example, in the 'linear CCSD' method, all linear terms including only single and double excitations are included for S:

$$\left|\psi\right\rangle = \{\, 1 + S_1 + S_2 \,\}\left|\psi^{(0)}\right\rangle \tag{42}$$

For a more detailed overview, please inspect, e.g., Refs. [108] and [91]. Refs. [10, 109] delve more deeply into the SDpT method whereas [100] and [103] include non-linear relativistic effects as well as a more complete treatment of triple excitations.

I. QED Corrections

For high-precision calculations it is important to include quantumelectrodynamical (QED) corrections resulting from vacuum polarisation and the electron self-energy. QED effects can have significant contributions to matrix elements [63, 68]. We incorporate them by adding the radiative potential to the Hamiltonian, which is given by [65]:

$$V_{rad} = V_{Ueh} + V_h + V_l + i\,(\boldsymbol{\gamma}\cdot\boldsymbol{n})\,V_m. \tag{43}$$

This is often referred to as *radiative potential method* and approximately accounts for one-loop radiative QED. The radiative potential is given by the sum of the Uehling (accounting for vacuum

[9] 'pT' here stands for 'partial triples'.

polarisation), high- and low-frequency electric self-energy, and magnetic self-energy potentials. A full expression including finite-size effects of the core can be found in Ref. [68]. By this method, QED corrections can be included in the atomic wavefunctions and therefore also into matrix elements [32, 63, 65]. Including V_{rad} into the RHF equation (see. Eq. 30) leads to important contributions for states with $l > 0$, commonly referred to as 'core relaxation' [17, 63, 68, 107].

J. Breit Interaction

Further lowest-order relativistic corrections to the Hartree-Fock Hamiltonian can be included by adding a so-called 'Breit Hamiltonian' [7, 78]. With this additional term, fine-structure corrections can be understood more precisely [78]. This incorporates the lowest-order relativistic effects, resulting from transverse photon[10] exchange between electrons. Physically it accounts for retardation effects due to the finite speed of light as well as magnetic interaction effects. Its effect is smaller by the order of $\alpha^2 Z^2$ than the Coulomb interaction ([78]) and enters as a correction to the Coulomb term in the many-body Hamiltonian as: $r_{ij}^{-1} \longrightarrow r_{ij}^{-1} + h_{ij}^B$. Here, h_{ij}^B denotes the Breit Hamiltonian. In the zero-frequency limit it can be expressed as:

$$h_{ij}^B = -\frac{\boldsymbol{\alpha}_i \cdot \boldsymbol{\alpha}_j + (\boldsymbol{\alpha}_i \cdot \boldsymbol{n}_{ij})(\boldsymbol{\alpha}_j \cdot \boldsymbol{n}_{ij})}{2\, r_{ij}} \tag{44}$$

with $\boldsymbol{n}_{ij} = (\boldsymbol{r}_i - \boldsymbol{r}_j)/r_{ij}$ [78]. In most cases, frequency-dependent effects can be neglected. However, these effects are increasingly important for highly charged ions [61, 78, 88]. Since we focus on single-charged ions, this is not of high importance for this study. Including h_{ij}^B into the Hamiltonian leads to a corresponding correction to the Hartree-Fock potential as: $V_{HF} \longrightarrow V_{HF} + V_B$. Including this potential in the RHF and TDHF equations allows for including Breit interaction effects into the calculations of wavefunctions and various other quantities [14, 15]. The inclusion of those effects in conjunction with correlation effects is very important for high-precision calculations, as demonstrated in Refs. [14, 15, 30]. In previous publications (e.g. [107]), it was shown that the treatment of the Breit contribution in AMPSCI corresponds well with the results of other groups.

Difficulties have been documented when trying to incorporate the Dirac-Coulomb Hamiltonian into calculations of high-order perturbation theory [78]. When using AMPSCI we can currently include the Breit interaction up to the second order in the correlation potential ($\Sigma^{(2)}$, see Sec. III E). In order to determine the Breit contribution to the matrix elements, we therefore evaluate it at the level of $\Sigma^{(2)}$. To include those contributions in the final result, we add them manually at the end. Contributions are added to the results of the fitted all-orders method (III F) including QED effects (III I).

For the calculation of matrix elements, it is important to fit to the experimental energies with the Breit contribution to the energies subtracted. This should be done since we already implicitly account for the Breit interaction if we are fitting to the experimental data and would otherwise risk double-counting to some degree. Adding the Breit contribution to scalar polarisabilities proves even more difficult due to the energies appearing explicitly in the denominator of their formulas (see Eq. 11). Those energies will change when including the Breit interaction in the Hamiltonian. Therefore, we cannot use the same procedure as for the matrix elements. In the case of polarisabilities, we fitted directly to the experimentally obtained energies instead. This will lead to small deviations in the matrix elements, but will generally lead to better results overall because of the high importance of the energy denominators.

[10] A transverse photon is characterised by its electric and magnetic field components being perpendicular to the direction of propagation.

K. Structure Radiation and Normalisation (SR+N)

Structure Radiation accounts for effects that involve external fields which act inside correlation diagrams (see Fig. 10). These terms cannot be included in the correlation potential method and therefore have to be considered separately [9, 25].

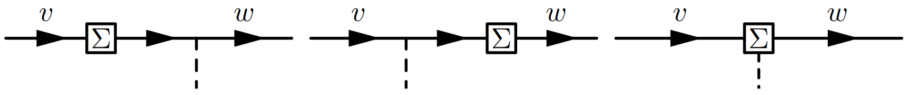

FIG. 10: Examples of correlation corrections. Here, Σ is the correlation potential, and dashed lines illustrate external fields. The first two (left and middle) diagrams are included automatically when calculating Brueckner orbitals whereas the third (right) diagram is included separately by Structure Radiation calculations. Taken from [107].

Expressions for SR can be found, e.g., in Refs. [80, 107]. Additionally, another correction known as normalisation of states enters at the same level. It arises from the change of the normalisations of many-body wavefunctions due to so-called configuration mixing [25, 79]. We calculate our many-body wavefunction ψ using a linear combination of core states ψ_c and valence states ψ_v:

$$|\psi\rangle = c_1\,|\psi_c\rangle \otimes |\psi_v\rangle \;+\; c_2\,\big(\,a\,|\psi_c\rangle\,\big) \otimes \big(\,a^\dagger|\psi_v\rangle\,\big) \;+\; \ldots \tag{45}$$

where a and $a^\dagger$ denote the quantum mechanical ladder operators. When calculating the valence states ψ_v we ensure that they are orthonormal: $\langle\psi_v|\psi_v\rangle \stackrel{!}{=} 1$. This, although, does not imply that $\langle\psi|\psi\rangle$ is automatically equal to 1 as well when excitations are included. This can be done using the following formula [25]:

$$\delta t^{\mathrm{N}}_{vw} = -\frac{t_{vw}}{2}\,\big[\,\langle v|\,\partial\Sigma/\partial\epsilon\,|v\rangle + \langle w|\,\partial\Sigma/\partial\epsilon\,|w\rangle\,\big]. \tag{46}$$

where t^k is an operator of rank k and v, w denote valence states. Furthermore, $\partial\Sigma/\partial\epsilon$ denotes the derivative of the Correlation potential with respect to the energy, and $t_{ij} = \langle i|\,|t^k|\,|j\rangle$.

Both structure radiation and normalisation corrections enter roughly at the same level ($\lesssim 1\%$) and generally tend to cancel. Nonetheless, they need to be included for high-precision calculations. For further information, please refer to Refs. [9, 25, 106].

Our calculations for SR+N contributions were carried out with the help of the *University of Queensland Research Computing Centre* on the high-performance computer *Bunya* because of their high computational demands ([99]).

L. Estimation of Theoretical Uncertainties

The estimation of uncertainties of theoretical data is of high importance. We estimate the errors in our calculations by comparing our results at different orders of approximation. Not only are they important for the analysis of certain experiments, such as possible variants of fundamental constants, but also they add value to recommended values. However, this is very difficult because it essentially involves the evaluation of certain quantities that are not known beforehand [108]. In order to estimate the variance due to missed correlation effects, we chose to use the full difference between the scaled all-orders method and the non-scaled method: $\delta\lambda := (\lambda\Sigma^{(\infty)} - \Sigma^{(\infty)})$. These corrections are mainly proportional to the $\Sigma-$potential and stem from the re-scaling process. Additionally, we include the full difference between the scaled all-orders and scaled second-order method $(\lambda\Sigma^{(\infty)} - \lambda\Sigma^{(2)})$. This should account for the approximate uncertainty due to higher-order (non-linear) effects. Finally, to include non-Brueckner type effects, we add half the Breit contribution (δBreit), 25% of the QED contribution (δQED) and 30% of the SR+N (δSR+N) contribution. These estimates were used for all calculations except for the sensitivity coefficients to α and the magic wavelengths, which were only compared between the second-order and all-orders correlation potential method. The total variance is accordingly the sum of the quadrature of all mentioned error estimations. We believe that these estimates are rather conservative and most likely overestimate SDs. From previous calculations using AMPSCI, e.g., for Cs (see [107]), we know that most of the experimental values for MEs are well within the estimated SDs of our calculations. This leads us to believe that these estimates will also be valid for similar atoms and ions where experimental data is more sparse, as in the case of Ra^+, Ba^+, and Sr^+.

IV. RESULTS AND DISCUSSION

We perform high-precision atomic structure calculations for various quantities of ionic valence states for Sr^+, Ba^+ and Ra^+ and compare them to other theoretical values and experiments when available. The focus will be mostly on the Radium and Strontium ion since both are currently being investigated for use as an optical atomic clock. Ba^+ is mainly shown as a proof of concept since it lies just below Ra^+ in the periodic table. Furthermore, for Ba^+ more experimental comparisons could be found than for the other two ions, which aids in estimating the accuracy of the calculations presented.

For Ra^+, we typically consider states up to $n_{\mathrm{Ra}^+,\{s,p\}} = 8$ for s and p orbitals, and $n_{\mathrm{Ra}^+,d} = 6$ for d orbitals. For the other ions, the chosen maximal principal quantum numbers follow a systematic reduction: $n_{\mathrm{Ba}^+,i}$ and $n_{\mathrm{Sr}^+,i}$ are set to be one and two units lower than $n_{\mathrm{Ra}^+,i}$, respectively. For the final values, we usually used the Correlation Potential Method up to all orders and included QED as well as Breit, Structure Radiation and Normalisation contributions. For better readability, all units will be given in atomic units if not stated otherwise.

A. Binding Energies

As shown in Table I, our results for the binding energies of the three investigated ions reveal that s and p states, in particular, can be calculated with high precision. For the highest order in the calculation presented, we used the non-scaled all-orders potential ($\Sigma^{(\infty)}$) including QED effects to which Breit and SR+N contributions were added.

The deviations from the experiment range from 0.00% up to 0.15% in magnitude at most for these states, showing very good agreement. For d states, the accuracy decreases noticeably, with deviations of 0.78% for both Ra^+ d states and $0.58\% - 0.59\%$ for these states in Sr^+, respectively. For Ba^+, we calculated the deviations to be $0.93\% - 0.94\%$ for these states. A possible reason for the larger deviations could be that correlation effects between electrons generally play a larger role in d states. For example, the presented d states feature a lower principal quantum number than the s and p states. Hence, d states are closer to the core and their orbitals have a higher overlap with the core electrons, leading to larger correlation effects. Therefore, if correlation effects are not precisely calculated, those deviations play a larger role in states with lower principal quantum number. Additionally, it is interesting to note that the deviations for all ions are qualitatively almost identical. This makes sense because their electronic structure is very similar as a result of all ions featuring a single valence electron above closed shells.

TABLE I: Calculated binding energies for various Sr^+, Ba^+, and Ra^+ valence states. Different orders of approximation are compared to experimental data, which were obtained from the NIST Atomic Spectra Database ([98]). For the final values, we used the non-scaled all-orders potential including QED effects and added Breit and SR+N contributions. All energies are given in units of cm^{-1}.

			Sr^+		
State	RHF	$\Sigma^{(\infty)}$	Final	Exp. [98]	Δ(%)
$5s_{1/2}$	−84042.19	−88919.69	−88911.97	−88965.18	−0.09
$6s_{1/2}$	−39906.33	−41194.73	−41191.51	−41228.65	−0.11
$5p_{1/2}$	−62512.11	−65269.82	−65248.92	−65249.99	0.00
$6p_{1/2}$	−32301.71	−33196.92	−33189.12	−33195.48	−0.02
$5p_{3/2}$	−61827.63	−64459.56	−64452.67	−64448.53	0.01
$6p_{3/2}$	−32043.79	−32905.37	−32902.54	−32907.28	−0.01
$4d_{3/2}$	−67385.18	−74785.05	−74829.66	−74409.28	0.58
$4d_{5/2}$	−67242.34	−74489.54	−74552.89	−74128.94	0.59

			Ba^+		
State	RHF	$\Sigma^{(\infty)}$	Final	Exp. [98]	Δ(%)
$6s_{1/2}$	−75339.65	−80774.28	−80722.56	−80686.30	0.04
$7s_{1/2}$	−36851.72	−38324.84	−38307.98	−38331.13	−0.06
$6p_{1/2}$	−57265.54	−60513.31	−60486.68	−60424.74	0.10
$7p_{1/2}$	−30240.11	−31312.31	−31302.25	−31296.48	0.02
$6p_{3/2}$	−55873.33	−58794.86	−58786.01	−58733.90	0.09
$7p_{3/2}$	−29698.96	−30686.06	−30682.28	−30674.96	0.02
$5d_{3/2}$	−68138.95	−76444.47	−76521.95	−75812.45	0.94
$5d_{5/2}$	−67664.76	−75611.96	−75710.11	−75011.49	0.93

			Ra^+		
State	RHF	$\Sigma^{(\infty)}$	Final	Exp. [98]	Δ(%)
$7s_{1/2}$	−75897.50	−81999.47	−81899.65	−81842.50	0.07
$8s_{1/2}$	−36859.93	−38440.60	−38409.07	−38437.45	−0.07
$7p_{1/2}$	−56878.19	−60634.41	−60583.72	−60491.17	0.15
$8p_{1/2}$	−30052.91	−31254.62	−31235.75	−31236.21	0.00
$7p_{3/2}$	−52905.73	−55698.48	−55685.67	−55633.65	0.09
$8p_{3/2}$	−28502.19	−29459.90	−29454.30	−29450.48	0.01
$6d_{3/2}$	−62355.89	−70191.99	−70301.27	−69758.23	0.78
$6d_{5/2}$	−61592.49	−68501.09	−68627.88	−68099.51	0.78

B. Matrix Elements

This section will show and compare the calculated values for reduced electric dipole, electric quadrupole, and magnetic dipole matrix elements. For the random phase approximation of E1 matrix elements, we used the time-dependent Hartfree-Fock method whereas we used the diagrammatic RPA for E2 and M1 matrix elements (see Sec. III D). To obtain the final values for the MEs, we add Breit and Structure Radiation and Normalisation contributions to the results of the scaled all-orders method including QED effects. To accurately include the Breit contribution, we fitted to the experimental energies after subtracting the computed Breit contribution towards those energies (see Sec. III J). We show primarily values where comparisons are available. Tables with all calculated E1 matrix elements can be found in Appendix B 1.

E1 - Electric Dipole matrix elements

Table II shows all reduced E1 matrix elements of Ba^+ where experimental values are available. Of the available experiments for all 3 ions, these values feature the smallest uncertainties overall, starting at the fourth significant digit. The performed calculations agree very well with the experiment, with the highest deviations being 0.45% and 0.46% magnitude for the lowest $p_{3/2} \to d$ transitions. Due to the very low experimental standard deviations, most of the calculated final values deviate at least $2\,\sigma$ from the experimental midpoint values. Nonetheless, when compared to other groups' calculations, such as a recent one by Porsev et al. (2021) ([104]), where the 'CCSDvT'[11] method was used, we tend to lie closer to the experiment. The table also presents the individual contributions from QED effects, the Breit interaction, as well as Structure Radiation and Normalisation. Most effects are fairly small and only affect the computed values from the fourth significant digit onwards. Nonetheless, these contributions are crucial in order to ensure high precisions in the calculations.

TABLE II: Calculated reduced E1 matrix elements for Ba^+ where experimental comparisons are available. Different approximations are compared with other calculations and experiments. All values are given in atomic units ($e\,a_B$) and as absolute values.

					Ba^+					
State	RHF	$\Sigma^{(\infty)}$	δBreit	δQED	δSR+N	$\delta\lambda$	Final	Other	Exp.	Δ(%)
$6p_{1/2} - 6s$	3.8909	3.3195	−0.0002	0.0020	−0.0013	0.0032	3.3214(80)	3.299[a]	3.3251(21)[b]	−0.11
								3.36(1)[e]		
$6p_{3/2} - 6s$	5.478	4.687	0.000	0.003	−0.002	0.004	4.689(11)	4.659[a]	4.7071(27)[b]	−0.38
								4.73(3) [e]		
$6p_{1/2} - 5d_{3/2}$	3.745	3.040	−0.004	−0.001	−0.031	0.026	3.033(56)	3.001[a]	3.0413(21)[c]	−0.27
								3.11(3) [e]		
$6p_{3/2} - 5d_{3/2}$	1.635	1.327	−0.002	−0.001	−0.012	0.012	1.326(22)	1.312[a]	1.33199(96)[d]	−0.45
								1.34(2) [e]		
$6p_{3/2} - 5d_{5/2}$	5.001	4.095	−0.008	−0.002	−0.045	0.036	4.084(81)	4.047[a]	4.1028(25)[d]	−0.46

[a]Ref. [104], [b]Ref. [126], [c]Ref. [38], [d]Ref. [128], [e]Ref. [119]

[11] 'Coupled-Cluster Single Double (valence) Triple'.

TABLE III: Calculated reduced E1 matrix elements for Sr^+. Different approximations are compared with other calculations and experiments when available. All values are given in atomic units ($e\,a_B$) and as absolute values.
'†' means that our final values lie within the experimental standard deviation.

	Sr^+									
State	RHF	$\Sigma^{(\infty)}$	δBreit	δQED	δSR+N	$\delta\lambda$	Final	Other	Exp.[c]	Δ(%)
$5p_{1/2}-5s$	3.4848	3.0751	0.0000	0.0011	−0.003	−0.0012	3.0712(31)	3.078[a]	3.076(24)	−0.16†
$6p_{1/2}-5s$	0.0664	0.0518	−0.0008	0.0011	−0.015	−0.0016	0.0358(56)	0.025[a]		
$7p_{1/2}-5s$	0.0050	0.0798	−0.0004	0.0006	−0.010	−0.0004	0.0698(35)	0.063[a]		
$5p_{3/2}-5s$	4.9211	4.3471	0.0000	0.0016	−0.004	−0.0018	4.3414(44)	4.351[a]	4.360(23)	−0.43†
$6p_{3/2}-5s$	0.1606	0.0035	0.0000	0.0014	0.021	−0.0013	0.0232(63)	0.034[a]		
$7p_{3/2}-5s$	0.0278	0.0767	0.0000	0.0007	−0.014	−0.0001	0.0633(48)	0.053[a]		
$5p_{1/2}-6s$	2.375	2.346	0.002	−0.002	−0.021	0.007	2.333(10)			
$6p_{1/2}-6s$	6.8103	6.5426	−0.0002	0.0022	−0.013	−0.0075	6.5226(89)			
$5p_{3/2}-6s$	3.497	3.459	0.001	−0.002	−0.029	0.009	3.440(13)			
$6p_{3/2}-6s$	9.578	9.199	0.001	0.003	−0.018	−0.010	9.171(12)			
$5p_{1/2}-4d_{3/2}$	3.729	3.095	−0.003	−0.001	−0.024	0.018	3.088(19)	3.112(10)[a]	3.093(15)	−0.16†
$6p_{1/2}-4d_{3/2}$	0.026	0.067	0.002	0.000	−0.013	−0.012	0.042(12)	0.07847[b]		
$7p_{1/2}-4d_{3/2}$	0.0469	0.0375	0.0010	0.0001	−0.007	−0.0053	0.0247(59)	0.04487[b]		
$5p_{3/2}-4d_{3/2}$	1.6572	1.3747	−0.0013	−0.0003	−0.010	0.0081	1.3722(87)	1.383(5)[a]	1.378(34)	−0.42†
$6p_{3/2}-4d_{3/2}$	0.0284	0.0457	0.0007	0.0002	−0.006	−0.0052	0.0348(55)	0.05105[b]		
$7p_{3/2}-4d_{3/2}$	0.0280	0.0242	0.0003	0.0001	0.003	−0.0024	0.0250(27)	0.02758[b]		
$5p_{3/2}-4d_{5/2}$	5.003	4.166	−0.006	−0.001	−0.032	0.023	4.155(26)	4.187(14)[a]	4.175(22)	−0.48†
$6p_{3/2}-4d_{5/2}$	0.076	0.128	0.003	0.000	−0.016	−0.015	0.097(16)	0.142[a]		

[a]Ref. [74], [b]Ref. [110], [c]Refs. [36, 102]

Table III shows various valence states of Sr^+ and compares them with other theoretical results as well as experiments. For five matrix elements, experimental values were indeed available, with an uncertainty given at the level of the third significant digit. The given exp. values were determined in Ref. [107] by combining the measurements of branching ratios in Ref. [36] with lifetime measurements presented in Ref. [102]. Our calculations align exceptionally well with the experiment in the case of Sr^+, which deviates at most by a magnitude of 0.48% for the low-lying $p_{3/2} \to d_{5/2}$ transition. Furthermore, it should be noted that all of our calculations lie within the given exp. standard deviations. When comparing our calculations to other groups, it can be seen that their values are usually close to ours, although for some matrix elements discrepancies can be noted. These include, for example, the $6p_{1/2}-5s$ and $6p_{3/2}-4d_{5/2}$ transition in comparison to Ref. [74]. In this case, the values reported by Jiang et al. (2009) differ from our results by approximately $2\,\sigma$. Additionally, the $6p_{1/2}-4d_{3/2}$, $7p_{1/2}-4d_{3/2}$ and $6p_{3/2}-4d_{3/2}$ values are noticeably distinct from those of Safronova et al. (2010) (Ref. [110]), with deviations also being around $4\,\sigma-5\,\sigma$ for those. It is important to mention that Refs. [74] and [110] utilised the relativistic CCSD[12] method, which means that possibly important triple excitations could be missing in these calculations. Future precision experiments will be able to tell which of these calculations are more accurate.

Table IV shows various calculated reduced E1 matrix elements for the Radium ion. We present all transitions where comparisons - mostly to other theoretical values - are available. When experimental data are available, our calculations are within the given exp. standard deviations (SDs) four out of five times, indicating a very high precision for the calculation of E1 MEs in heavy

[12] 'Coupled-Cluster Single Double'

TABLE IV: Calculated reduced E1 matrix elements for Ra^+. Different approximations are compared with other calculations and experiments when available. All values are given in atomic units ($e\,a_B$) and as absolute values.
'†' means that our final values lie within the experimental standard deviation.

					Ra^+					
State	RHF	$\Sigma^{(\infty)}$	δBreit	δQED	δSR+N	$\delta\lambda$	Final	Other	Exp. [64]	Δ(%)
$7p_{1/2}-7s$	3.877	3.230	0.000	0.004	0.000	0.005	3.235(29)	3.28(2)[a]	3.229(9)	0.19†
$8p_{1/2}-7s$	0.125	0.088	−0.002	0.004	−0.027	0.001	0.064(33)	0.08(4)[a]		
$9p_{1/2}-7s$	0.024	0.102	−0.001	0.002	−0.017	−0.012	0.075(13)	0.09(3)[a]		
$7p_{3/2}-7s$	5.340	4.483	0.000	0.007	0.002	0.007	4.494(44)	4.54(2)[a]	4.484(13)	0.22†
$8p_{3/2}-7s$	0.625	0.344	0.000	−0.003	0.034	−0.003	0.374(36)	0.49(2)[a]		
$9p_{3/2}-7s$	0.281	0.110	0.000	−0.002	0.024	−0.010	0.123(12)	0.30(2)[a]		
$7p_{1/2}-8s$	2.637	2.538	0.006	−0.005	−0.034	0.015	2.519(47)	2.517[b]		
$8p_{1/2}-8s$	7.371	6.980	−0.001	0.007	−0.022	−0.002	6.9574(84)	6.949[b]		
$7p_{3/2}-8s$	4.810	4.675	0.001	−0.006	−0.046	0.011	4.640(50)	4.644[b]		
$8p_{3/2}-8s$	9.881	9.342	0.001	0.012	−0.027	−0.002	9.315(11)	9.294[b]		
$7p_{1/2}-6d_{3/2}$	4.446	3.540	−0.006	−0.003	−0.024	0.021	3.533(32)	3.62(5)[a]	3.564(27)	−0.87
$8p_{1/2}-6d_{3/2}$	0.105	0.020	0.005	0.002	−0.028	−0.013	0.021(16)	0.06(2)[a]		
$9p_{1/2}-6d_{3/2}$	0.087	0.005	−0.002	0.000	−0.016	0.007	0.0105(83)	0.02(1)[a]		
$7p_{3/2}-6d_{3/2}$	1.881	1.499	−0.002	−0.002	−0.007	0.010	1.502(16)	1.54(2)[a]	1.513(11)	−0.73†
$8p_{3/2}-6d_{3/2}$	0.168	0.131	0.001	0.001	0.013	−0.005	0.1388(61)	0.15(2)[a]		
$9p_{3/2}-6d_{3/2}$	0.094	0.063	0.000	0.000	0.009	−0.005	0.0673(54)	0.07(2)[a]		
$7p_{3/2}-6d_{5/2}$	5.862	4.802	−0.011	−0.004	−0.042	0.030	4.785(55)	4.84(8)[a]	4.788(14)	−0.06†
$8p_{3/2}-6d_{5/2}$	0.462	0.361	0.004	0.002	0.021	−0.015	0.366(17)	0.378[b]		

[a]Ref. [118], [b]Ref. [48]

ions. The highest deviation is of 0.87% in magnitude whilst the lowest is 0.06%. For the sake of completeness, we want to mention that some of the experimental values were extracted from experiments using theoretical ratios between matrix elements. This has been done and explained in a previous paper by Roberts et al. (2022) ([107]). When comparing the AMPSCI data to other calculations, most values agree very well. There are, although, as in the previous example for Sr^+, some noticeable differences. These are for the $8p_{3/2}-6d_{3/2}$ and $8p_{1/2}-6d_{3/2}$ transitions in Ra^+ compared to Ref. [118] by Sahoo et al. (2008). Their values are at least $3\,\sigma$ off when using our estimated SDs, showing a significant difference. Ref. [118] employed the relativistic CCSD(T) method, where the most important triple excitations have been included. As in the case of Sr^+, future experiments will likely be able to tell which method is more precise. However, we expect our calculations to be more accurate, since we include higher-order effects while usually having better agreement with experimental data when available.

M1 and E2 - Magnetic Dipole and Electric Quadrupole matrix elements

This section will show the computed reduced E2 and M1 matrix elements for the lowest lying s, p, and d valence states, which are also important for utilisation in optical atomic clocks. Only a limited amount of data from other calculations were available for comparison, and we identified two experimental values for E2 MEs. For each ion, at least four theoretical comparisons were found for a total of twenty calculated transitions. It can be seen in Table V that our calculations for E2 MEs are all close to existing calculations. Furthermore, for the experimental comparison of the

TABLE V: Calculated reduced M1 and E2 matrix elements for Sr^+, Ba^+, and Ra^+. For each ME, RHF and Final values are compared. All values are given in atomic units and as absolute values. The '†' after some non-relativistically forbidden M1 MEs implies that numerical instabilities were noted. In this case, we present the values at the level of third-order MBPT.

Sr^+

	M1 ($\|\mu_B\|$)			E2 (ea_B^2)		
State	RHF	Final	Other[a]	RHF	Final	Other
$6s-5s$	$4.80\cdot10^{-5}$	$2.58\cdot10^{-5\dagger}$	$2.828\cdot10^{-5}$			
$4d_{3/2}-5s$	$1.55\cdot10^{-6}$	$4.65(76)\cdot10^{-5}$	$4.693\cdot10^{-5}$	12.97	11.103(64)	11.21(5)[b]
						11.13(39)[a]
$4d_{5/2}-5s$				15.97	13.709(77)	13.74[a]
$4d_{3/2}-6s$	$4.45\cdot10^{-6}$	$2.50(38)\cdot10^{-5}$		7.97	5.96(14)	
$4d_{5/2}-6s$				9.89	7.45(17)	
$6p_{1/2}-5p_{1/2}$	$1.68\cdot10^{-5}$	$2.10\cdot10^{-5\dagger}$				
$5p_{3/2}-5p_{1/2}$	1.154327	1.1542580(91)		25.409	23.380(26)	
$6p_{3/2}-5p_{1/2}$	0.01592113	0.0166(16)		15.268	14.231(47)	
$5p_{3/2}-6p_{1/2}$	0.01642035	0.0183(15)		16.576	15.554(43)	
$6p_{3/2}-6p_{1/2}$	1.154292	1.154232(12)		98.356	93.221(70)	
$6p_{3/2}-5p_{3/2}$	$6.82\cdot10^{-5}$	$7.32\cdot10^{-5\dagger}$		16.077	15.054(44)	
$4d_{5/2}-4d_{3/2}$	1.5490980	1.549152(28)		7.260	5.958(55)	

Ba^+

	M1 ($\|\mu_B\|$)			E2 (ea_B^2)		
State	RHF	Final	Other	RHF	Final	Other
$7s-6s$	$4.95\cdot10^{-5}$	$7.21\cdot10^{-5\dagger}$	$7.257\cdot10^{-5}$[a]			
$5d_{3/2}-6s$	$0.55\cdot10^{-5}$	$16.5(3.1)\cdot10^{-5}$	$16.94\cdot10^{-5}$[a]	14.76	12.56(11)	12.76(35)[d]
						12.63(11)[c]
$5d_{5/2}-6s$				18.38	15.71(14)	15.80(12)[c]
$5d_{3/2}-7s$	$0.59\cdot10^{-5}$	$8.4(1.6)\cdot10^{-5}$		6.20	4.66(18)	4.74(9)[c]
$5d_{5/2}-7s$				7.94	6.06(22)	6.17(11)[c]
$7p_{1/2}-6p_{1/2}$	$1.82\cdot10^{-5}$	$2.31\cdot10^{-5\dagger}$				
$6p_{3/2}-6p_{1/2}$	1.152753	1.152321(51)		31.319	28.272(70)	
$7p_{3/2}-6p_{1/2}$	0.0364	0.0393(23)		17.06	15.58(10)	
$6p_{3/2}-7p_{1/2}$	0.0389	0.0436(22)		20.70	19.28(87)	
$7p_{3/2}-7p_{1/2}$	1.152525	1.152118(42)		114.21	106.88(15)	
$7p_{3/2}-6p_{3/2}$	$6.83\cdot10^{-5}$	$7.18\cdot10^{-5\dagger}$		19.275	17.845(87)	
$5d_{5/2}-5d_{3/2}$	1.54889	1.54928(12)	1.549[c]	8.091	6.666(82)	

Ra^+

	M1 ($\|\mu_B\|$)			E2 (ea_B^2)		
State	RHF	Final	Other[a]	RHF	Final	Other[a]
$8s-7s$	$0.061\cdot10^{-3}$	$1.076\cdot10^{-3\dagger}$	$1.10\cdot10^{-3}$			
$6d_{3/2}-7s$	$0.006\cdot10^{-3}$	$1.33(31)\cdot10^{-3}$	$1.386\cdot10^{-3}$	17.263	14.662(95)	14.74(12)
$6d_{5/2}-7s$				21.77	18.76(13)	18.86
$6d_{3/2}-8s$	$0.007\cdot10^{-3}$	$0.57(15)\cdot10^{-3}$		10.00	7.57(18)	
$6d_{5/2}-8s$				13.19	10.46(23)	
$8p_{1/2}-7p_{1/2}$	$0.022\cdot10^{-3}$	$0.029\cdot10^{-3\dagger}$				
$7p_{3/2}-7p_{1/2}$	1.137744	1.13398(41)		33.27	29.80(10)	
$8p_{3/2}-7p_{1/2}$	0.1002	0.1140(70)		14.45	12.81(15)	
$7p_{3/2}-8p_{1/2}$	0.122	0.126(13)		25.88	24.33(11)	
$8p_{3/2}-8p_{1/2}$	1.135735	1.13293(79)		119.10	110.84(18)	
$8p_{3/2}-7p_{3/2}$	$0.073\cdot10^{-3}$	$0.055\cdot10^{-3\dagger}$		21.26	19.70(11)	
$6d_{5/2}-6d_{3/2}$	1.5478	1.5511(11)		10.367	8.556(84)	

[a]Ref. [115], [b]Ref. [89] (Exp. value extracted via lifetime measurement), [c]Ref. [112], [d]Ref. [127] (Exp. value extracted via lifetime measurement)

$5d_{5/2} - 6s$ E2 transition in Ba^+, our calculation lies well within the exp. SD with $0.11\,\sigma$ and a deviation of 0.56%. For the second exp. value, the $4d_{3/2} - 5s$ E2 transition in Sr^+, we notice a difference of approximately $2\,\sigma$. Both values were extracted from exp. lifetime measurements. It can be seen that our values align very well with the theoretical values obtained in Refs. [115] and [112] by Safronova et al.
For the reduced M1 matrix elements, our values for all three ions are close to existing theoretical values by the same group. The values of Ref. [115] lie within our SDs for all of the three ions. It should be mentioned that we noticed numerical instabilities when computing non-relativistically forbidden M1 matrix elements. These feature states with equal angular quantum numbers ($l = l'$) but unequal principal quantum numbers ($n \neq n'$). Some instabilities can arise because their true value is very small. In the relativistic limit, the value is indeed 0 since those wavefunctions are in that case fully orthogonal. When including relativistic effects (as in our case), a small additional term, which is suppressed by α^{-2}, comes into play. This should also be the only non-zero and hence dominating term in the calculations. However, due to the way we calculate our wavefunctions, they are never completely orthogonal. Even though we generally achieve high orthogonalities of $\leq 10^{-3}$ between core and valence states, these terms can become overly dominant in comparison to the α^{-2} suppressed integral term. Accordingly, even very small truncation errors in the orthogonality of these states can let the calculated value of certain non-relativistically forbidden M1 MEs blow up [115]. Therefore, when we noticed these instabilities for certain transitions, we used the so-called third-order method instead. This method is in theory less accurate than the all-orders method, but is generally more stable since it is entirely based on a basis expansion ([79]), for which the orthogonality can be guaranteed to a higher level of accuracy. For all final values that are marked with a '†' in Table V, we have used this approach. For the lowest-lying $s \to s$ state M1 transitions in both ions, it can be seen that our calculations are fairly close to those of Ref. [115], which used the same calculation method. This points towards a fairly accurate first-principles calculation.

However, for the relevant clock transitions of all ions, these numerical instabilities were not encountered. This makes sense since $d_{3/2} \to s$ state transitions have different angular quantum numbers. Hence, we could use the most accurate calculation method available to us and should not expect negative influences for a characterisation regarding its usage in an atomic clock.

C. Lifetimes

Lifetimes can provide a decent indirect proof for the accuracy of matrix element calculations, since they directly influence the lifetimes. Additionally, lifetime measurements are usually easier to perform, which means that generally more experimental comparisons are available, as is the case for all three investigated ions. Estimates for electric dipole matrix elements are more readily obtained, since they dominate in allowed transitions. In contrast, higher-order matrix elements are more challenging to measure, as they are only accessible through forbidden transitions, which are more difficult to access by state-of-the-art experimental probes.
We computed lifetimes up to the most accurate order of the calculated matrix elements. The column 'Final' corresponds to the scaled all-orders method and includes Breit, QED, and Structure Radiation and Normalisation contributions. For the transition frequencies in the lifetime formula we used the data available from experiments, which were obtained from the NIST database ([98]). We show two tables, one where lifetimes with allowed transitions are calculated and one with lifetimes featuring only non-allowed transitions. The latter are most relevant for the use in atomic clocks (see Sec. II A).

For the lowest p states of the three ions, all of which feature allowed transitions, experimental values for the lifetimes are available, as shown in Table VI. Out of those five states, our calculations are within 1 standard deviation of the experiment for all states, showing exceptional agreement. All of our values are very accurate, most within $0.5\,\sigma$. Overall, the high level of accuracy indicates excellent precision in the calculation of E1 matrix elements since they determine the accuracy of lifetime calculations for allowed transitions. This is consistent with our findings in the previous section, where E1 MEs were shown to be accurate within the 0.1% range when compared to the existing literature. Furthermore, our results generally agree more closely with experimental values than other theoretical predictions.

TABLE VI: Calculated lifetimes for the lowest lying valence states in Sr^+, Ba^+, and Ra^+ with allowed transitions. Different approximations are compared with other calculations and experiments. Values are given in ns. '†' means that the calculated value is within the experimentalstandard deviation.

			Sr^+		
State	$\Sigma^{(2)}$	$\Sigma^{(\infty)}$	Final	Exp.	Other
$5p_{1/2}$	7.55	7.39	7.416(70)†	7.47(7)[1]	7.376[2]
				7.39(7)[3]	
$5p_{3/2}$	6.81	6.67	6.688(63)†	6.69(7)[1]	6.653[2]
				6.63(7)[3]	
$6s$	4.35	4.37	4.417(42)		

			Ba^+		
State	$\Sigma^{(2)}$	$\Sigma^{(\infty)}$	Final	Exp.	Other
$6p_{1/2}$	8.129	7.876	7.879(50)†	7.90(10)[3]	7.68(7)[4]
				7.92(8)[2]	7.83[5]
$6p_{3/2}$	6.44	6.31	6.37(15)†	6.32(10)[3]	6.26(11)[4]
					6.27[5]
$7s$	5.025	5.030	5.114(49)		

			Ra^+		
State	$\Sigma^{(2)}$	$\Sigma^{(\infty)}$	Final	Other [120]	Exp. [64]
$7p_{1/2}$	9.20	8.85	8.83(13)	8.57(10)	
$7p_{3/2}$	4.977	4.782	4.766(72)†	4.67(9)	4.78(3)
$8s$	5.48	5.48	5.56(15)		

[1]Ref. [82], [2]Ref. [74], [3]Ref. [102], [4]Ref. [118], [5]Ref. [72]

Table VII presents the calculated lifetimes for the relevant clock transitions of all ions, corresponding to the lowest-lying d states. Additional details on the states considered for each ion can be found in Sec. II A. Experimental data is available for five of the six relevant states, and our calculations agree within $0.5\,\sigma$ for four of them.

For the $4d_{3/2}$ state in Sr^+, we agree with the experimental value of 0.455(29) ns by Ref. [34] by Biémont et al. (2000) within their given standard deviation. This experiment was conducted using laser probing. On the other hand, we disagree with the value of 0.435(4) ns using an optical pump measurement method, which was performed by Ref. [34] in the same publication and in Ref. [89] by Mannervik et al. (1999). For these, our computed midpoint value is off by about 2 experimental SDs. Furthermore, the theoretical values of other groups by Jiang et al. (2009) ([74]) and Safronova et al. (2017) ([115]) also show some variation.

For Ba^+, both relevant valence state lifetimes lie well within the experimental standard deviations. However, it should be mentioned that the corresponding experiments feature larger SDs than for the other two ions.

For Ra^+ the only experimental value available regards the $6d_{5/2}$ state. However, the given experimental value of 0.232 s by Versolato et al. (2010) ([45]) is noticeably different from ours of 0.309 s and from another theory value of 0.303 s ([114]). Versolato et al. note that their measured value may be considered as a lower bound for the lifetime of this state (see [45], p.18). They explain this by referring to the buffer gas causing the metastable state to quench to the ground state and thus reducing the lifetime during their measurements [45]. Therefore, this value should probably be treated with caution.

Overall, the good agreement of the lifetimes of states with non-allowed transitions proves us confident, especially in the calculated E2 but also in the non-relativistically allowed M1 matrix elements.

TABLE VII: Calculated lifetimes for the two relevant clock states − the lowest lying d states in Sr^+, Ba^+, and Ra^+. Different approximations are compared with other calculations and experiments. Values are given in s. '†' means that the calculated value is within the experimental standard deviation.

			Sr^+		
State	$\Sigma^{(2)}$	$\Sigma^{(\infty)}$	Final	Exp.	Other
$4d_{3/2}$	0.455	0.439	0.4442(43)†	0.455(29)[1]	0.441(3)[3]
				0.435(4)[1,2]	0.437(14)[4]
$4d_{5/2}$	0.406	0.392	0.3974(37)†	0.408(22)[1]	0.394(3)[3]
				0.372(25)[5]	0.3945(22)[4]

			Ba^+		
State	$\Sigma^{(2)}$	$\Sigma^{(\infty)}$	Final	Exp.	Other
$5d_{3/2}$	85.1	81.8	82.4(1.4)†	79.8(4.6)[6]	81.4(1.4)[4]
				89.(16.)[7]	80.1(7)[9]
$5d_{5/2}$	31.28	30.33	30.61(43)†	31.2(0.9)[8]	30.34(48)[4]
				32.0(4.6)[7]	29.9(3)[9]

			Ra^+		
State	$\Sigma^{(2)}$	$\Sigma^{(\infty)}$	Final	Other [114]	Exp. [45]
$6d_{3/2}$	0.6729	0.6414	0.6447(77)	0.6382(94)	
$6d_{5/2}$	0.3174	0.3051	0.3093(37)	0.3028(37)	0.232(4)

[1]Ref. [34], [2]Ref. [89], [3]Ref. [74], [4]Ref. [115], [5]Ref. [86], [6]Ref. [127], [7]Ref. [37], [8]Ref. [3], [9]Ref. [116]

D. Branching ratios

Additionally, we calculated the branching ratios of the rates used for the calculation of the lifetimes. Table VIII shows those ratios for the relevant clock states. It can be seen that electric quadrupole transition rates are dominant for all states. Especially for the rates from $d_{3/2}$ states they essentially contribute to the whole rate, with contributions of about 0.999997 for Ra^+, 0.999998 for Ba^+, and 0.999999 for Sr^+. The rest comes from the contribution of the one available M1 transition. However, for the $d_{5/2}$ transitions, the non-relativistically allowed $nd_{5/2} - nd_{3/2}$ M1 transition rates can contribute significantly. For example, for Ra^+, they contribute approximately 0.38%, whereas

TABLE VIII: Branching ratios within relevant clock states of Sr^+, Ba^+, and Ra^+. It can be seen that especially E2 as well as non-relativistically allowed M1 transitions are the dominant contributions for the transition rates between those states.

		Sr^+	
$4d_{5/2}$	$4d_{5/2} - 5s$ (E2)	$4d_{5/2} - 4d_{3/2}$ (E2)	$4d_{5/2} - 4d_{3/2}$ (M1)
	0.999999	$6.80425 \cdot 10^{-7}$	0.0000264
$4d_{3/2}$	$4d_{3/2} - 5s$ (E2)	$4d_{3/2} - 5s$ (M1)	
	0.999999	$6.80425 \cdot 10^{-7}$	
		Ba^+	
$5d_{5/2}$	$5d_{5/2} - 6s$ (E2)	$5d_{5/2} - 5d_{3/2}$ (E2)	$5d_{5/2} - 5d_{3/2}$ (M1)
	0.830278	$8.36871 \cdot 10^{-6}$	0.169714
$5d_{3/2}$	$5d_{3/2} - 6s$ (E2)	$5d_{3/2} - 6s$ (M1)	
	0.999998	$1.74845 \cdot 10^{-6}$	
		Ra^+	
$6d_{5/2}$	$6d_{5/2} - 7s$ (E2)	$6d_{5/2} - 6d_{3/2}$ (E2)	$6d_{5/2} - 6d_{3/2}$ (M1)
	0.996177	$5.30716 \cdot 10^{-6}$	0.003817
$6d_{3/2}$	$6d_{3/2} - 7s$ (E2)	$6d_{3/2} - 7s$ (M1)	
	0.999997	$3.37423 \cdot 10^{-6}$	

for Ba^+ the contribution is around 16.97%. The remaining part again falls mainly to the E2 transition to the s valence ground states, while the $nd_{5/2} - nd_{3/2}$ E2 transitions only contribute at the order of 10^{-6}. Therefore, we conclude that the accuracy of the corresponding lifetimes point to a high accuracy of the corresponding E2 and non-relativistically allowed M1 matrix elements.

E. Static Polarisabilities

This section presents the results for the static scalar and tensor polarisabilities of various Sr^+, Ba^+, and Ra^+ valence states. For the individual contributions, we estimated the Breit, QED and SR+N contributions using scaled correlation potentials. This is necessary since the energies are very important for the calculation of polarisabilities because of their appearance in the denominator. For more details, please refer to Sec. II D.

Tables IX, X, and XI show the calculated static scalar polarisabilities. We found only one experimental value to compare to, obtained for the static polarisability of the Ba^+ valence ground state. Higher excited states are particularly challenging to measure due to their quicker decay, which limits experimental accessibility. Compared with the theoretical values of other groups, we are mostly within $1\,\sigma - 2\,\sigma$ of their estimated uncertainties (when given).

For example, for Sr^+ (see Table IX) where many theoretical comparisons were found, it can be seen that some values, e.g., for the $5p_{1/2}$ and $6p$ states, show tensions between calculations. Especially for the $5p_{1/2}$ states the variability is very high. We align much closer with the value of Safronova (2010) ([113]) than with Mitroy et al. (2008) ([90]). A noticeable difference is that Safronova utilised the CCSD[13] method, whereas Mitroy et al. used a semi-empirical Hamiltonian approach. This approach can sometimes deviate from the best calculations ([90]), as stated by the

[13] Coupled-Cluster Single Double

authors themselves. Therefore, a higher accuracy for the CCSD value should probably be assumed. Higher tensions between our values and those of Safronova can be seen in the two $6p$ states in Sr^+. For the single experimental value we identified – the $6s$ state in Ba^+ (see Tbl. X) – measured by Snow et al. (2007) ([121]), our calculations are slightly closer to their exp. midpoint compared to Sahoo et al. (2008) ([118]). However, they still fall outside the narrow experimental standard deviation. Furthermore, in the case of Ra^+ (Tbl. XI), there seems to be disagreement, especially for the scalar polarisability of the $6d_{3/2}$ state. Sahoo et al. (2009) ([119]) use a RCCSD(T)[14] approach while Wu et al. (2016) ([62]) use a *relativistic core polarisation potential method*.

TABLE IX: Calculated static scalar polarisabilities of various Sr^+ valence states in a.u. ($a_B{}^3$).

		Sr^+		
State	RHF	δBreit	Final	Other
$5s$	127.03	−0.006	90.91(33)	91.3(9)[c]
				88.3(1.0)[a]
$6s$	1247.7	−0.22	1065.2(8.5)	1082.(4.)[e]
				1089.[d]
$5p_{1/2}$	−168.9	0.088	−32.7(3.9)	−32.2(9)[e]
				−23.13[d]
$6p_{1/2}$	−2977.5	−0.82	−2241.(84.)	−1990.(5.)[e]
$5p_{3/2}$	−139.9	0.089	−22.0(3.6)	−21.4(8)[e]
				−23.13[d]
$6p_{3/2}$	−2613.4	0.52	−1964.(75.)	−1745.(5.)[e]
$4d_{3/2}$	148.9	−0.028	62.1(2.4)	63.3(9)[e]
				61.43(52)[a]
$4d_{5/2}$	139.4	−0.040	60.8(2.2)	62.0(9)[e]
				62.0(5)[c]
				62.87(75)[a]

[a]Ref. [119], [c]Ref. [74], [d]Ref. [90], [e]Ref. [113]

TABLE X: Calculated static scalar polarisabilities of various Ba^+ valence states in a.u. ($a_B{}^3$).

		Ba^+		
State	RHF	Final	Other	Exp. [121]
$6s$	185.50	123.26(45)	124.5(1.3)[f]	123.88(5)
$6p_{1/2}$	−30.1	19.5(2.5)	17.4(2.9)[f]	
			21.04[g]	
$6p_{3/2}$	4.3	44.0(2.5)	45.9(3.8)[f]	
			46.03[g]	
$5d_{3/2}$	91.3	49.5(1.7)	49.4(1.5)[f]	
			55.69[g]	
$5d_{5/2}$	88.8	49.6(1.7)	50.5(1.4)[f]	
			55.83[g]	

[f]Ref. [118], [g]Ref. [112]

In the literature, no experimental measurements for static tensor polarisabilities (see Table XII) were identified. Theoretical values are provided by the same groups as for the scalar polarisabilities.

[14] Relativistic CCSD including the most important triple excitations

TABLE XI: Calculated static scalar polarisabilities of various Ra^+ valence states in a.u. ($a_B{}^3$).

	Ra^+			
State	RHF	δQED	Final	Other
$7s_{1/2}$	163.81	0.09	105.02(61)	104.5(1.5)[a]
				103.213[b]
$8s_{1/2}$	1329.3	0.37	1080.2(6.8)	
$7p_{1/2}$	−210.7	0.03	−43.7(3.9)	
$8p_{1/2}$	−4911.7	3.12	−4107.(185.)	
$7p_{3/2}$	−24.1	0.00	50.2(3.2)	
$8p_{3/2}$	−1902.	0.05	−1514.(79.)	
$6d_{3/2}$	200.0	2.41	89.7(2.8)	83.71(77)[a]
				88.614[b]
$6d_{5/2}$	153.76	2.76	82.6(2.3)	82.38(70)[a]
				82.176[b]

[a]Ref. [119], [b]Ref. [62]

TABLE XII: Calculated static tensor polarisabilities of various ionic valence states in a.u. ($a_B{}^3$).

			Sr^+		
State	RHF	δBreit	δQED	Final	Other
$5p_{3/2}$	31.55	−0.02	0.01	10.96(27)	10.74(23)[f]
					10.58[a]
$6p_{3/2}$	454.10	−0.03	0.21	365.2(8.4)	326.9(3.5)[f]
					363.5[a]
$4d_{3/2}$	−93.82	0.02	0.00	−34.8(1.7)	−35.5(6)[f]
					−35.42(25)[d]
$4d_{5/2}$	−118.31	0.04	0.00	−46.7(2.1)	−47.7(8)[f]
					−47.7(3)[b]

			Ba^+		
State	RHF	δBreit	δQED	Final	Other
$6p_{3/2}$	23.44	−0.20	0.03	5.18(35)	5.87(13)[c]
$7p_{3/2}$	367.24	−7.90	0.52	305.3(7.9)	363.5[a]
$5d_{3/2}$	−45.50	−0.03	−0.01	−21.5(1.1)	−22.69(54)[c]
$5d_{5/2}$	−58.63	−0.05	−0.02	−28.7(1.4)	−29.42(39)[c]

			Ra^+		
State	RHF	δBreit	δQED	Final	Other
$7p_{3/2}$	−1.97	−0.03	0.07	−17.79(52)	
$8p_{3/2}$	179	0.43	0.99	141.(14.)	
$6d_{3/2}$	−128.7	0.08	−0.46	−48.7(2.0)	−50.23(43)[d]
					−49.1[e]
$6d_{5/2}$	−108	0.10	−0.76	−51.1(1.9)	−52.60(45)[d]
					−53.0[e]

[a]Ref. [90], [b]Ref. [74], [c]Ref. [118], [d]Ref. [119], [e]Ref. [62], [f]Ref. [113]

In cases where they provide uncertainty estimates, our computed values mostly deviate by at least $1\,\sigma$ from theirs. In addition, the values reported by different groups show significant disagreement. These observations highlight notable tensions among theoretical predictions for this quantity.

F. Dynamic Polarisabilities

We calculated dynamic polarisabilities as well as magic wavelengths for the relevant clock transitions. These calculations were evaluated at the level of the scaled all-orders method. Frequency-dependent RPA was not included. However, this should lead only to a negligible deviation because the main contribution of the field frequency is due to its explicit appearance in the denominator of the dynamic polarisability formula (see Eq. 12). Especially around the magic wavelengths it accounts for nearly all of its contribution. For the non-spherically symmetric d states, we also include tensor polarisability contributions. All calculations used an equally spaced grid of 100.000 points in the wavelength range between 100 nm and 2500 nm. Smaller wavelengths were not considered because they are not of physical importance since they reach the values for ionisation energies of the valence electrons. The relevant magic wavelengths are denoted by a red circle in the subsequent plots and are summarised at the end of this section.

Figure 11 shows a plot of the dynamic polarisability of the $7s - 6d_{5/2}$ transition in Ra^+ over the wavelength of an external electric field. This is the transition that was used in the first Ra^+ atomic clock. Resonances that arise at certain wavelengths due to the denominator going to zero are

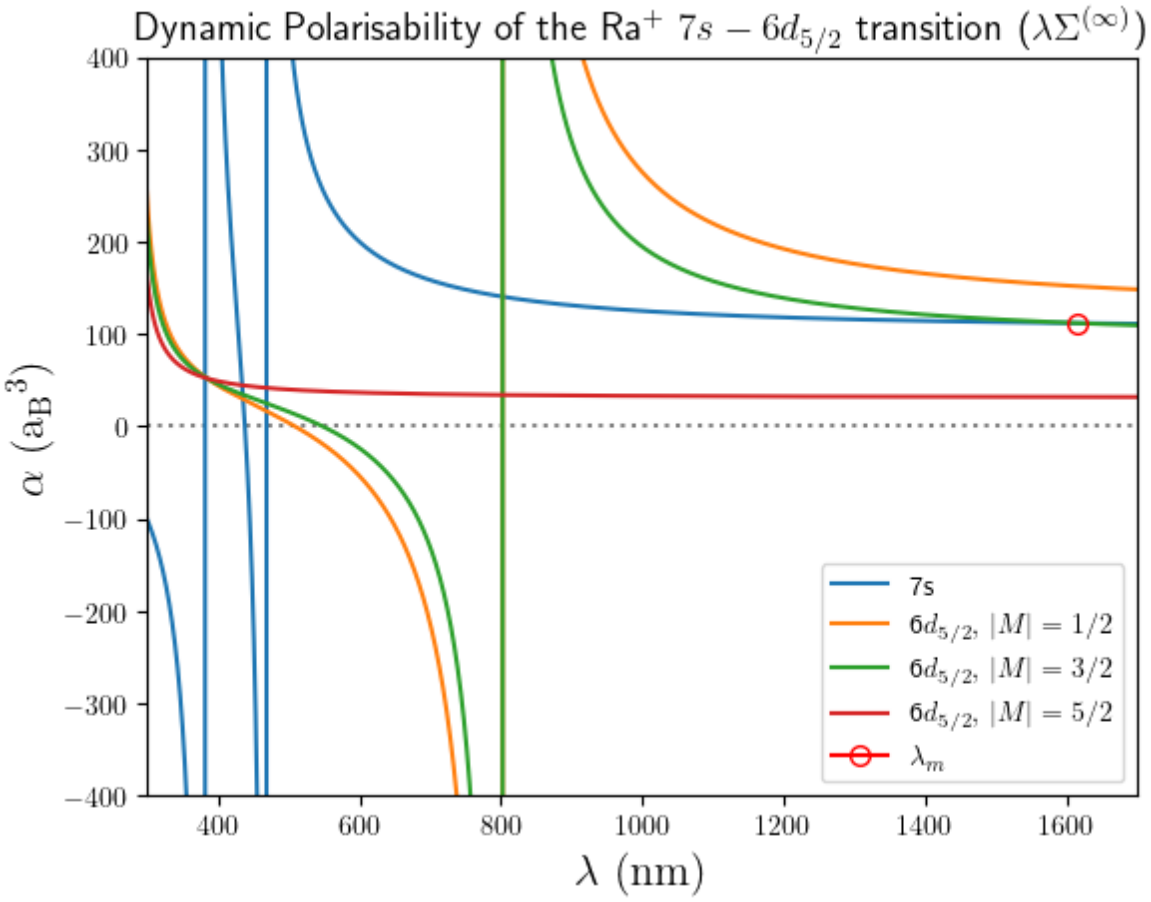

FIG. 11: Plot of the dynamic polarisability of the $7s - 6d_{5/2}$ transition in Ra^+ over the wavelength using the scaled all-orders potential method. Suitable magic wavelengths λ_m are indicated by a red circle.

visible. This leads to magic wavelengths, where the polarisabilities of the two states in the transition become equal. Since the tensor polarisability is dependent on the magnetic projection M, the three possible substates of $6d_{5/2}$ are shown individually. A plot of the second clock transition that is considered for Ra^+, $7s - 6d_{3/2}$, is shown in Fig. 12. Currently, the $7s - 6d_{5/2}$ transition seems to be favoured, since it is believed to be less prone to external perturbations such as the linear Quadrupole Stark Shift [46]. Versolato et al. estimate the frequency uncertainties $\delta\nu/\nu$ at room temperature to be $1.5 \cdot 10^{-14}$ and $5.4 \cdot 10^{-14}$, respectively [46].

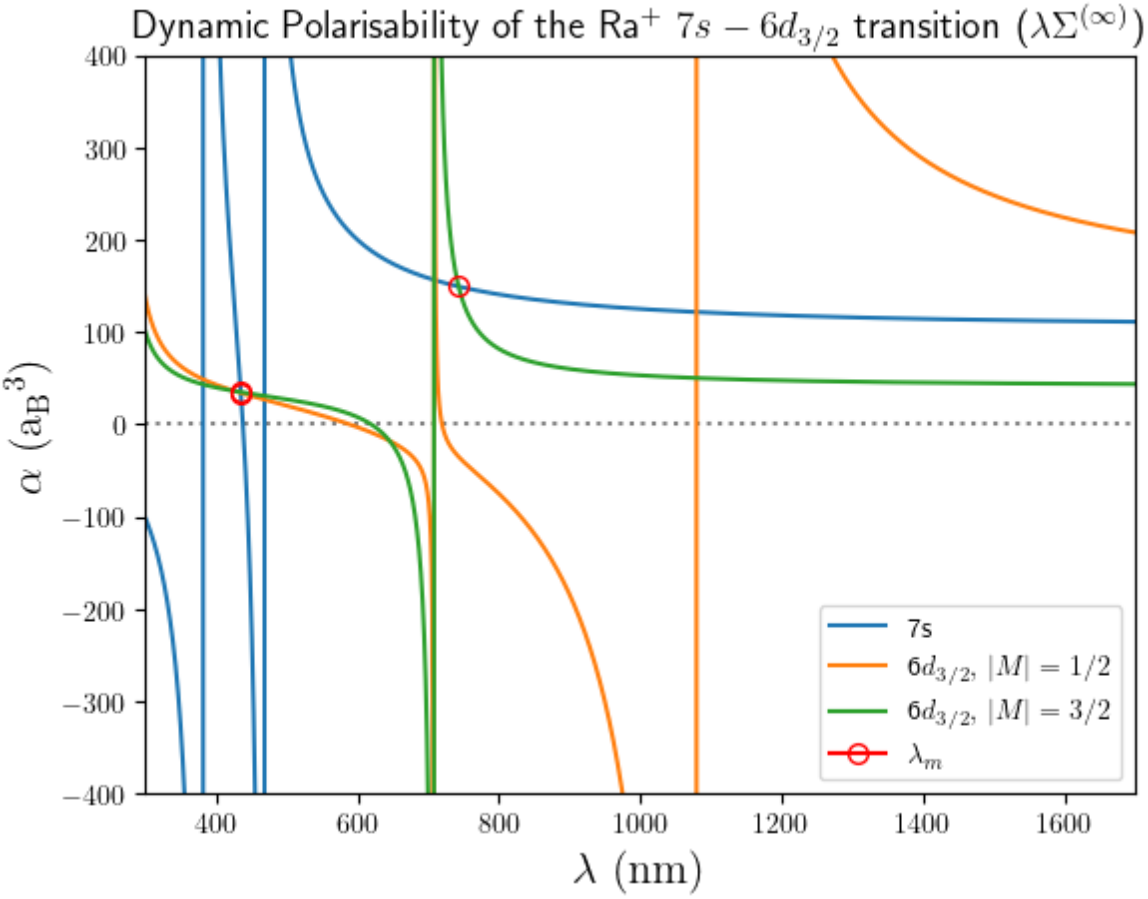

FIG. 12: Plot of the dynamic polarisability of the $7s - 6d_{3/2}$ transition in Ra^+ over the wavelength using the scaled all-orders potential method. Suitable magic wavelengths λ_m are indicated by a red circle.

The corresponding plots for the relevant clock transitions in Sr^+ are shown in Figs. 13 and 14 on page 38 and in Appendix B 2 for Ba^+.

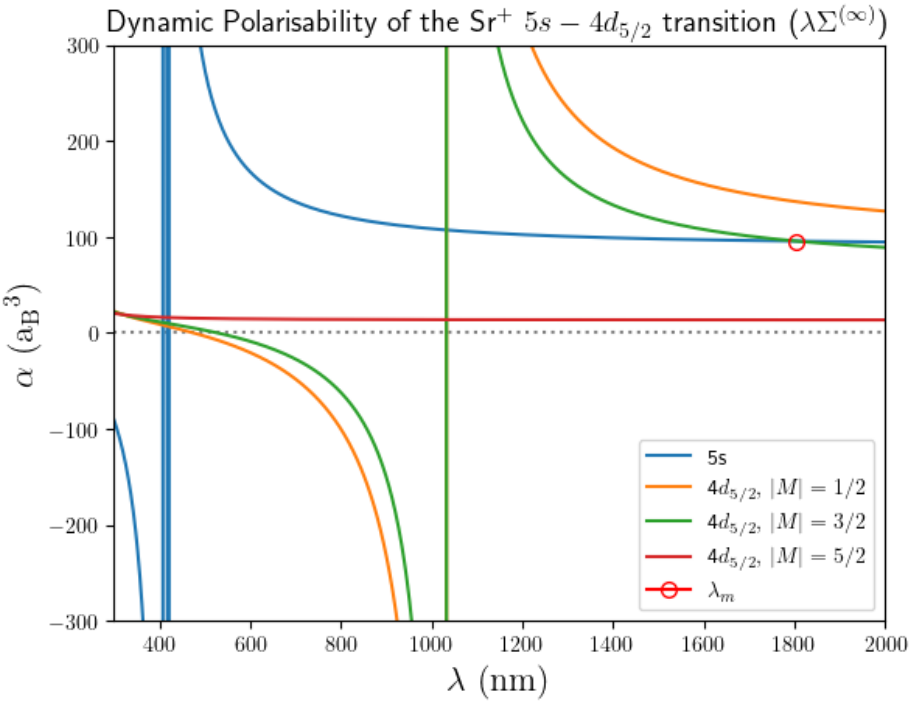

FIG. 13: Plot of the dynamic polarisability of the $5s - 4d_{5/2}$ transition in Sr^+ over the wavelength using the scaled all-orders potential method. Suitable magic wavelengths λ_m are indicated by a red circle.

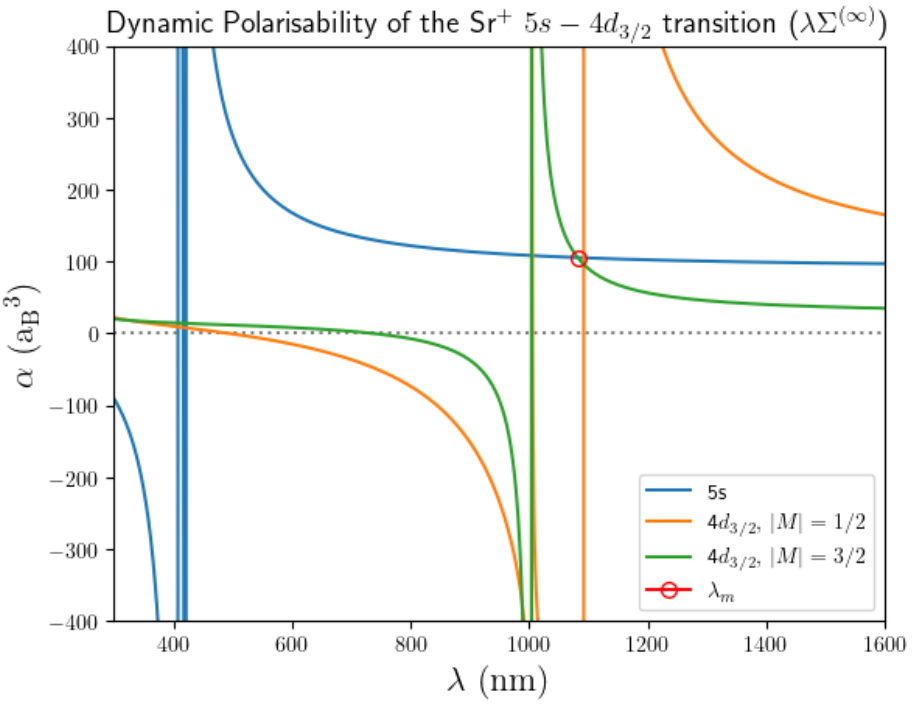

FIG. 14: Plot of the dynamic polarisability of the $5s - 4d_{3/2}$ transition in Sr^+ over the wavelength using the scaled all-orders potential method. Suitable magic wavelengths λ_m are indicated by a red circle.

Magic Wavelengths

Relevant magic wavelengths for the clock transitions of all considered ions along with the corresponding frequencies as well as the value of the polarisability at each magic wavelength are shown in Tables XIII, XIV, and XV. These wavelengths were extracted using a custom PYTHON script, which processed previously computed dynamical polarisability files. The script identified all local minima of the absolute difference between the polarisabilities of two selected states. Most magic wavelengths returned by the script corresponded to energies higher than the ionisation energies and were therefore discarded beforehand. We chose to show the ones for which both states have a low gradient around the respective magic wavelength. This is to avoid magic wavelengths that are close to resonances since they exhibit high spontaneous photon scattering rates, which can result in severe heating processes [70]. These would be unsuitable for use in an atomic clock. The chosen wavelengths are indicated in the corresponding plots (Figs. 11, 12, 13, 14, 15, 16) via red circles.

TABLE XIII: Relevant magic wavelengths of two Sr^+ clock transitions, $5s - 4d_{5/2}$ and $5s - 4d_{3/2}$. Projection numbers M are distinguished.

Sr^+				
Transition	$\|M\|$	λ_m(nm)	Other	$\alpha_0(\lambda_m)$
$5s - 4d_{5/2}$	3/2	1805.07(3.15)	1896.(182.)[a]	95.71
			1880.(103.)[b]	
$5s - 4d_{3/2}$	3/2	1081.67(12)		105.61

[a]Ref. [84], [b]Ref. [75]

TABLE XIV: Relevant magic wavelengths of two Ba^+ clock transitions, $6s - 5d_{5/2}$ and $6s - 5d_{3/2}$. Projection numbers M are distinguished.

Ba^+				
Transition	$\|M\|$	λ_m(nm)	Other	$\alpha_0(\lambda_m)$
$6s - 5d_{5/2}$	1/2	709.36(98)	715.6(13.8)[a]	212.92
			707.9(3.3)[b]	
$6s - 5d_{5/2}$	3/2	664.51(40)	666.7(6.6)[a]	238.14
			663.6(1.4)[b]	
$6s - 5d_{3/2}$	1/2	761.4(1.0)		193.80

[a]Ref. [84], [b]Ref. [76]

When comparisons to other theoretical values are available, such as for the $d_{5/2} \to s$ transitions in Sr^+ and Ba^+ (see Tbls. XIII and XIV), our calculations show good agreement with the literature. In these cases, our results are within $1\,\sigma$ of the values reported by other groups. Notably, the estimated uncertainties of these groups are significantly larger − by an order of magnitude − for Ba^+ compared to those for Sr^+.

For Ra^+, Ref. [62] provides a comparison for both $d \to s$ transitions. Interestingly, the standard deviations stated in their work are much lower than for the previously mentioned references. Especially for the $7s - 6d_{5/2}$ transitions, our calculated value and the one by Wu et al. (2016) disagree by more than 200 nm. For the three given magic wavelengths of the $7s - 6d_{3/2}$ transition, the agreement between our calculations is much better although we are still multiple standard deviations of theirs apart. In theory, our calculations should provide a more precise estimate of λ_m since we used the scaled all-orders potential method, which per definition uses exact (experimental

energies). This is crucial for finding resonances and is also important for most magic wavelengths. Ref. [62] used the so-called *relativistic core polarisation potential method* instead, which is similar to our RPA method.

TABLE XV: Relevant magic wavelengths of two Ra^+ clock transitions, $7s - 6d_{5/2}$ and $7s - 6d_{3/2}$. Projection numbers M are distinguished.

		Ra^+		
Transition	$\|M\|$	λ_m (nm)	Other [62]	$\alpha_0(\lambda_m)$
$7s - 6d_{5/2}$	3/2	1615.55	1824.4(2.5)	111.94
	1/2	434.89	435.315(3)	34.18
$7s - 6d_{3/2}$	3/2	434.82	435.277(4)	34.97
	3/2	742.72	744.93(1)	149.51

G. Sensitivity Coefficients

This section will show the calculated sensitivity coefficients for various transitions to a possible variation of the fine-structure constant. We calculated them at the level of the all-orders as well as the second-order correlation potential method. We also checked the calculations for two different values of δx, for $\delta x = 0.1$ and $\delta x = 0.05$. These lead to the same results, proving that the sensitivity coefficient is indeed linear in this regime. Further details on the computation of this quantity can be found in Refs. [57] and [31]. Table XVI shows the final calculated values for the so-called $q-$values for both ions. For a brief description of their calculation as well as their relation to the sensitivity coefficient κ_α, please refer to Appendix A.

TABLE XVI: Calculated q-values of the transition energies of various Ra^+, Ba^+, and Sr^+ valence states from the valence ground state. The coefficients were evaluated at the level of all orders for the Final value, as well as at second order and are compared to the literature when available.

	Ra^+			Ba^+				Sr^+			
State	$\Sigma^{(2)}$	Final	Other[a]	State	$\Sigma^{(2)}$	Final	Other[a]	State	$\Sigma^{(2)}$	Final	Other[a]
$8s_{1/2}$	7138	8487(675)		$7s_{1/2}$	1833	2285(226)		$6s_{1/2}$	1103	1059(22)	
$7p_{1/2}$	5309	5356(24)		$6p_{1/2}$	1350	1508(79)		$5p_{1/2}$	777	747(15)	
$8p_{1/2}$	8415	9572(579)		$7p_{1/2}$	2196	2633(218)		$6p_{1/2}$	1281	1235(23)	
$7p_{3/2}$	10782	12336(777)		$6p_{3/2}$	2891	3449(279)		$5p_{3/2}$	1664	1611(26)	
$8p_{3/2}$	10510	12014(752)		$7p_{3/2}$	2792	3330(269)		$6p_{3/2}$	1594	1542(26)	
$6d_{3/2}$	16746	19238(1246)	18150	$5d_{3/2}$	5398	6268(435)	6104	$4d_{3/2}$	2985	2915(35)	2828
$6d_{5/2}$	16570	19201(1315)	19000	$5d_{5/2}$	5727	6754(513)	6910	$4d_{5/2}$	3176	3094(41)	3172

[a]Ref. [57]

Standard deviations were estimated by comparing the results at second order ($\Sigma^{(2)}$) with those at all orders ($\Sigma^{(\infty)}$). Half of the absolute difference is estimated as SD.

Our calculated q-values are consistent with the range reported in the literature by Flambaum et al. (2018) ([57]). However, there is notable disagreement between the midpoints of most values, particularly those associated with the Sr^+ ion, where the computed standard deviations are smaller. In this case, the results obtained by Ref. [57] are in fact at least $2\,\sigma$ away from ours.

Furthermore, it can be seen that especially the proposed clock transitions $7s-6d_{3/2}$ and $7s-6d_{5/2}$ in Ra^+ have high sensitivity coefficients to variations in α, with our calculated values being 3.29 and 2.87 for κ_α, respectively. The value for the $7s-6d_{5/2}$ transition in Ra^+ is, in fact, the highest positive value for a working atomic clock so far [57, 71]. Until now, the most sensitive clock with a negative coefficient is based on Yb^+ using an electric octupole (E3) transition with $\kappa_\alpha = -6$ [111]. In conjunction with the high positive enhancement of a Ra^+ optical atomic clock, future measurements could be used to further restrict the variation of the fine-structure constant [71]. Qualitatively, the values for the Barium and Strontium ion are very similar, although noticeably smaller, with values κ_{α,Ba^+} of 1.50 and 1.49 and κ_{α,Sr^+} of 0.41 and 0.43 for the respective $d_{3/2}$ and $d_{5/2}$ transitions. Hence, Ra^+ seems to be a better candidate for future measurements of variations in α. This was also expected, since this effect is known to be more pronounced in heavier atoms [57].

H. Hyperfine A Constants

This section shows the calculated Hyperfine A Constants for the s and $p_{1/2}$ states of Sr^+, Ba^+, and Ra^+, respectively. The final values are given at the level of the scaled all-orders method including QED effects, to which Breit, SR+N, and Bohr-Weisskopf contributions are added.

Experimental values were available for the Strontium and Barium ion. As can be seen in Tables XVII and XVIII, our values deviate at most 0.2% from the experiment for Sr^+ and 0.7% for Ba^+. For these states, we deviate by approximately $0.3\,\sigma$ and $0.5\,\sigma$ for the lowest s valence states and fall just outside the experimental standard deviations of the lowest $p_{1/2}$ valence states in $^{137}Ba^+$. Comparisons with other theoretical calculations in the literature generally show good agreement with our results. Notably, Refs. [113], [92], and [112] all utilised (relativistic) coupled-cluster approaches.

TABLE XVII: Calculated Hyperfine A Constants for $^{87}Sr^+$ in comparison with experiments when available.

			$^{87}Sr^+$				
State	RHF	Final	Other	Exp. [123]	Δ(MHz)	Δ(%)	σ
$5s$	−734.2	−1002.8(8.8)	−997.85[a]	−1000.47	−2.31	0.2	0.3
			−1000.[b]				
$6s$	−234.1	−296.3(1.8)	−296.04[a]				
$7s$	−105.1	−129.94(67)	−129.91[a]				
$5p_{1/2}$	−121.6	−178.64(32)	−177.33[a]				
			−177.[b]				
$6p_{1/2}$	−46.2	−63.65(19)	−63.4[a]				
$7p_{1/2}$	−22.5	−30.37(1.3)	−30.26[a]				

[a]Ref. [113], [b]Ref.[92]

For the Hyperfine A Constants in Ra^+, which are shown in Table XIX, we show different contributions to our calculations since no comparisons were found within the literature. Here, the column 'BW' denotes the Bohr-Weisskopf contribution. We believe that these values should be fairly close to the true values since the two other alkali-like ions, Ba^+ and Sr^+, align well with the available experiments, as discussed before.

TABLE XVIII: Calculated Hyperfine A Constants for $^{137}Ba^{+}$ in comparison with experiments when available.

			$^{137}Ba^{+}$				
State	RHF	Final	Other [112]	Exp.	Δ(MHz)	Δ(%)	σ
$6s$	2935.75	4042.(43.)		4018.871[a]	22.98	0.6	0.54
$7s$	964.95	1216.0(9.4)	1211.73				
$8s$	442.87	543.6(4.1)	542.5				
$6p_{1/2}$	493.71	748.4(4.4)	733.98	743.7(3)[b]	5.01	0.7	1.15
$7p_{1/2}$	193.29	270.9(1.2)	267				
$8p_{1/2}$	96.07	131.06(60)	129.35				

[a]SD: (1.8E-07) by Ref. [8], [b]Ref. [125]

TABLE XIX: Calculated Hyperfine A Constants for $^{226}Ra^{+}$.

			$^{226}Ra^{+}$		
State	RHF	δBreit	δSR+N	BW	Final
$7s$	−3982.00	−17.46	92.22	212.78	−5112.(130.)
$8s$	−1240.44	−3.66	10.73	60.07	−1460.(36.)
$9s$	−563.27	−1.62	3.03	26.55	−647.(16.)
$7p_{1/2}$	−665.15	1.31	−2.07	12.54	−999.(10.)
$8p_{1/2}$	−257.97	0.29	−2.80	4.43	−353.8(3.2)
$9p_{1/2}$	−127.96	0.10	−1.60	2.15	−171.3(1.7)

.

I. Field Shift Constants

We calculated Field Shift Constants for low-lying valence states of the three ions up to the level of the scaled all-orders correlation potential method. No experimental comparisons were available at the time of writing.

Fortunately, theoretical studies are available for $^{137}Ba^{+}$, which is presented in Table XX. Our values show a reasonable correlation with those of Martennson-Pendrill et al. (1992) ([93]) and Berengut et al. (2003) ([6]). Ref. [93] used a relativistic coupled-cluster (RCC) approach, while Ref. [6] used an approach that is similar to the second-order correlation potential method, using many-body perturbation theory (MBPT). For three out of five states with available comparisons, at least one of those groups' values is within our estimated uncertainty. This is the case for the $6s$ and $6p$ states. Interestingly, we tend to agree better with the RCC approach. However, this is not concerning since we evaluate our MBPT calculations up to the level of the scaled all-orders correlation potential and hence also include higher-order correlation effects. For the remaining values, we noticed larger disagreement between our calculations and those of the other groups. Some of the largest differences were observed for the $5d$ states, with deviations of around $2\,\sigma - 2.5\,\sigma$ compared to Ref. [93]. Additionally, we found a very different value for the $6p_{1/2}$ state in comparison to Ref. [6]: $-0.1557(62)$ vs. -0.111.

TABLE XX: Calculated Field Shift Constants for $^{137}Ba^{+}$ compared to other groups.

			$^{137}Ba^{+}$		
State	RHF	$\Sigma^{(2)}$	$\Sigma^{(\infty)}$	Final	Other
$6s_{1/2}$	3.40	4.26	4.06	4.05(20)	3.851[a]
					4.096[b]
$7s_{1/2}$	1.10	1.22	1.20	1.196(25)	
$6p_{1/2}$	−0.13	−0.16	−0.16	−0.1557(62)	−0.151[a]
					−0.111[b]
$7p_{1/2}$	−0.05	−0.06	−0.06	−0.0567(16)	
$6p_{3/2}$	−0.19	−0.24	−0.23	−0.2331(80)	−0.2254[a]
					0.2426[b]
$7p_{3/2}$	−0.07	−0.09	−0.09	−0.0851(20)	
$5d_{3/2}$	−1.10	−1.31	−1.29	−1.273(23)	−1.223[a]
$5d_{5/2}$	−1.02	−1.23	−1.21	−1.196(22)	−1.148[a]

[a]Ref. [6], [b]Ref. [93]

For the other two ions, presented in Table XXI, we show different orders of our calculations. Notably, our values remain largely consistent from the second-order potential method ($\Sigma^{(2)}$) onward, indicating high numerical stability. In particular, when comparing the all-orders potential ($\Sigma^{(\infty)}$) with the scaled all-orders potential ($\lambda\Sigma^{(\infty)}$) values, they remain remarkably stable. This consistency reflects the high precision of the *ab initio* calculations of valence state energies, as demonstrated in Table I.

TABLE XXI: Calculated Field Shift Constants for $^{87}Sr^{+}$ and $^{226}Ra^{+}$.

			$^{87}Sr^{+}$		
State	RHF	$\Sigma^{(2)}$	$\Sigma^{(\infty)}$	$\lambda\Sigma^{(2)}$	Final
$5s_{1/2}$	1.0654	1.2833	1.2412	1.2475	1.243(42)
$6s_{1/2}$	0.3351	0.3675	0.3612	0.3629	0.3619(63)
$5p_{1/2}$	−0.0588	−0.0723	−0.0707	−0.0704	−0.0706(17)
$6p_{1/2}$	−0.0222	−0.0256	−0.0252	−0.0252	−0.02516(44)
$5p_{3/2}$	−0.0660	−0.0806	−0.0788	−0.0786	−0.0788(18)
$6p_{3/2}$	−0.0249	−0.0286	−0.0282	−0.0282	−0.02817(46)
$4d_{3/2}$	−0.2881	−0.3560	−0.3485	−0.3469	−0.3456(75)
$4d_{5/2}$	−0.2795	−0.3456	−0.3384	−0.3369	−0.3356(72)

			$^{226}Ra^{+}$		
State	RHF	$\Sigma^{(2)}$	$\Sigma^{(\infty)}$	$\lambda\Sigma^{(2)}$	Final
$7s_{1/2}$	35.03	41.97	40.68	40.36	40.5(1.3)
$8s_{1/2}$	10.702	11.335	11.301	11.213	11.300(34)
$7p_{1/2}$	0.635	0.851	0.812	0.806	0.806(39)
$8p_{1/2}$	0.230	0.274	0.266	0.266	0.266(8)
$7p_{3/2}$	−1.625	−2.012	−1.965	−1.936	−1.957(47)
$8p_{3/2}$	−0.629	−0.725	−0.713	−0.707	−0.713(11)
$6d_{3/2}$	−7.90	−9.67	−9.48	−9.38	−9.40(19)
$6d_{5/2}$	−6.34	−7.77	−7.65	−7.56	−7.58(12)

V. CONCLUSION AND OUTLOOK

I presented high-precision atomic structure calculations for the low-lying s, p, and d states of the singly-charged ions Sr^+, Ba^+, and Ra^+. Additionally, I compared the results with the available literature and found very good overall agreement for various quantities. Notably, the results for quantities such as reduced electric dipole matrix elements and lifetimes align exceptionally well with experimental data. For other quantities, such as electric quadrupole and magnetic dipole matrix elements, scalar and tensor polarisabilities, or field shift constants, the experimental literature was found to be more limited, especially for the Radium ion. These quantities are generally more challenging to measure, as they are difficult to access with state-of-the-art experimental probes. In the case of Radium, its radioactivity further complicates experiments by increasing costs and making it more difficult to obtain and handle. Nonetheless, the consistency of the results for the lighter Sr^+ and Ba^+ ions strongly suggests that the AMPSCI library is reliable for Ra^+ as well. For the little experimental data that is indeed available for the latter ion, including reduced electric dipole matrix elements as well as certain lifetimes, we are in fact already most often within the given experimental standard deviations. When experimental values weren't available, I compared our calculations to theoretical values from other groups. These comparisons showed decent agreement overall, although some inconsistencies in the literature highlight the need for future experimental work to clarify and refine these theoretical predictions.

Due to the scope of calculated quantities, this work may be one of the most comprehensive summaries of atomic structure calculations for ions under consideration for optical atomic clocks. Furthermore, we are hopeful to support further improvements of those optical atomic clocks towards their projected precisions with our predictions for yet-unknown values, such as polarisabilities and magic wavelengths for the Radium and Strontium ions. Additionally, we are optimistic that future experiments will be able to confirm the precisions of our calculations while also providing valuable insights into the improvement of the precision and reliability of these advanced timekeeping and experimental systems.

APPENDICES

Appendix A: Supplementary Material: Calculation of the sensitivity of the transition frequency to a variation in the fine-structure constant

The frequency of an atomic transition may be expressed as [31, 57]:

$$\omega = \omega_0 + qx$$

where ω_0 is the currently observed transition frequency and x parametrizes a variation in α as:

$$x = \left(\frac{\alpha}{\alpha_0}\right)^2 - 1$$

and q is a sensitivity coefficient. Here, α_0[15] is the currently assumed value for the fine-structure constant whereas α is a possible deviation from it. This variation could be for example over time or of spatial nature. If the variation of α is assumed to be small, q can be determined from the first-order derivative of ω around $x = 0$. In our case, we calculated the relevant transition frequencies and varied α in the Dirac equation. We can then use the approximation:

$$q = \frac{d\omega}{dx}\Big|_{x=0} \approx \frac{\omega(+\delta x) - \omega(-\delta x)}{2\,\delta x}$$

In practice, we take values between $\delta x = 0.05$ and $\delta x = 0.1$. Since q has units of energy it is convenient to further define a dimensionless sensitivity coefficient κ_α via:

$$\frac{\delta\omega}{\omega_0} = \kappa_\alpha \frac{\delta\alpha}{\alpha}$$

which has the following relation to q:

$$\kappa_\alpha = \frac{2q}{\omega_0}$$

We can further calculate the sensitivity of a measurement to a variation in α using two atomic clocks (1) and (2) by subtracting their individual sensitivity coefficients:

$$\Delta\kappa_\alpha = \kappa_\alpha^{(1)} - \kappa_\alpha^{(2)}$$

Therefore, one can infer that using one clock with a particularly large positive enhancement and one with a large negative enhancement will allow for easier measurements of variations in α. For further information about atomic clocks and the search for a possible variation of fundamental physical constants, please inspect Ref. [57].

[15] The currently accepted value for the fine-structure constant is $7.2973525693(11) \cdot 10^{-3}$ [97]. This is approximately $\approx 1/137$.

Appendix B: Additional calculations

1. Large E1 Tables

Sr^+

TABLE XXII: Part 1: All calculated reduced E1 matrix elements for Sr^+. Different approximations are compared with other calculations and experiments when available. All values are given in atomic units ($e\,a_B$) and as absolute values.
† means that our final values lie within the experimental standard deviation.

					Sr^+				
State	RHF	$\Sigma^{(2)}$	$\Sigma^{(\infty)}$	δBreit	δQED	δSR+N	$\delta\lambda$	Final	Exp. [36, 102]
$5p_{1/2}-5s$	3.485	3.043	3.075	0.000	0.001	−0.003	−0.001	3.0712(31)	3.076(24)†
$6p_{1/2}-5s$	0.066	0.041	0.052	−0.001	0.001	−0.015	−0.002	0.0358(56)	
$7p_{1/2}-5s$	0.005	0.074	0.080	0.000	0.001	−0.010	0.000	0.0698(35)	
$5p_{3/2}-5s$	4.921	4.301	4.347	0.000	0.002	−0.004	−0.002	4.3414(44)	4.360(23)†
$6p_{3/2}-5s$	0.161	0.012	0.003	0.000	0.001	0.020	−0.001	0.0232(63)	
$7p_{3/2}-5s$	0.028	0.069	0.077	0.000	0.001	−0.014	0.000	0.0633(48)	
$5p_{1/2}-6s$	2.375	2.349	2.346	0.002	−0.002	−0.021	0.007	2.333(10)	
$6p_{1/2}-6s$	6.810	6.496	6.543	0.000	0.002	−0.013	−0.008	6.5226(89)	
$7p_{1/2}-6s$	0.224	0.188	0.171	0.002	−0.002	0.005	0.006	0.1813(62)	
$5p_{3/2}-6s$	3.497	3.465	3.459	0.001	−0.002	−0.029	0.009	3.440(13)	
$6p_{3/2}-6s$	9.578	9.131	9.199	0.001	0.003	−0.018	−0.010	9.171(12)	
$7p_{3/2}-6s$	0.432	0.388	0.364	0.000	−0.002	0.006	0.007	0.3765(70)	
$5p_{1/2}-7s$	0.640	0.648	0.650	0.000	0.000	−0.007	0.000	0.6431(21)	
$6p_{1/2}-7s$	4.860	4.782	4.771	0.004	−0.003	−0.013	0.013	4.772(14)	
$7p_{1/2}-7s$	11.153	10.823	10.888	−0.001	0.004	−0.012	−0.013	10.863(14)	
$5p_{3/2}-7s$	0.920	0.928	0.931	0.000	0.000	−0.009	0.000	0.9216(28)	
$6p_{3/2}-7s$	7.120	7.024	7.006	0.001	−0.004	−0.019	0.016	7.003(17)	
$7p_{3/2}-7s$	15.652	15.178	15.273	0.001	0.005	−0.016	−0.018	15.239(19)	
$5p_{1/2}-4d_{3/2}$	3.729	3.061	3.095	−0.003	−0.001	−0.024	0.018	3.088(19)	3.093(15)†
$6p_{1/2}-4d_{3/2}$	0.026	0.073	0.067	0.002	0.000	−0.013	−0.012	0.042(12)	
$7p_{1/2}-4d_{3/2}$	0.047	0.040	0.037	0.001	0.000	−0.007	−0.005	0.0247(59)	
$5p_{3/2}-4d_{3/2}$	1.657	1.359	1.375	−0.001	0.000	−0.010	0.008	1.3722(87)	1.378(34)†
$6p_{3/2}-4d_{3/2}$	0.028	0.049	0.046	0.001	0.000	−0.006	−0.005	0.0348(55)	
$7p_{3/2}-4d_{3/2}$	0.028	0.025	0.024	0.000	0.000	0.003	−0.002	0.0250(27)	
$4f_{5/2}-4d_{3/2}$	3.579	2.850	2.892	−0.003	−0.001	−0.027	0.033	2.897(34)	
$5p_{1/2}-5d_{3/2}$	4.331	4.292	4.308	0.005	0.000	−0.021	0.004	4.2923(94)	
$6p_{1/2}-5d_{3/2}$	9.087	8.536	8.582	−0.005	−0.001	−0.028	−0.003	8.550(10)	
$7p_{1/2}-5d_{3/2}$	0.374	0.233	0.241	−0.005	0.000	−0.003	−0.001	0.2365(29)	
$5p_{3/2}-5d_{3/2}$	1.996	1.980	1.986	0.001	0.000	−0.009	0.001	1.9784(39)	
$6p_{3/2}-5d_{3/2}$	4.037	3.787	3.808	−0.002	0.000	−0.012	−0.001	3.7946(41)	
$7p_{3/2}-5d_{3/2}$	0.123	0.059	0.063	−0.001	0.000	−0.001	0.000	0.0614(8)	
$4f_{5/2}-5d_{3/2}$	12.730	12.188	12.239	−0.002	0.000	−0.027	−0.007	12.204(11)	
$5p_{1/2}-6d_{3/2}$	1.466	1.358	1.365	0.000	0.000	−0.001	−0.001	1.3628(18)	
$6p_{1/2}-6d_{3/2}$	7.126	7.188	7.201	0.011	0.001	−0.015	0.016	7.203(18)	
$7p_{1/2}-6d_{3/2}$	16.063	15.426	15.484	−0.007	−0.001	−0.023	−0.015	15.446(17)	
$5p_{3/2}-6d_{3/2}$	0.659	0.608	0.611	0.000	0.000	0.000	−0.001	0.61016(84)	
$6p_{3/2}-6d_{3/2}$	3.297	3.331	3.335	0.003	0.001	−0.007	0.006	3.3347(64)	
$7p_{3/2}-6d_{3/2}$	7.139	6.847	6.874	−0.002	−0.001	−0.010	−0.006	6.8576(71)	
$4f_{5/2}-6d_{3/2}$	5.918	6.276	6.248	0.002	0.001	−0.014	−0.008	6.2262(90)	

TABLE XXIII: Part 2: All calculated reduced E1 matrix elements for Sr^+. Different approximations are compared with other calculations and experiments when available. All values are given in atomic units ($e\,a_B$) and as absolute values.
† means that our final values lie within the experimental standard deviation.

State	RHF	$\Sigma^{(2)}$	$\Sigma^{(\infty)}$	δBreit	Sr^+ δQED	δSR+N	$\delta\lambda$	Final	Exp. [36, 102]
$5p_{1/2}-7d_{3/2}$	0.820	0.739	0.743	0.000	0.000	0.002	−0.002	0.7434(20)	
$6p_{1/2}-7d_{3/2}$	2.421	2.363	2.369	0.001	0.000	−0.003	0.000	2.3666(12)	
$7p_{1/2}-7d_{3/2}$	10.450	10.588	10.601	0.017	0.001	−0.011	0.025	10.615(27)	
$5p_{3/2}-7d_{3/2}$	0.366	0.328	0.330	0.000	0.000	0.001	−0.001	0.3294(9)	
$6p_{3/2}-7d_{3/2}$	1.093	1.064	1.067	0.000	0.000	−0.001	0.000	1.06592(54)	
$7p_{3/2}-7d_{3/2}$	4.847	4.919	4.923	0.004	0.001	−0.005	0.009	4.9276(96)	
$4f_{5/2}-7d_{3/2}$	1.249	1.245	1.248	0.000	0.000	−0.005	−0.001	1.2419(20)	
$5p_{3/2}-4d_{5/2}$	5.003	4.122	4.166	−0.006	−0.001	−0.032	0.023	4.155(26)	4.175(22)†
$6p_{3/2}-4d_{5/2}$	0.076	0.136	0.128	0.003	0.000	−0.016	−0.015	0.097(16)	
$7p_{3/2}-4d_{5/2}$	0.080	0.072	0.069	0.001	0.000	0.009	−0.007	0.0710(79)	
$4f_{5/2}-4d_{5/2}$	0.964	0.772	0.783	−0.001	0.000	−0.007	0.009	0.7836(89)	
$4f_{7/2}-4d_{5/2}$	4.313	3.453	3.501	−0.006	−0.001	−0.033	0.037	3.504(39)	
$5p_{3/2}-5d_{5/2}$	5.956	5.905	5.924	0.006	0.001	−0.027	0.005	5.903(12)	
$6p_{3/2}-5d_{5/2}$	12.164	11.426	11.486	−0.008	−0.001	−0.037	−0.005	11.443(13)	
$7p_{3/2}-5d_{5/2}$	0.402	0.215	0.225	−0.006	−0.001	−0.004	−0.001	0.2202(34)	
$4f_{5/2}-5d_{5/2}$	3.406	3.263	3.276	−0.001	0.000	−0.007	−0.002	3.2668(31)	
$4f_{7/2}-5d_{5/2}$	15.232	14.591	14.650	−0.003	0.000	−0.032	−0.008	14.610(13)	
$5p_{3/2}-6d_{5/2}$	1.980	1.830	1.839	−0.001	0.000	−0.001	−0.002	1.8361(26)	
$6p_{3/2}-6d_{5/2}$	9.822	9.913	9.930	0.012	0.001	−0.020	0.019	9.930(21)	
$7p_{3/2}-6d_{5/2}$	21.493	20.633	20.710	−0.011	−0.002	−0.031	−0.020	20.658(23)	
$4f_{5/2}-6d_{5/2}$	1.568	1.662	1.655	0.001	0.000	−0.004	−0.002	1.6497(22)	
$4f_{7/2}-6d_{5/2}$	7.011	7.432	7.400	0.006	0.001	−0.017	−0.004	7.3793(69)	
$5p_{3/2}-7d_{5/2}$	1.100	0.989	0.995	−0.001	0.000	0.002	−0.003	0.9944(29)	
$6p_{3/2}-7d_{5/2}$	3.277	3.193	3.202	0.000	0.000	−0.004	−0.001	3.1983(16)	
$7p_{3/2}-7d_{5/2}$	14.424	14.627	14.643	0.019	0.002	−0.015	0.032	14.660(34)	
$4f_{5/2}-7d_{5/2}$	0.333	0.333	0.334	0.000	0.000	−0.001	0.000	0.33178(53)	
$4f_{7/2}-7d_{5/2}$	1.490	1.487	1.491	0.000	0.000	−0.006	−0.001	1.4837(22)	

Ba$^+$

TABLE XXIV: Part 1: All calculated reduced E1 matrix elements for Ba^+. Different approximations are compared with other calculations and experiments when available. All values are given in atomic units ($e\,a_B$) and as absolute values.
† means that our final values lie within the experimental standard deviation.

					Ba^+				
State	RHF	$\Sigma^{(2)}$	$\Sigma^{(\infty)}$	δBreit	δQED	δSR+N	$\delta\lambda$	Final	Exp. [120]
$6p_{1/2}$-$6s$	3.891	3.261	3.319	0.000	0.002	−0.001	0.003	3.3214(80)	3.36(4)†
$7p_{1/2}$-$6s$	0.065	0.089	0.106	−0.001	0.002	−0.025	0.000	0.082(44)	0.24(3)
$8p_{1/2}$-$6s$	0.007	0.107	0.115	−0.001	0.001	−0.016	0.001	0.100(29)	0.10(1)†
$6p_{3/2}$-$6s$	5.478	4.602	4.687	0.000	0.003	−0.002	0.004	4.689(11)	4.55(10)
$7p_{3/2}$-$6s$	0.261	0.051	0.028	0.000	−0.002	0.033	−0.001	0.058(58)	0.33(4)
$8p_{3/2}$-$6s$	0.079	0.060	0.071	0.000	0.001	−0.022	0.002	0.051(39)	0.15(2)
$6p_{1/2}$-$7s$	2.549	2.499	2.500	0.004	−0.003	−0.032	0.011	2.480(57)	
$7p_{1/2}$-$7s$	7.392	6.947	7.027	−0.001	0.004	−0.019	−0.004	7.005(34)	
$8p_{1/2}$-$7s$	0.199	0.138	0.114	0.003	−0.004	0.008	0.004	0.125(17)	
$6p_{3/2}$-$7s$	3.957	3.899	3.895	0.001	−0.004	−0.044	0.012	3.863(78)	
$7p_{3/2}$-$7s$	10.312	9.679	9.798	0.000	0.006	−0.026	−0.005	9.768(47)	
$8p_{3/2}$-$7s$	0.568	0.502	0.466	0.000	−0.004	0.010	0.004	0.480(20)	
$6p_{1/2}$-$8s$	0.702	0.708	0.711	0.000	0.000	−0.010	0.000	0.701(18)	
$7p_{1/2}$-$8s$	5.088	4.966	4.958	0.006	−0.006	−0.021	0.015	4.953(40)	
$8p_{1/2}$-$8s$	11.917	11.464	11.571	−0.002	0.006	−0.018	−0.007	11.546(34)	
$6p_{3/2}$-$8s$	1.029	1.029	1.035	0.000	0.000	−0.013	0.000	1.022(23)	
$7p_{3/2}$-$8s$	7.810	7.678	7.657	0.002	−0.008	−0.030	0.017	7.645(54)	
$8p_{3/2}$-$8s$	16.551	15.888	16.049	0.001	0.009	−0.024	−0.010	16.015(46)	
$6p_{1/2}$-$5d_{3/2}$	3.745	3.009	3.040	−0.004	−0.001	−0.031	0.026	3.033(56)	2.90(9)
$7p_{1/2}$-$5d_{3/2}$	0.351	0.259	0.266	0.002	0.000	0.014	−0.012	0.267(25)	0.19(5)
$8p_{1/2}$-$5d_{3/2}$	0.196	0.121	0.126	0.001	0.000	0.009	−0.007	0.127(16)	0.10(3)†
$6p_{3/2}$-$5d_{3/2}$	1.635	1.313	1.327	−0.002	−0.001	−0.012	0.012	1.326(22)	
$7p_{3/2}$-$5d_{3/2}$	0.186	0.147	0.150	0.001	0.000	0.007	−0.005	0.151(12)	
$8p_{3/2}$-$5d_{3/2}$	0.102	0.071	0.073	0.000	0.000	0.004	−0.003	0.0741(79)	
$4f_{5/2}$-$5d_{3/2}$	4.206	3.473	3.725	−0.034	−0.002	−0.053	0.023	3.67(11)	
$5f_{5/2}$-$5d_{3/2}$	2.331	0.690	0.456	0.079	−0.012	−0.029	−0.277	0.30(17)	
$6p_{1/2}$-$6d_{3/2}$	5.141	4.838	4.898	0.007	0.001	−0.027	0.013	4.885(51)	
$7p_{1/2}$-$6d_{3/2}$	9.189	8.630	8.673	−0.007	−0.002	−0.040	−0.005	8.627(71)	
$8p_{1/2}$-$6d_{3/2}$	0.088	0.102	0.117	0.006	0.001	0.002	0.002	0.122(10)	
$6p_{3/2}$-$6d_{3/2}$	2.446	2.314	2.339	0.002	0.000	−0.012	0.004	2.331(23)	
$7p_{3/2}$-$6d_{3/2}$	4.020	3.767	3.786	−0.002	−0.001	−0.017	−0.002	3.767(30)	
$8p_{3/2}$-$6d_{3/2}$	0.130	0.142	0.147	0.001	0.000	0.001	0.001	0.1481(25)	
$4f_{5/2}$-$6d_{3/2}$	12.333	5.681	8.343	−0.202	−0.025	−0.044	−0.453	7.92(39)	
$5f_{5/2}$-$6d_{3/2}$	5.144	11.846	10.282	0.081	0.020	−0.040	0.441	10.65(22)	
$6p_{1/2}$-$7d_{3/2}$	1.551	1.375	1.385	−0.001	0.000	0.004	−0.004	1.3856(73)	
$7p_{1/2}$-$7d_{3/2}$	8.360	8.136	8.218	0.015	0.001	−0.023	0.028	8.223(48)	
$8p_{1/2}$-$7d_{3/2}$	16.195	15.567	15.617	−0.010	−0.002	−0.034	−0.020	15.563(62)	
$6p_{3/2}$-$7d_{3/2}$	0.690	0.606	0.610	0.000	0.000	0.002	−0.002	0.6095(31)	
$7p_{3/2}$-$7d_{3/2}$	4.009	3.924	3.957	0.003	0.001	−0.010	0.010	3.957(20)	
$8p_{3/2}$-$7d_{3/2}$	7.096	6.804	6.827	−0.003	−0.001	−0.015	−0.009	6.804(26)	
$5f_{5/2}$-$7d_{3/2}$	22.119	10.161	12.999	−0.170	−0.039	−0.067	−0.720	12.23(40)	

TABLE XXV: Part 2: All calculated reduced E1 matrix elements for Ba^+. Different approximations are compared with other calculations and experiments when available. All values are given in atomic units ($e\,a_B$) and as absolute values.

					Ba^+				
State	RHF	$\Sigma^{(2)}$	$\Sigma^{(\infty)}$	δBreit	δQED	δSR+N	$\delta\lambda$	Final	Exp.
$6p_{1/2}$-$8d_{3/2}$	0.844	0.725	0.730	−0.001	0.000	0.006	−0.004	0.731(11)	
$7p_{1/2}$-$8d_{3/2}$	2.568	2.460	2.472	0.000	0.000	−0.003	−0.002	2.4676(56)	
$8p_{1/2}$-$8d_{3/2}$	12.196	11.959	12.070	0.023	0.002	−0.018	0.045	12.098(51)	
$6p_{3/2}$-$8d_{3/2}$	0.367	0.310	0.312	0.000	0.000	0.003	−0.002	0.3127(46)	
$7p_{3/2}$-$8d_{3/2}$	1.154	1.100	1.105	0.000	0.000	−0.001	−0.002	1.1024(23)	
$8p_{3/2}$-$8d_{3/2}$	5.876	5.800	5.843	0.005	0.002	−0.008	0.018	5.853(18)	
$5f_{5/2}$-$8d_{3/2}$	7.009	1.220	0.418	0.027	0.015	−0.031	0.268	0.62(12)	
$6p_{3/2}$-$5d_{5/2}$	5.001	4.059	4.095	−0.008	−0.002	−0.045	0.036	4.084(81)	
$7p_{3/2}$-$5d_{5/2}$	0.543	0.429	0.439	0.002	0.001	0.014	−0.015	0.438(27)	
$8p_{3/2}$-$5d_{5/2}$	0.298	0.208	0.215	0.001	0.000	0.009	−0.008	0.215(17)	
$4f_{5/2}$-$5d_{5/2}$	1.146	0.951	1.022	−0.010	−0.001	−0.016	0.005	1.005(32)	
$4f_{7/2}$-$5d_{5/2}$	5.129	4.338	4.591	−0.046	−0.002	−0.068	0.033	4.52(14)	
$5f_{7/2}$-$5d_{5/2}$	2.811	0.676	0.693	0.116	−0.013	−0.041	−0.329	0.54(23)	
$6p_{3/2}$-$6d_{5/2}$	7.253	6.860	6.937	0.007	0.001	−0.034	0.013	6.917(65)	
$7p_{3/2}$-$6d_{5/2}$	12.217	11.471	11.525	−0.011	−0.002	−0.053	−0.006	11.465(94)	
$8p_{3/2}$-$6d_{5/2}$	0.318	0.350	0.368	0.006	0.001	0.001	0.002	0.371(10)	
$5f_{5/2}$-$6d_{5/2}$	1.423	3.197	2.787	0.020	0.005	−0.011	0.115	2.883(58)	
$4f_{7/2}$-$6d_{5/2}$	14.748	7.199	10.218	−0.280	−0.026	−0.051	−0.510	9.75(51)	
$5f_{7/2}$-$6d_{5/2}$	6.374	14.095	12.216	0.119	0.022	−0.050	0.527	12.65(29)	
$6p_{3/2}$-$7d_{5/2}$	2.088	1.843	1.855	−0.002	0.000	0.006	−0.006	1.856(12)	
$7p_{3/2}$-$7d_{5/2}$	11.849	11.586	11.687	0.015	0.002	−0.030	0.033	11.691(60)	
$8p_{3/2}$-$7d_{5/2}$	21.519	20.660	20.726	−0.016	−0.003	−0.044	−0.028	20.654(82)	
$5f_{5/2}$-$7d_{5/2}$	5.919	2.676	3.442	−0.045	−0.011	−0.018	−0.194	3.24(11)	
$5f_{7/2}$-$7d_{5/2}$	26.473	12.420	15.929	−0.251	−0.045	−0.077	−0.894	14.99(54)	
$6p_{3/2}$-$8d_{5/2}$	1.119	0.953	0.959	−0.002	0.000	0.009	−0.006	0.961(16)	
$7p_{3/2}$-$8d_{5/2}$	3.476	3.321	3.335	−0.001	0.000	−0.003	−0.004	3.3285(64)	
$8p_{3/2}$-$8d_{5/2}$	17.331	17.083	17.220	0.025	0.004	−0.024	0.057	17.253(61)	

Ra$^+$

TABLE XXVI: Part 1: All calculated reduced E1 matrix elements for Ra^+. Different approximations are compared with other calculations and experiments when available. All values are given in atomic units ($e\,a_B$) and as absolute values.
† means that our final values lie within the experimental standard deviation.

					Ra^+				
State	RHF	$\Sigma^{(2)}$	$\Sigma^{(\infty)}$	δBreit	δQED	δSR+N	$\delta\lambda$	Final	Exp. [64]
$7p_{1/2}$-$7s$	3.877	3.167	3.230	0.000	0.004	0.000	0.005	3.2352(71)	3.229(9)†
$8p_{1/2}$-$7s$	0.125	0.071	0.088	−0.002	0.004	−0.027	0.001	0.064(10)	
$9p_{1/2}$-$7s$	0.024	0.100	0.102	−0.001	0.002	−0.017	−0.012	0.075(13)	
$7p_{3/2}$-$7s$	5.340	4.388	4.483	0.000	0.007	0.002	0.007	4.494(10)	4.484(13)†
$8p_{3/2}$-$7s$	0.625	0.364	0.344	0.000	−0.003	0.034	−0.003	0.374(13)	
$9p_{3/2}$-$7s$	0.281	0.110	0.110	0.000	−0.002	0.024	−0.010	0.123(12)	
$7p_{1/2}$-$8s$	2.637	2.532	2.538	0.006	−0.005	−0.034	0.015	2.519(18)	
$8p_{1/2}$-$8s$	7.371	6.896	6.980	−0.001	0.007	−0.022	−0.002	6.9574(87)	
$9p_{1/2}$-$8s$	0.275	0.175	0.164	0.005	−0.007	0.009	0.049	0.222(50)	
$7p_{3/2}$-$8s$	4.810	4.681	4.675	0.001	−0.006	−0.046	0.011	4.640(18)	
$8p_{3/2}$-$8s$	9.881	9.206	9.342	0.001	0.012	−0.027	−0.002	9.315(11)	
$9p_{3/2}$-$8s$	1.140	1.051	1.041	0.000	−0.007	0.009	−0.020	1.029(20)	
$7p_{1/2}$-$9s$	0.716	0.711	0.716	0.001	0.000	−0.009	0.000	0.7072(27)	
$8p_{1/2}$-$9s$	5.227	5.040	5.039	0.011	−0.010	−0.024	0.014	5.030(17)	
$9p_{1/2}$-$9s$	11.873	11.413	11.512	−0.003	0.012	−0.021	−0.051	11.441(51)	
$7p_{3/2}$-$9s$	1.078	1.035	1.048	0.000	0.001	−0.009	−0.002	1.0368(33)	
$8p_{3/2}$-$9s$	9.244	9.074	9.050	0.002	−0.013	−0.033	0.013	9.029(16)	
$9p_{3/2}$-$9s$	15.713	14.999	15.149	0.002	0.021	−0.025	0.031	15.156(33)	
$7p_{1/2}$-$6d_{3/2}$	4.446	3.489	3.540	−0.006	−0.003	−0.024	0.021	3.533(22)	3.564(27)
$8p_{1/2}$-$6d_{3/2}$	0.105	0.019	0.020	0.005	0.002	−0.028	−0.013	−0.021(16)	
$9p_{1/2}$-$6d_{3/2}$	0.087	0.004	0.005	−0.002	0.000	−0.016	0.007	−0.0105(83)	
$7p_{3/2}$-$6d_{3/2}$	1.881	1.477	1.499	−0.002	−0.002	−0.007	0.010	1.502(11)	1.513(11)†
$8p_{3/2}$-$6d_{3/2}$	0.168	0.132	0.131	0.001	0.001	0.013	−0.005	0.1388(63)	
$9p_{3/2}$-$6d_{3/2}$	0.094	0.059	0.063	0.000	0.000	0.009	−0.005	0.0673(54)	
$5f_{5/2}$-$6d_{3/2}$	5.355	4.309	4.447	−0.020	−0.005	−0.051	0.026	4.407(34)	
$7p_{3/2}$-$7d_{3/2}$	4.527	4.297	4.352	0.013	0.003	−0.034	0.024	4.346(29)	
$8p_{3/2}$-$7d_{3/2}$	10.207	9.518	9.582	−0.009	−0.004	−0.045	−0.010	9.527(17)	
$9p_{3/2}$-$7d_{3/2}$	0.514	0.479	0.453	−0.012	−0.002	−0.009	−0.071	0.373(71)	
$7p_{3/2}$-$7d_{3/2}$	2.488	2.390	2.409	0.002	0.001	−0.016	0.007	2.3997(91)	
$8p_{3/2}$-$7d_{3/2}$	4.331	4.015	4.045	−0.003	−0.002	−0.017	−0.005	4.0230(72)	
$9p_{3/2}$-$7d_{3/2}$	0.094	0.125	0.133	0.002	0.001	0.003	−0.006	0.1289(66)	
$5f_{5/2}$-$7d_{3/2}$	11.776	6.700	8.164	−0.143	−0.027	−0.062	−0.254	7.86(27)	
$6f_{5/2}$-$7d_{3/2}$	8.000	12.184	11.311	0.073	0.017	−0.059	0.277	11.50(28)	
$7p_{1/2}$-$8d_{3/2}$	1.584	1.432	1.446	0.000	0.000	0.000	−0.002	1.4454(30)	
$8p_{1/2}$-$8d_{3/2}$	7.184	7.007	7.083	0.026	0.005	−0.026	0.039	7.097(42)	
$9p_{1/2}$-$8d_{3/2}$	17.580	16.855	16.915	−0.012	−0.005	−0.039	−0.074	16.803(75)	
$7p_{3/2}$-$8d_{3/2}$	0.733	0.643	0.649	−0.001	0.000	0.000	−0.002	0.6467(25)	
$8p_{3/2}$-$8d_{3/2}$	4.047	4.007	4.030	0.005	0.003	−0.012	0.014	4.031(15)	
$9p_{3/2}$-$8d_{3/2}$	7.492	7.137	7.158	−0.005	−0.003	−0.016	0.001	7.1440(55)	
$6f_{5/2}$-$8d_{3/2}$	21.143	12.279	14.283	−0.185	−0.046	−0.090	−0.527	13.67(54)	

TABLE XXVII: Part 2: All calculated reduced E1 matrix elements for Ra^+. Different approximations are compared with other calculations and experiments when available. All values are given in atomic units ($e\,a_B$) and as absolute values.
† means that our final values lie within the experimental standard deviation.

					Ra^+				
State	RHF	$\Sigma^{(2)}$	$\Sigma^{(\infty)}$	δBreit	δQED	δSR+N	$\delta\lambda$	Final	Exp. [64]
$7p_{1/2}$-$9d_{3/2}$	0.904	0.798	0.805	−0.001	0.000	0.004	−0.004	0.8061(42)	
$8p_{1/2}$-$9d_{3/2}$	2.531	2.444	2.460	0.003	0.000	−0.006	0.003	2.4585(43)	
$9p_{1/2}$-$9d_{3/2}$	10.311	10.094	10.249	0.040	0.006	−0.019	0.271	10.50(27)	
$7p_{3/2}$-$9d_{3/2}$	0.395	0.333	0.336	−0.001	0.000	0.002	−0.003	0.3351(27)	
$8p_{3/2}$-$9d_{3/2}$	1.201	1.145	1.151	0.000	0.000	−0.002	−0.002	1.1474(19)	
$9p_{3/2}$-$9d_{3/2}$	5.896	5.879	5.943	0.008	0.003	−0.010	−0.014	5.920(15)	
$7p_{3/2}$-$6d_{5/2}$	5.862	4.761	4.802	−0.011	−0.004	−0.042	0.030	4.785(34)	4.788(14)†
$8p_{3/2}$-$6d_{5/2}$	0.462	0.351	0.361	0.004	0.002	0.021	−0.015	0.366(17)	
$9p_{3/2}$-$6d_{5/2}$	0.263	0.165	0.183	0.002	0.000	0.013	−0.015	0.180(16)	
$5f_{5/2}$-$6d_{5/2}$	1.480	1.223	1.259	−0.007	−0.001	−0.019	0.006	1.2420(92)	
$5f_{7/2}$-$6d_{5/2}$	6.638	5.560	5.669	−0.027	−0.004	−0.079	0.034	5.604(44)	
$7p_{3/2}$-$7d_{5/2}$	7.249	6.921	6.996	0.011	0.004	−0.037	0.019	6.980(28)	
$8p_{3/2}$-$7d_{5/2}$	13.372	12.517	12.578	−0.016	−0.006	−0.056	−0.012	12.509(22)	
$9p_{3/2}$-$7d_{5/2}$	0.090	0.142	0.185	0.011	0.002	0.005	−0.022	0.168(23)	
$5f_{5/2}$-$7d_{5/2}$	3.140	1.751	2.151	−0.038	−0.007	−0.015	−0.069	2.070(74)	
$6f_{5/2}$-$7d_{5/2}$	2.259	3.360	3.136	0.016	0.005	−0.018	0.070	3.181(71)	
$5f_{7/2}$-$7d_{5/2}$	13.994	8.416	9.944	−0.176	−0.027	−0.065	−0.258	9.63(28)	
$6f_{7/2}$-$7d_{5/2}$	10.164	14.700	13.752	0.091	0.018	−0.075	0.299	13.94(30)	
$7p_{3/2}$-$8d_{5/2}$	2.227	1.988	2.003	−0.002	−0.001	0.006	−0.004	2.0046(58)	
$8p_{3/2}$-$8d_{5/2}$	11.680	11.479	11.578	0.024	0.007	−0.032	0.032	11.579(37)	
$9p_{3/2}$-$8d_{5/2}$	23.033	22.085	22.118	−0.022	−0.006	−0.048	0.014	22.084(23)	
$6f_{5/2}$-$8d_{5/2}$	5.625	3.170	3.723	−0.048	−0.013	−0.023	−0.146	3.56(15)	
$6f_{7/2}$-$8d_{5/2}$	25.130	15.148	17.405	−0.250	−0.049	−0.097	−0.595	16.72(61)	
$7p_{3/2}$-$9d_{5/2}$	1.218	1.053	1.060	−0.002	−0.001	0.009	−0.007	1.0627(75)	
$8p_{3/2}$-$9d_{5/2}$	3.616	3.471	3.488	−0.001	0.000	−0.004	−0.003	3.4818(37)	
$9p_{3/2}$-$9d_{5/2}$	16.923	16.740	16.978	0.038	0.006	−0.026	−0.043	16.910(48)	

2. Dynamic Polarisabilities

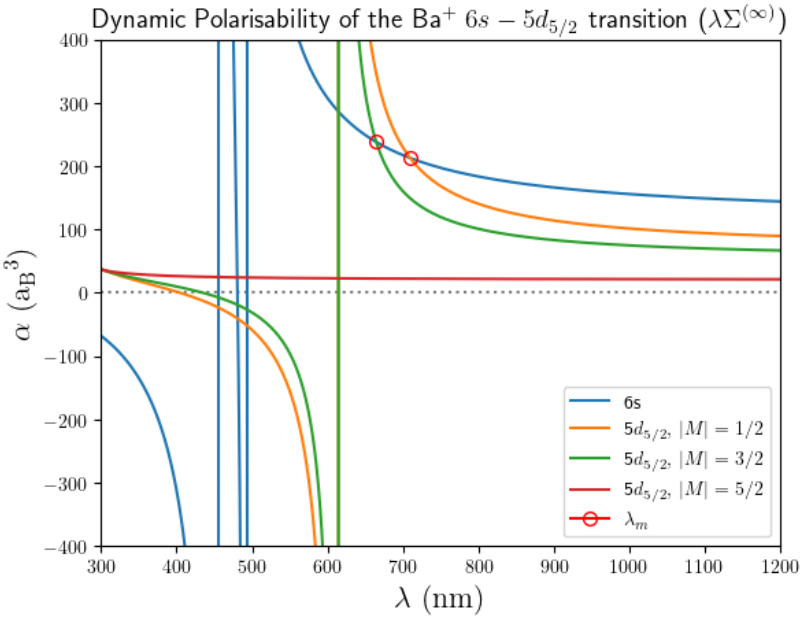

FIG. 15: Plot of the dynamic polarisability of the $6s - 5d_{5/2}$ transition in Ba^+ over the wavelength using the scaled all-orders potential method. Suitable magic wavelengths λ_m are indicated by a red circle.

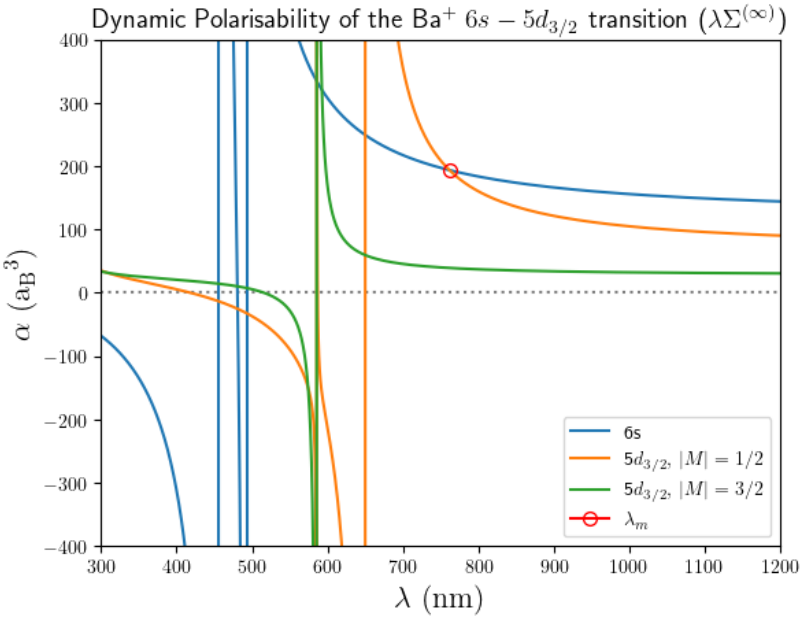

FIG. 16: Plot of the dynamic polarisability of the $6s - 5d_{3/2}$ transition in Ba^+ over the wavelength using the scaled all-orders potential method. Suitable magic wavelengths λ_m are indicated by a red circle.

LIST OF TABLES

LIST OF FIGURES

[1] Nobel Prize Outreach AB. The Nobel Prize in Physics 2005. NobelPrize.org, 2024. Accessed: 15/10/2024.

[2] B. Arora, M. S. Safronova, and C. W. Clark. Magic wavelengths for the $np-ns$ transitions in alkali-metal atoms. *Phys. Rev. A*, 76:052509, 2007. doi:10.1103/PhysRevA.76.052509.

[3] C. Auchter, T. W. Noel, M. R. Hoffman, S. R. Williams, and B. B. Blinov. Measurement of the branching fractions and lifetime of the $5D_{5/2}$ level of Ba^+. *Phys. Rev. A*, 90:060501, 2014. doi:10.1103/PhysRevA.90.060501.

[4] A. Banerjee, D. Budker, M. Filzinger, N. Huntemann, G. Paz, G. Perez, S. Porsev, and M. Safronova. Oscillating nuclear charge radii as sensors for ultralight dark matter. *arXiv:2301.10784 [hep-ph]*, 2023. doi:10.48550/arXiv.2301.10784.

[5] K. Beloy and A. Derevianko. Application of the dual-kinetic-balance sets in the relativistic many-body problem of atomic structure. *Comp. Phys. Commun.*, 179:310–319, 2008. doi:10.1016/j.cpc.2008.03.004.

[6] J. C. Berengut, V. A. Dzuba, and V. V. Flambaum. Isotope-shift calculations for atoms with one valence electron. *Phys. Rev. A*, 68:022502, 2003. doi:10.1103/physreva.68.022502.

[7] H. A. Bethe and E. E. Salpeter. *Quantum Mechanics of One- and Two-Electron Atoms*. Plenum Publishing, New York, 1977. ISBN 978-3-662-12869-5. doi:10.1007/978-3-662-12869-5.

[8] R. Blatt and G. Werth. Precision determination of the ground-state hyperfine splitting in $^{137}Ba^+$ using the ion-storage technique. *Phys. Rev. A*, 25:1476, 1982. doi:10.1103/PhysRevA.25.1476.

[9] S. A. Blundell, D. S. Guo, W. R. Johnson, and J. Sapirstein. Formulas from first-, second-, and third-order perturbation theory for atoms with one valence electron. *At. Data Nucl. Data Tables*, 37: 103–119, 1987. doi:10.1016/0092-640X(87)90006-4.

[10] S. A. Blundell, W. R. Johnson, and J. Sapirstein. Relativistic all-order calculations of energies and matrix elements in cesium. *Phys. Rev. A*, 43:3407, 1991. doi:10.1103/PhysRevA.43.3407.

[11] F. Coester and H. Kümmel. Short-range correlations in nuclear wave functions. *Nucl. Phys.*, 17: 477–485, 1960. doi:10.1016/0029-5582(60)90140-1.

[12] Boulder Atomic Clock Optical Network (BACON) Collaboration. Frequency Ratio Measurements with 18-digit Accuracy Using a Network of Optical Clocks. *Nature*, 591:564–569, 2021. doi:10.1038/s41586-021-03253-4.

[13] P. Delva, H. Denker, and G. Lion. *Chronometric Geodesy: Methods and Applications*. Springer International Publishing, 2019. ISBN 978-3-030-11500-5. doi:10.1007/978-3-030-11500-5˙2.

[14] A. Derevianko. Reconciliation of the Measurement of Parity Nonconservation in Cs with the Standard Model. *Phys. Rev. Lett.*, 85:1618, 2000. doi:10.1103/PhysRevLett.85.1618.

[15] A. Derevianko. Correlated many-body treatment of the Breit interaction with application to cesium atomic properties and parity violation. *Phys. Rev. A*, 65:012106, 2001. doi:10.1103/PhysRevA.65.012106.

[16] A. Derevianko and H. Katori. Colloquium: Physics of optical lattice clocks. *Rev. Mod. Phys.*, 83:331, 2010. doi:10.1103/REVMODPHYS.83.331.

[17] A. Derevianko, B. Ravaine, and W. R. Johnson. Relaxation effect and radiative corrections in many-electron atoms. *Phys. Rev. A*, 69:054502, 2004. doi:10.1103/PhysRevA.69.054502.

[18] A. Derevianko, S. G. Porsev, and K. Beloy. Convergence of all-order many-body methods: Coupled-cluster study for Li. *Phys. Rev. A*, 78:010503, 2008. doi:10.1103/PhysRevA.78.010503.

[19] P. Dubé, A. A. Madej, Z. Zhou, and J. E. Bernard. Evaluation of systematic shifts of the $^{88}Sr^+$ single-ion optical frequency standard at the 10^{-17} level. *Phys. Rev. A*, 87:023806, 2013. doi:10.1103/PhysRevA.87.023806.

[20] P. Dubé, A. A. Madej, M. Tibbo, and J. E. Bernard. High-Accuracy Measurement of the Differential Scalar Polarizability of a $^{88}Sr^+$ Clock Using the Time-Dilation Effect. *Phys. Rev. Lett.*, 112:173002, 2014. doi:10.1103/PhysRevLett.112.173002.

[21] P. Dubé, A. A. Madej, and B. Jian. Sr^+ single-ion clock. *J. Phys.: Conf. Ser.*, 723, 2016. doi:10.1088/1742-6596/723/1/012018.

[22] V. A. Dzuba, V. V. Flambaum, and O. P. Sushkov. Relativistic many-body calculations of energy levels and of fine-structure intervals in the caesium atom. *J. Phys. B: At. Mol. Opt. Phys.*, 16:715, 1983. doi:10.1088/0022-3700/16/5/007.

[23] V. A. Dzuba, V. V. Flambaum, and O. P. Sushkov. Relativistic many-body calculations of the hyperfine-structure intervals in caesium and francium atoms. *J. Phys. B: At. Mol. Opt. Phys.*, 17: 1953, 1984. doi:10.1088/0022-3700/17/10/005.

[24] V. A. Dzuba, V. V. Flambaum, P. G. Silvestrov, and O. P. Sushkov. Relativistic many-body calculations in atoms and parity violation in caesium. *J. Phys. B: At. Mol. Opt. Phys.*, 18:597, 1985. doi:10.1088/0022-3700/18/4/008.

[25] V. A. Dzuba, V. V. Flambaum, P. G. Silvestrov, and O. P. Sushkov. Correlation potential method for the calculation of energy levels, hyperfine structure and E1 transition amplitudes in atoms with one unpaired electron. *J. Phys. B: At. Mol. Opt. Phys.*, 20:1399, 1987. doi:10.1088/0022-3700/20/7/009.

[26] V. A. Dzuba, V. V. Flambaum, P. G. Silvestrov, and O. P. Sushkov. Calculation of parity nonconservation in thallium. *J. Phys. B: At. Mol. Opt. Phys.*, 20:3297, 1987. doi:10.1088/0022-3700/20/14/005.

[27] V. A. Dzuba, V. V. Flambaum, A. Y. Krafmakher, and O. P. Sushkov. Summation of the high orders of perturbation theory in the correlation correction to the hyperfine structure and to the amplitudes of E1-transitions in the caesium atom. *Phys. Lett. A*, 142:373–377, 1989. doi:10.1016/0375-9601(89)90385-X.

[28] V. A. Dzuba, V. V. Flambaum, and O. P. Sushkov. Summation of the high orders of perturbation theory for the parity nonconserving E1-amplitude of the 6s–7s transition in the caesium atom. *Phys. Lett. A*, 141:147–153, 1989. doi:10.1016/0375-9601(89)90777-9.

[29] V. A. Dzuba, V. V. Flambaum, and W. A. King. Summation of the Dominating Diagrams in Many-body Perturbation Theory. *Aust. J. Phys.*, 49:231–246, 1996. doi:10.1071/PH960231.

[30] V. A. Dzuba, C. Harabati, W. R. Johnson, and M. S. Safronova. Breit correction to the parity-nonconservation amplitude in cesium. *Phys. Rev. A*, 63:044103, 2001. doi:10.1103/PhysRevA.63.044103.

[31] A. Hees et al. Search for a Variation of the Fine Structure Constant around the Supermassive Black Hole in Our Galactic Center. *Phys. Rev. Lett.*, 124:081101, 2020. doi:10.1103/PhysRevLett.124.081101.

[32] B. M. Roberts et al. Quantum electrodynamics corrections to energies, transition amplitudes, and parity nonconservation in Rb, Cs, Ba^+, Tl, Fr, and Ra^+. *Phys. Rev. A*, 87:054502, 2013. doi:10.1103/PhysRevA.87.054502.

[33] B. M. Roberts et al. Search for transient variations of the fine structure constant and dark matter using fiber-linked optical atomic clocks. *New J. Phys.*, 22:093010, 2020. doi:10.1088/1367-2630/abaace.

[34] E. Biémont et al. Lifetimes of metastable states in Sr II. *Eur. Phys. J. D*, 11:355–365, 2000. doi:10.1007/s100530070063.

[35] E. Reinhold et al. Indication of a Cosmological Variation of the Proton-Electron Mass Ratio Based on Laboratory Measurement and Reanalysis of H_2 Spectra. *Phys. Rev. Lett.*, 96:151101, 2006. doi:10.1103/PhysRevLett.96.151101.

[36] H. Zhang et al. Iterative precision measurement of branching ratios applied to $5P$ states in $^{88}Sr^+$. *New Journal of Physics*, 18:123021, 2016. doi:10.1088/1367-2630/aa511d.

[37] J. Gurell et al. Laser-probing measurements and calculations of lifetimes of the $5d^2D_{3/2}$ and $5d^2D_{5/2}$ metastable levels in Ba II. *Phys. Rev. A*, 75:052506, 2007. doi:10.1103/PhysRevA.75.052506.

[38] K. J. Arnold et al. Measurements of the branching ratios for $6P_{1/2}$ decays in $^{138}Ba^+$. *Phys. Rev. A*, 100:032503, 2019. doi:10.1103/PhysRevA.100.032503.

[39] L. W. Wansbeek et al. Charge radii of radium isotopes. *Phys. Rev. C*, 86:015503, 2012. doi:10.1103/PhysRevC.86.015503.

[40] M. Nuñez Portela et al. Ra^+ ion trapping: toward an atomic parity violation measurement and an optical clock. *Appl. Phys. B*, 114:173–182, 2014. doi:10.1007/s00340-013-5603-2.

[41] M. S. Safronova et al. Search for new physics with atoms and molecules. *Rev. Mod. Phys.*, 90:025008, 2018. doi:10.1103/RevModPhys.90.025008.

[42] M. Takamoto et al. Test of general relativity by a pair of optical lattice clocks. *Nat. Photonics*, 14: 411–415, 2020. doi:10.1038/s41566-020-0619-8.

[43] N. Huntemann et al. Single-Ion Atomic Clock with 3×10^{-18} Systematic Uncertainty. *Phys. Rev. Lett.*, 116:063001, 2016. doi:10.1103/PhysRevLett.116.063001.

[44] N. Poli et al. Optical atomic clocks. *La Rivista del Nuovo Cimento*, 36, 2013. doi:10.1393/ncr/i2013-10095-x.

[45] O. O. Versolato et al. Atomic parity violation in a single trapped radium ion. *Can. J. Phys.*, 89, 2010.

doi:10.1139/P10-051.

[46] O. O. Versolato et al. Potential of electric quadrupole transitions in radium isotopes for single-ion optical frequency standards. *Phys. Rev. A*, 83:043829, 2011. doi:10.1103/PhysRevA.83.043829.

[47] O. O. Versolato et al. Radium single-ion optical clock. *arXiv:1102.4988 [physics.atom-ph]*, 2011. doi:10.48550/arXiv.1102.4988.

[48] R. Pal et al. Calculation of parity-nonconserving amplitude and other properties of Ra^+. *Phys. Rev. A*, 79:062505, 2009. doi:10.1103/PhysRevA.79.062505.

[49] S. Blatt et al. New Limits on Coupling of Fundamental Constants to Gravity Using ^{87}Sr Optical Lattice Clocks. *Phys. Rev. Lett.*, 100:140801, 2008. doi:10.1103/PhysRevLett.100.140801.

[50] S. M. Brewer et al. $^{27}Al^+$ Quantum-Logic Clock with a Systematic Uncertainty below 10^{-18}. *Phys. Rev. Lett.*, 123:033201, 2019. doi:10.1103/PhysRevLett.123.033201.

[51] T. L. Nicholson et al. Systematic evaluation of an atomic clock at 2×10^{-18} total uncertainty. *Nat. Commun.*, 6:6896, 2015. doi:10.1038/ncomms7896.

[52] T. Rosenband et al. Frequency Ratio of Al^+ and Hg^+ Single-Ion Optical Clocks; Metrology at the 17th Decimal Place. *Science*, 319:1808–1812, 2008. doi:10.1126/science.1154622.

[53] V. A. Dzuba et al. Relativistic many-body calculation of parity-violating E1-amplitude for the 6S $\rightarrow$ 7S transition in atomic cesium. *Phys. Lett. A*, 103:265–269, 1984. doi:10.1016/0375-9601(84)90122-1.

[54] V. A. Dzuba et al. Screening of Coulomb interaction and many-body perturbation theory in atoms. *Phys. Lett. A*, 131:461–465, 1988. doi:10.1016/0375-9601(88)90302-7.

[55] V. A. Dzuba et al. Summation of the perturbation theory high order contributions to the correlation correction for the energy levels of the caesium atom. *Phys. Lett. A*, 140:493–497, 1989. doi:10.1016/0375-9601(89)90129-1.

[56] V. M. Shabaev et al. Dual Kinetic Balance Approach to Basis-Set Expansions for the Dirac Equation. *Phys. Rev. Lett.*, 93:130405, 2004. doi:10.1103/PhysRevLett.93.130405.

[57] V. V. Flambaum et al. Search for variation of the fundamental constants in atomic, molecular, and nuclear spectra. *Can. J. Phys.*, 87, 2009. doi:10.1139/p08-072.

[58] W. F. McGrew et al. Atomic clock performance enabling geodesy below the centimetre level. *Nature*, 564:87–90, 2018. doi:10.1038/s41586-018-0738-2.

[59] W. R. Johnson et al. Relativistic Random-Phase Approximation. *Phys. Scr.*, 21:409, 1980. doi:10.1088/0031-8949/21/3-4/029.

[60] W. R. Johnson et al. Finite basis sets for the Dirac equation constructed from B splines. *Phys. Rev. A*, 37:307, 1988. doi:10.1103/PhysRevA.37.307.

[61] W. R. Johnson et al. Many-body perturbation-theory calculations of energy levels along the lithium isoelectronic sequence. *Phys. Rev. A*, 37:2764, 1988. doi:10.1103/PhysRevA.37.2764.

[62] X.-M. Wu et al. Magic wavelengths for the $7s_{1/2} - 6d_{3/2,5/2}$ transitions in Ra^+. *Chin. Phys. B*, 25: 093101, 2016. doi:10.1088/1674-1056/25/9/093101.

[63] C. J. Fairhall, B. M. Roberts, and J. S. M. Ginges. QED Radiative Corrections to Electric Dipole Amplitudes in Heavy Atoms. *Phys. Rev. A*, 107:022813, 2023. doi:10.1103/PhysRevA.107.022813.

[64] M. Fan, C. A. Holliman, A. Contractor, C. Zhang, S. F. Gebretsadken, and A. M. Jayich. Measurement of the Ra^+ $7p\,^2P_{3/2}$ state lifetime. *Phys. Rev. A*, 105, 2022. doi:10.1103/PhysRevA.105.042801.

[65] V. V. Flambaum and J. S. M. Ginges. Radiative potential and calculations of QED radiative corrections to energy levels and electromagnetic amplitudes in many-electron atoms. *Phys. Rev. A*, 72: 052115, 2005. doi:10.1103/PhysRevA.72.052115.

[66] V. V. Flambaum and A. J. Mansour. Variation of the quadrupole hyperfine structure and nuclear radius due to an interaction with scalar and axion dark matter. *Phys. Rev. Lett.*, 131:113004, 2023. doi:10.1103/PhysRevLett.131.113004.

[67] G. Fricke, C. Bernhardt, K. Heilig, L. A. Schaller, L. Schellenberg, E. B. Shera, and C. W. Dejager. Nuclear Ground State Charge Radii from Electromagnetic Interactions. *At. Data Nucl. Data Tables*, 60:177–285, 1995. doi:10.1006/adnd.1995.1007.

[68] J. S. M. Ginges and J. C. Berengut. QED radiative corrections and many-body effects in atoms: vacuum polarization and binding energy shifts in alkali metals. *J. Phys. B: At. Mol. Opt. Phys.*, 49: 095001, 2016. doi:10.1088/0953-4075/49/9/095001.

[69] J.S.M. Ginges and V.V. Flambaum. Violations of fundamental symmetries in atoms and tests of unification theories of elementary particles. *Physics Reports*, 397(2):63–154, 2004. ISSN 0370-1573. doi:10.1016/j.physrep.2004.03.005.

[70] D. L. Haycock, S. E. Hamann, G. Klose, and P. S. Jessen. Atom trapping in deeply bound states of a far-off-resonance optical lattice. *Phys. Rev. A*, 55:R3991(R), 1997. doi:10.1103/PhysRevA.55.R3991.

[71] C. A. Holliman, M. Fan, A. Contractor, S. M. Brewer, and A. M. Jayich. Radium Ion Optical Clock. *Phys. Rev. Lett.*, 128:033202, 2022. doi:10.1103/PhysRevLett.128.033202.

[72] E. Iskrenova-Tchoukova and M. S. Safronova. Theoretical study of lifetimes and polarizabilities in Ba^+. *Phys. Rev. A*, 78:012508, 2008. doi:10.1103/PhysRevA.78.012508.

[73] V. V. Flambaum J. C. Berengut. Laboratory spectroscopy and the search for variation of the fine-structure constant. *Hyperfine Interact.*, 196:269–278, 2010. doi:10.1007/s10751-009-0146-y.

[74] D. Jiang, B. Arora, M. S. Safronova, and C. W. Clark. Blackbody-radiation shift in a $^{88}Sr^+$ ion optical frequency standard. *J. Phys. B: At. Mol. Opt. Phys.*, 42, 2009. doi:10.1088/0953-4075/42/15/154020.

[75] J. Jiang, J. Mitroy, Y. Cheng, and M. W. J. Bromley. Relativistic semiempirical-core-potential calculations of Sr^+ using Laguerre and Slater spinors. *Phys. Rev. A*, 94:062514, 2016. doi:10.1103/PhysRevA.94.062514.

[76] J. Jiang, Y. Ma, X. Wang, C.-Z. Dong, and Z. W. Wu. Tune-out and magic wavelengths of Ba^+ ions. *Phys. Rev. A*, 103:032803, 2021. doi:10.1103/PhysRevA.103.032803.

[77] W. R. Johnson. In D. Bates and B. Bederson, editors, *Relativistic Random-Phase Approximation*, volume 25 of *Adv. At. Mol. Phys.* Academic Press, 1989. doi:10.1016/S0065-2199(08)60094-9.

[78] W. R. Johnson. *Atomic Structure Theory.* Springer Verlag, 2007. ISBN 978-3-540-68010-9. doi:10.1007/978-3-540-68013-0.

[79] W. R. Johnson, M. Idrees, and J. Sapirstein. Second-order energies and third-order matrix elements of alkali-metal atoms. *Phys. Rev. A*, 35:3218, 1987. doi:10.1103/PhysRevA.35.3218.

[80] W. R. Johnson, Z. W. Liu, and J. Sapirstein. Transition rates for Lithium-like ion, sodium-like ions, and neutral alkali-metal atoms. *At. Data Nucl. Data Tables*, 64:279–300, 1996. doi:10.1006/adnd.1996.0024.

[81] K. P. Jungmann. Symmetries and fundamental interactions—selected topics. *Hyperfine Interact.*, 227: 5–16, 2014. doi:10.1007/s10751-014-1046-3.

[82] P. Kuske, N. Kirchner, W. Wittmann, H. J. Andrä, and D. Kaiser. Lifetime measurements by pulsed laser excitation of fast ion beams. *Phys. Lett. A*, 64:377–380, 1978. doi:10.1016/0375-9601(78)90271-2.

[83] I. Lindgren and J. Morrison. *Atomic Many-Body Theory, 2nd ed.* Springer-Verlag, 1986. ISBN 978-3-642-61640-2. doi:10.1007/978-3-642-61640-2.

[84] S.-S. Lu, F.-F. Wu, T.-Y. Shi, and L.-Y. Tang. Multipolar polarizabilities and hyperpolarizabilities for alkaline-earth-metal ions. *Phys. Rev. A*, 110:042824, 2024. doi:10.1103/PhysRevA.110.042824.

[85] A. D. Ludlow, M. M. Boyd, and J. Ye. Optical atomic clocks. *Rev. Mod. Phys.*, 87:637, 2015. doi:10.1103/RevModPhys.87.637.

[86] A. A. Madej and J. D. Sankey. Single, trapped Sr^+ atom: laser cooling and quantum jumps by means of the $4d^2D5/2 - 5s^2S_{1/2}$ transition. *Opt. Lett.*, 15:634–635, 1990. doi:10.1364/OL.15.000634.

[87] A. A. Madej, P. Dubé, Z. Zhou, J. E. Bernard, and M. Gertsvolf. $^{88}Sr^+$ 445-THz Single-Ion Reference at the 10^{-17} Level via Control and Cancellation of Systematic Uncertainties and Its Measurement against the SI Second. *Phys. Rev. Lett.*, 109:203002, 2012. doi:10.1103/PhysRevLett.109.203002.

[88] J. B. Mann and W. R. Johnson. Breit Interaction in Multielectron Atoms. *Phys. Rev. A*, 4:41, 1971. doi:10.1103/PhysRevA.4.41.

[89] S. Mannervik, J. Lidberg, L-O Norlin, P. Royen, A. Schmitt, W. Shi, and X. Tordoir. Lifetime Measurement of the Metastable $4d^2D_{3/2}$ Level in Sr^+ by Optical Pumping of a Stored Ion Beam. *Phys. Rev. Lett.*, 83:698, 1999. doi:10.1103/PhysRevLett.83.698.

[90] J. Mitroy, J. Y. Zhang, and M. W. J. Bromley. Long-range interactions of the Sr^+ ion. *Phys. Rev. A*, 77:032512, 2008. doi:10.1103/PhysRevA.77.032512.

[91] J. Mitroy, M. S. Safronova, and C. W. Clark. Theory and applications of atomic and ionic polarizabilities. *J. Phys. B: At. Mol. Opt. Phys.*, 43:202001, 2010. doi:10.1088/0953-4075/43/20/202001.

[92] A.-M. Mårtensson-Pendrill. Hyperfine structure in the $4d$ states of Rb-like Sr. *J. Phys. B: At. Mol. Opt. Phys.*, 35:917, 2002. doi:10.1088/0953-4075/35/4/315.

[93] A.-M. Mårtensson-Pendrill and A. Ynnerman. Isotope shift and nuclear charge radii of barium isotopes. *J. Phys. B: At. Mol. Opt. Phys.*, 25:L551, 1992. doi:10.1088/0953-4075/25/22/001.

[94] W. Neu, R. Neugart, E. Otten, G. Passler, K. Wendt, B. Fricke, E. Arnold, H.-J. Kluge, G. Ulm, and ISOLDE Collaboration. Quadrupole moments of radium isotopes from the $7p^2P_{3/2}$ hyperfine structure in Ra II. *Z. Phys. D*, Atoms, Molecules and Clusters 11:105–111, 1989. doi:10.1007/BF01444425.

[95] NIST. Periodic Table of the Elements, 2023. Accessed: 01/11/2023.

[96] NIST. Definitions of SI Base Units, 2023. Accessed: 04/11/2023.

[97] NIST. Fundamental Physical Constants from NIST, 2023. Accessed: 28/11/2023.

[98] NIST. NIST Atomic Spectra Database, 2023. Accessed: 06/11/2023.

[99] The University of Queensland Research Computing Centre. Bunya HPC , 2024. Accessed: 26/04/2024.

[100] R. Pal, M. S. Safronova, W. R. Johnson, A. Derevianko, and S. G. Porsev. Relativistic coupled-cluster single-double method applied to alkali-metal atoms. *Phys. Rev. A*, 75:042515, 2007. doi:10.1103/PhysRevA.75.042515.

[101] M. E. Peskin and D. V. Schroeder. *An Introduction to Quantum Field Theory*. Westview Press, 1995. ISBN 978-0-201-50397-5. doi:https://doi.org/10.1201/9780429503559.

[102] E. H. Pinnington, R. W. Berends, and M. Lumsden. Studies of laser-induced fluorescence in fast beams of Sr^+ and Ba^+ ions. *J. Phys. B: At. Mol. Opt. Phys.*, 28:2095, 1995. doi:10.1088/0953-4075/28/11/009.

[103] S. G. Porsev and A. Derevianko. Triple excitations in the relativistic coupled-cluster formalism and calculation of Na properties. *Phys. Rev. A*, 73:012501, 2006. doi:10.1103/PhysRevA.73.012501.

[104] S. G. Porsev and M. S. Safronova. Role of triple excitations in calculating different properties of Ba^+. *Phys. Rev. A*, 103:042815, 2021. doi:10.1103/PhysRevA.103.042815.

[105] B. M. Roberts. *Low-energy atomic phenomena: probing fundamental physics and searching for dark matter*. PhD thesis, University of New South Wales, 2016.

[106] B. M. Roberts. AMPSCI (Atomic Many-body Perturbation theory in the Screened Coulomb Interaction), 2023. Accessed: 24/10/2023.

[107] B. M. Roberts, C. J. Fairhall, and J. S. M. Ginges. Electric-dipole transition amplitudes for atoms and ions with one valence electron. *Phys. Rev. A*, 107:052812, 2023. doi:10.1103/PhysRevA.107.052812.

[108] M. S. Safronova and W. R. Johnson. In E. Arimondo, P. R. Berman, and C. C. Lin, editors, *All-Order Methods for Relativistic Atomic Structure Calculations*, volume 55 of *Adv. At. Mol. Opt. Phys.* Academic Press, 2008. doi:10.1016/S1049-250X(07)55004-4.

[109] M. S. Safronova, W. R. Johnson, and A. Derevianko. Relativistic many-body calculations of energy levels, hyperfine constants, electric-dipole matrix elements, and static polarizabilities for alkali-metal atoms. *Phys. Rev. A*, 60:4476, 1999. doi:10.1103/PhysRevA.60.4476.

[110] M. S. Safronova, W. R. Johnson, and U. I. Safronova. Two-photon transitions in Ca^+, Sr^+ and Ba^+ ions. *J. Phys. B: At. Mol. Opt. Phys.*, 43, 2010. doi:10.1088/0953-4075/43/7/074014.

[111] M. S. Safronova, S. G. Porsev, C. Sanner, and J. Ye. Two Clock Transitions in Neutral Yb for the Highest Sensitivity to Variations of the Fine-Structure Constant. *Phys. Rev. Lett.*, 120:173001, 2018. doi:10.1103/PhysRevLett.120.173001.

[112] U. I. Safronova. Relativistic many-body calculation of energies, lifetimes, hyperfine constants, multipole polarizabilities, and blackbody radiation shift in ^{137}Ba II. *Phys. Rev. A*, 81:052506, 2010. doi:10.1103/PhysRevA.81.052506.

[113] U. I. Safronova. All-order perturbation calculation of energies, hyperfine constants, multipole polarizabilities, and blackbody radiation shift in $^{87}Sr^+$. *Phys. Rev. A*, 82:022504, 2010. doi:10.1103/PhysRevA.82.022504.

[114] U. I. Safronova, M. S. Safronova, and W. R. Johnson. Forbidden M1 and E2 transitions in monovalent atoms and ions. *Phys. Rev. A*, 95:042507, 2017. doi:10.1103/PhysRevA.95.042507.

[115] U. I. Safronova, M. S. Safronova, and W. R. Johnson. Forbidden M1 and E2 Transitions in Monovalent Atoms and Ions. *Phys. Rev. A*, 95:042507, 2017. doi:10.1103/PhysRevA.95.042507.

[116] B. K. Sahoo, M. R. Islam, B. P. Das, R. K. Chaudhuri, and D. Mukherjee. Lifetimes of the metastable $^2D_{3/2,\,5/2}$ states in Ca^+, Sr^+, and Ba^+. *Phys. Rev. A*, 74:062504, 2006. doi:10.1103/PhysRevA.74.062504.

[117] B. K. Sahoo, B. P. Das, R. K. Chaudhuri, D. Mukherjee, R. G. E. Timmermans, and K. Jungmann. Investigations of Ra^+ properties to test possibilities for new optical-frequency standards. *Phys. Rev. A*, 76:040504, 2007. doi:10.1103/PhysRevA.76.040504.

[118] B. K. Sahoo, R. G. E. Timmermanns, and K. Jungmann. Accurate determination of the electric dipole matrix elements, lifetimes, polarizabilities and light-shifts in Ba^+ and Ra^+. *arXiv:0809.5167 [physics.atom-ph]*, 2008. doi:10.48550/arXiv.0809.5167.

[119] B. K. Sahoo, R. G. E. Timmermans, B. P. Das, and D. Mukherjee. Comparative studies of dipole polarizabilities in Sr^+, Ba^+, and Ra^+ and their applications to optical clocks. *Phys. Rev. A*, 80:

062506, 2009. doi:10.1103/PhysRevA.80.062506.

[120] B. K. Sahoo, L. W. Wansbeek, K. Jungmann, and R. G. E. Timmermanns. Light shifts and electric dipole matrix elements in Ba^+ and Ra^+. *Phys. Rev. A*, 79:052512, 2009. doi:10.1103/PhysRevA.79.052512.

[121] E. L. Snow and S. R. Lundeen. Fine-structure measurements in high-L $n = 17$ and 20 Rydberg states of barium. *Phys. Rev. A*, 76:052505, 2007. doi:10.1103/PhysRevA.76.052505.

[122] I. I. Sobelman. *Atomic Spectra and Radiative Transitions*. Springer Berlin, Heidelberg, 1992. ISBN 978-3-540-54518-7. doi:10.1007/978-3-642-76907-8.

[123] H. Sunaoshi, Y. Fukashiro, and M. Furukawa et al. A precision measurement of the hyperfine structure of $^{87}Sr^+$. *Hyperfine Interact.*, page 241–245, 1993. doi:10.1007/BF00568145.

[124] J. M. Thijssen. *Computational Physics, 2nd Ed.* Cambridge University Press, 2007. ISBN 978-1-139-17139-7. doi:10.1017/CBO9781139171397.

[125] P. Villemoes, A. Arnesen, F. Heijkenskjold, and A. Wannstrom. Isotope shifts and hyperfine structure of 134-138ba ii by fast ion beam-laser spectroscopy. *J. Phys. B: At. Mol. Opt. Phys.*, 26:4289, 1993. doi:10.1088/0953-4075/26/22/030.

[126] S. L. Woods, M. E. Hanni, S. R. Lundeen, and E. L. Snow. Dipole transition strengths in Ba^+ from Rydberg fine-structure measurements in Ba and Ba^+. *Phys. Rev. A*, 82:012506, 2010. doi:10.1103/PhysRevA.82.012506.

[127] N. Yu, W. Nagourney, and H. Dehmelt. Radiative Lifetime Measurement of the Ba^+ Metastable $D_{3/2}$ State. *Phys. Rev. Lett.*, 78:4898, 1997. doi:10.1103/PhysRevLett.78.4898.

[128] Z. Zhang, K. J. Arnold, S. R. Chanu, R. Kaewuam, M. S. Safronova, and M. D. Barrett. Branching fractions for $P_{3/2}$ in Ba^+. *Phys. Rev. A*, 101:062515, 2020. doi:10.1103/PhysRevA.101.062515.